# Impact of Fuel and Oxidizer Composition on Premixed Flame Stabilization in Turbulent Swirling Flows: Dynamics and Scaling

by

Soufien Taamallah

B.Sc., Ecole Polytechnique, Palaiseau, France (2007)
M.Sc., Ecole Polytechnique & Ecole des Mines de Paris, France (2009)

Submitted to the Department of Mechanical Engineering
in partial fulfillment of the requirements for the degree of

Doctor of Philosophy in Mechanical Engineering and Computation

at the

MASSACHUSETTS INSTITUTE OF TECHNOLOGY

February 2016



Author .....
Department of Mechanical Engineering
December 16, 2015

Certified by .....
Ahmed F. Ghoniem
Ronald C. Crane (1972) Professor of Mechanical Engineering
Thesis Supervisor

Accepted by .....
Nicolas G. Hadjiconstantinou
Co-Director, Computational Science and Engineering

Accepted by .....
Rohan Abeyaratne
Chairman, Department Committee on Graduate Studies

# Impact of Fuel and Oxidizer Composition on Premixed Flame Stabilization in Turbulent Swirling Flows: Dynamics and Scaling

by

Soufien Taamallah

Submitted to the Department of Mechanical Engineering
on December 16, 2015, in partial fulfillment of the
requirements for the degree of
Doctor of Philosophy in Mechanical Engineering and Computation

## Abstract

The world relies on fossil fuels as its main energy source (86.7% in 1973, 81.7% in 2012 [1]). Several factors including the abundance of resources and the existing infrastructure suggest that this is likely to continue in the near future (potentially 75% in 2040 [2]). Meanwhile climate change continues to be a pressing concern that calls for the development of low $CO_2$ energy systems. Among the most promising approaches are pre-combustion capture technologies, e.g., coal gasification and natural gas reforming that produce hydrogen-rich fuels. Another approach is oxy-combustion in which air is replaced by a mixture of $O_2/CO_2/H_2O$ as the oxidizer stream. However, modern gas turbines have been optimized to operate on methane-air combustion and several challenges, notably thermo-acoustic instability, arise when using other fuels or oxidizers because of their different thermochemical and transport properties. While these phenomena constitute a major challenge under conventional operations, using hydrogen-rich fuels or $CO_2$-rich oxidizer exacerbates the problem by modifying the combustor stability map in ways that are not well understood. In this thesis, we identify combustion modes most prone to dynamics, predict the onset of thermo-acoustic instability over a wide range of fuel and oxidizer compositions, and define parameters that can scale the data. To this end, a combination of experimental and numerical tools were deployed. We carried out a series of experiments in an optically accessible laboratory-scale swirl-stabilized combustor typical of those found in modern gas turbines, using high-speed chemiluminescence to examine the flame macrostructure; high-speed Particle Image Velocimetry and OH Planar Laser Induced Fluorescence to

[1] Percent of total primary energy. Source: IEA Key World Energy Statistics 2014.
[2] Percent of total primary energy. Source: IEA energy outlook 2014

probe the flow and flame microstructure. Numerical simulations were used to complement experiments and examine the complex three-dimensional two-way interaction between the flame and the turbulent swirling flow. Experimental data were used to construct the stability maps for different $CH_4$-$H_2$ mixtures and analyze the dynamic flame macrostructures and their transitions. A comparison with acoustically uncoupled combustion shows that the onset of thermo-acoustic instability is concomitant with a specific transition associated with the intermittent appearance of the flame in the outer recirculation zone (ORZ) and stabilization along the outer shear layer (forming between the swirling jet and the ORZ, as revealed by the PIV-PLIF data). The sudden onset of large amplitude limit cycle oscillations and the observed hysteresis suggest the existence of a sub-critical Hopf bifurcation typically characterized by a bistable or "triggering" zone; the flame intermittency in the ORZ can potentially provide the disturbance required to trigger these oscillations. Using a dual-camera method to track chemiluminescence in space and time, this flame transition was found to originate from a reacting kernel that detaches from the inner shear layer flame (forming between the jet and the vortex breakdown zone), reaching the ORZ and spinning at a specific frequency; its characteristic Strouhal number is independent of the Reynolds number and the fuel/oxidizer, only a function of the swirl strength. We propose a new Karlovitz number based criterion that defines the transition on a flow time - flame time space, the former being the inverse of the spinning frequency and the latter being the flame extinction strain rate. According to this scaling, the flame survives in the ORZ if and when it can overcome the region's bulk strain rate. This criterion is valid over a wide range of operating, fuel and oxidizer composition, covering a wide range of fast to slow chemistry scenarios. Given the role of this flame transition in triggering the instability, the same criterion is applicable to predicting the onset of thermo-acoustics. The interaction of the turbulent swirling flow with the flame is further examined using large eddy simulations. Numerical simulations show that the experimentally observed large scale flame structures along the inner shear layer are due to a helical vortex core that originates at the swirler's centerbody. This vortical structure stays aligned with the centerline in the combustor upstream section, but bends and reaches the inner shear layer-stabilized flame around the sudden expansion where it causes the flame wrinkling. We propose that the flame kernel igniting the ORZ/ OSL observed in the experiment may be related to the interaction between the helical vortical structure and the outer shear layer.

**Doctoral Thesis Committee:**

Ahmed F. Ghoniem
Committee Chair and Thesis Supervisor
Ronald C. Crane (1972) Professor of Mechanical Engineering at MIT

Douglas P. Hart
Skolkovo Foundation Professor of Mechanical Engineering at MIT

Youssef M. Marzouk
Class of 1942 Associate Professor of Aeronautics and Astronautics at MIT

Mohamed A.M. Habib
Professor of Mechanical Engineering at KFUPM

Santosh J. Shanbhogue
Research Scientist, Department of Mechanical Engineering at MIT

# Acknowledgments

First of all, I would like to thank my wife, Lindsey, for her unerring support and Franciscan patience during all these years of hard work. Her mental support, presence and love provided a constant safety net all along.

Professor Ghoniem wins, easily, the trophy of the exceptional supervisor and advisor. I am not only very grateful for his guidance along this hard process but also for his infallible trust in me; Professor Ghoniem gave me the freedom and flexibility necessary for creative thinking and work. He trusted my intuition and always encourage it. I benefited tremendously from his wisdom, experience and scientific depth. Professor Ghoniem and his wife Elizabeth have been both mentors and friends. By enjoying life through traveling, hiking and discovering while being so professional and successful, they are an abundant source of inspiration.

I am very grateful to all my committee members, Prof. Hart, Prof. Marzouk, Prof. Habib and Dr. Santosh Shanbhogue, who followed my evolution and my results during the PhD process. They all gave such great suggestions and insights, and encouraged me to take a step back and see the big picture from time to time. I am very pleased to have had Santosh not only as a committee member but as a lab-mate. I learned so much from his technical expertise in experimental combustion. I thank him for teaching me how to use the PIV and PLIF lasers which was a critical component in my scientific contribution to the field. Also, special thanks to Dr. Christos Altantzis as well who is another mentor I had all along my PhD (although indirectly). I thank him for the endless hours of great brainstorming covering all sorts of topics either while walking from MIT to Harvard Square or during his smoking breaks overlooking the Charles River and Boston. I enjoyed sharing his passion about combustion, fluids, CFD, history, philosophy... I wish him the best in his next endeavors.

I would like to thank all the previous and current members of the RGD lab. Special thanks go to the combustion dynamics group I had the pleasure to interact with and learn from: Santosh S., Konstantina V., Kushal K., John H., Zach L., Gaurav K., Dominik B. and more recently Nadim C., ByungChul C. and Dan M. Special thanks to Konstantina who shared a true commitment to improving communication and exchange (of ideas and tools) within the group. I wish her the best in her academic career.

Other RGD lab sub-group members have been such a great support; my heartfelt thanks for making our lab such a great and friendly research environment. I am thinking of, in particular, the membrane lab. sub-group (Pat, Anton, Georges and Xiaoyu) who are always there to help when we are missing something in the lab (thermocouples, gas cylinders, even torches! they always had everything.). The "BP guys" / RGD soccer team : Christos A, Richard B, Akhilesh B, Addison S., Nadim C, and Nwike C, are the best; thanks to our bi-weekly soccer plan, I maintained not only physical but most importantly mental health.

None of this would have been possible without my family. They did and still do everything to make my life easier through their endless love and support. My parents, Marie-Claude and Mohamed, my brother Skander, my sister Rym, her husband Salem and the amazing "kiddos" Sarra and Mehdi are always there for me. My new family — the family in law — has also been a tremendous part in any of my success; Thank you Mike, Natasha and Brittany for all your positive energy and cheering me up during difficult times. My wife Lindsey and my two cat-sons Sidi and Shoush definitely deserve half of my PhD (at least). Without their care and appeasing purring I would not have achieved my goals. I am immensely grateful for their existence.

# Contents

# List of Figures

# List of Tables

# Nomenclature

***Abbreviations***

| | |
|---|---|
| **ORZ** | Outer recirculation zone |
| **IRZ** | Inside or inner recirculation zone |
| **OSL** | Outer or Outside Shear Layer |
| **ISL** | Inner or Inside Shear Layer |
| **VB** | Vortex Breakdown |
| **VBB** | Vortex Breakdown Bubble |
| **PVC** | Precessing Vortex Core |
| **KH** | Kelvin-Helmholtz |
| **IR** | Infrared |
| **PLIF** | Planar Laser Induced Fluorescence |
| **HS-SPIV** | High-Speed Stereoscopic Particle Image Velocimetry |
| **PMT** | Photomultiplier Tube |
| **RMS** | Root Mean Square |
| **TC** | Thermocouple |
| **LES** | Large Eddy Simulation |
| **DNS** | Direct Numerical Simulation |
| **SGS** | Sub-grid Scale |
| **ER** | Equivalence ratio |

| | |
|---|---|
| **SPL** | Sound Pressure Level |

***Non-dimensional numbers***

| | |
|---|---|
| $K_a$ | Karlovitz number |
| $L_e$ | Lewis number |
| $S$ | Swirl number |
| $Re_{D_{in}}$ | Reynolds number based on inlet diameter $d_{in}$ |
| $Re_t$ | Turbulent Reynolds number |
| $St$ | Strouhal number |
| $St_{sw}$ | Swirl Strouhal number |
| $Sc$ | Schmidt number |

***Roman***

| | |
|---|---|
| $D_{in}$ | Inlet diameter $(m)$ |
| $D_{out}$ | Outlet diameter $(m)$ |
| $D_{cb}$ | Centerbody diameter $(m)$ |
| $R_{reat}$ | Reattachment length $(m)$ |
| $S_L^0$ | Unstretched laminar burning velocity $(m.s^{-1})$ |
| $S_T$ | Turbulent burning velocity $(m.s^{-1})$ |
| $t$ | Time (s) |
| $T_{ad}$ | Adiabatic flame temperature (K) |
| $T_u$ | Temperature of the unburnt reactants (K) |
| $U_b$ | Bulk velocity of the incoming reactants $(m.s^{-1})$ |
| $U_x$ | Velocity in the axial direction $(m.s^{-1})$ |
| $U_r$ | Velocity in the radial direction $(m.s^{-1})$ |

| | |
|---|---|
| $U_\theta$ | Velocity in the azimuthal direction ($m.s^{-1}$) |
| $U_m$ | Meridional velocity: combined axial-radial velocity ($m.s^{-1}$) |
| $\mathbf{g}$ | Velocity gradient ($s^{-1}$) |
| $f_{ORZ}$ | ORZ flame spinning frequency ($s^{-1}$) |
| $D$ | Mass diffusivity ($m^2.s^{-1}$) |
| $D_{eff}$ | Effective mass diffusivity ($m^2.s^{-1}$) |
| $Y_k$ | Mass fraction of species k |
| $F$ | Thickening factor |
| $F_{loc}$ | Local thickening factor |
| $E$ | Efficiency function |

***Greek***

| | |
|---|---|
| $\delta_T$ | Thermal thickness of the flame ($m$) |
| $\alpha_{th}$ | Thermal diffusivity of the unburnt reactants ($m^2.s^{-1}$) |
| $\alpha_{sw}$ | Swirl angle in arc degrees |
| $\phi$ | Equivalence ratio |
| $\kappa_{ext}$ | Extinction strain rate ($s^{-1}$) |
| $\Xi$ | Non-dimensional wrinkling factor |

# Chapter 1

# Introduction

## 1.1 Gas Turbine Combustion and the Dual Challenge of Fuel Flexibility

### 1.1.1 Gas Turbines and Lean Premixed Combustion

Gas turbines (GT) in combined cycle configuration (GTCC) offer one of the most efficient technologies for large-scale stationary power generation [15, 79, 6]. First law efficiencies up to 60% (on a low heating value basis) have been reached thanks to progress in materials and cooling technologies that allows the gas turbine to operate with turbine inlet temperatures in the range of 1500-1600°$C$ [32]. Nevertheless, the ever increasing stringent regulations on harmful gases emissions, notably nitrogen oxides ($NO_x$) and carbon monoxide, as well as the possible caps on $CO_2$ emissions, are expected to keep changing the way gas turbines — particularly combustion systems — are designed and operated.

Lean premixed combustion of natural gas — the most common fuel used in gas turbines and composed predominately of methane — has been developed and successfully

applied during the last few decades to achieve low $NO_x$ emissions with minimal cycle efficiency penalties. Alternative methods of lowering $NO_x$ include fuel staging, inert species dilution as well exhaust gas clean-up in a non-premixed combustion system. In addition to being limited in their $NO_x$ abatement potential, these methods are associated with increased operating and/or capital costs as well as efficiency penalties [24], contrary to premixed combustion. However, operating a combustor in a lean premixed mode brings also its own challenges [94]; it raises operability concerns because of the increased risk of combustion instabilities, as well as possible higher CO emissions, leading to a potentially narrow window of safe, stable and clean operation in terms of both CO and $NO_x$.

### 1.1.2 Importance of GTs in Transitioning to Cleaner Power

Promising methods for reducing emissions, combined with the high efficiency, the fast ramp rate and the relatively low cost makes gas turbines - especially in a combined cycle configuration - one of the best candidates to enable a transition toward a low carbon-based power mix. For instance, the current high capital cost and the intermittency associated with renewable energy technologies could be alleviated by an integration with an efficient, cost effective and low emitting fossil-fuel based power generation method, something that gas turbine combined cycles can achieve. An example of such systems is the integrated solar reforming combined cycles [85]. Furthermore, relatively more abundant fossil (coal) or renewable solid fuel (biomass) can also be used in an integrated gasification combined cycle (IGCC) configuration with partial or complete $CO_2$ capture following the gasification and the water-gas shift processes.

### 1.1.3 The Double Challenge of Fuel Flexibility

In such pre-combustion capture configurations, but also in many other cases where hydrogen is available as a by-product of industrial or chemical processes, the gas turbine combustion system would need to be operated using a different fuel than methane that is synthetic gas (mixture of $H_2$, CO, $CH_4$ and $CO_2$). Two difficulties emerge here: (1) gas turbines have been historically designed and optimized for the use of natural gas so there is a need for these to be adapted to these fuels. (2) An additional complication is the likely variations in the fuel composition which leads to operability issues [78, 104]. We detailed the effects of fuel composition change on the micro- and macro-scale levels in our literature review [103]. To illustrate the latter point, if gas turbine combustion is combined with gasification, the solid fuel input can vary and be any of the different grades of coal and biomass leading to a change in the output fuel composition. Also if syngas is produced through solar reforming then the fuel composition may vary with the changes in the available solar heat throughout the day. Table-1.1 shows typical composition of syngas from gasification of coal and biomass along with an example of daily average fuel composition from solar reforming of methane.

Among different gaseous fuels, hydrogen leads to major operability concerns in premixed combustion mainly because of its radically different chemical and transport properties compared to standard fuels which, in turn, affect the fundamental flame properties (like the stretched and unstretched laminar burning velocities and the extinction strain rate) and thus the combustion process. Thermo-chemical and transport properties of fuels are critical in determining the characteristics of the combustion process and flame properties. Table-1.2 and Table-1.3 show the values of these parameters for $CH_4$, CO and $H_2$ as well as for air, the conventional oxidizer, at 300K and 1 bar. We see how hydrogen stands out compared to other fuels, standard fuels like methane in particular. Heat and momentum diffusivity for hydrogen are around one order of

| Process → | *Gasification* *$O_2$ blown* | | *Gasification* *Air blown* | | *Gasification* Steam | *Reforming*** Steam |
|---|---|---|---|---|---|---|
| Source → | Lignite | Bitumi--nous coal | Lignite | Bitumi--nous coal | biomass* | Methane Solar |
| Syngas (vol.% dry) | | | | | | |
| $H_2$ | 36.4 | 37.3 | 12.6 | 21.6 | 51.3 | 55.2 |
| CO | 43 | 52 | 22.5 | 21.6 | 42.7 | 5.4 |
| $CH_4$ | 1.7 | 3.5 | 0.8 | 1.8 | 1.5 | 30.0 |
| $CO_2$ | 13.1 | 5.3 | 7.7 | 8.9 | - | 9.4 |
| $N_2$ | 1 | 0.3 | 55.7 | 50.6 | 0.2 | - |
| $H_2S$ | ∼0.4 | ∼0 | - | - | - | - |

Table 1.1: Typical composition of syngas from different sources and processes. *Syngas from biomass is the average gas composition from bagasse, pine sawdust, poplar sawdust and almond shells gasification. ** Syngas from solar steam reforming is the daily composition average (Data reproduced from [10] , [2] and [86]).

magnitude larger than for $CH_4$, CO and also air. In addition, hydrogen molecules diffuse in air around four times as fast as $CH_4$ and CO in air. $CH_4$ and CO have similar transport properties, except a large difference in density. This difference in density however gets undermined when working with premixed fuels as the fuel mole fraction is small usually compared to the oxidizer i.e. for dilute fuels at lean conditions. Clearly, $CH_4$-CO-$H_2$ blends should be expected to have different combustion properties than the pure standard $CH_4$.

| Fuel | Density $kg.m^{-3}$ | molecular weight $g.mol^{-1}$ | HHV per mole $MJ.mol^{-1}$ | HHV per unit mass $MJ.kg^{-1}$ | HHV per unit vol. $MJ.m^{-3}$ |
|---|---|---|---|---|---|
| $CH_4$ | 0.65 | 16.04 | 890.38 | 55.50 | 36.17 |
| CO | 1.14 | 28.01 | 282.99 | 10.10 | 11.49 |
| $H_2$ | 0.08 | 2.02 | 285.76 | 141.75 | 11.60 |

Table 1.2: Properties of fuels of interest at 300 K and 1 atm. HHV stands for high heating value. Data compiled using GRI 3.0 transport and thermal properties [90]

In addition to blowout and flashback, known as static instabilities, a combustion

| Fuel | Density | Thermal Diffusivity | Mass diffusivity (in Air) | Momentum diffusivity | Pr | Le |
|---|---|---|---|---|---|---|
| | $kg.m^{-3}$ | $10^{-6}$ $m.s^{-2}$ | $10^{-6}$ $m.s^{-2}$ | $10^{-6}$ $m.s^{-2}$ | | ($T_{ad}$ = 1660 K) |
| $CH_4$ | 0.651 | 24.56 | 22.39 | 17.53 | 0.714 | 0.999 |
| CO | 1.138 | 21.50 | 20.67 | 15.61 | 0.726 | 1.070 |
| $H_2$ | 0.082 | 159.4 | 77.92 | 109.9 | 0.689 | 0.437 |
| Air | 1.172 | 22.28 | - | 15.89 | 0.713 | - |

Table 1.3: Fuel Properties at 300 K and 1 bar. Lewis number for lean fuel-air mixtures that provide the same adiabatic flame temperature $T_{ad}$=1660 K ($\phi$=0.6, 0.51, 0.45 for Methane, $H_2$ and CO respectively). Data compiled using GRI 3.0 transport and thermal properties [90]

system may face other stability issues, mainly when operating in a premixed mode for low $NO_x$ emissions; these are known as dynamic or thermo-acoustic instabilities. This is already challenging for standard fuels like methane; and this challenge is exacerbated when other fuels, especially the ones with substantially different thermo-chemical and transport properties like $H_2$ are used.

## 1.2 Combustion Instabilities and Impact of Fuel Composition

Heat release rate from the reacting flow can be subject to fluctuations typically due to either equivalence ratio oscillations or to unsteadiness of the flow field itself, for instance vortex shedding from a flow separation region and vortex roll-up along a shear layer. Heat release oscillations can couple with the acoustic pressure fluctuations to form a positive feedback loop leading to a large increase in pressure amplitude and the establishment of self-sustained limit cycle oscillations. Thus, while lean premixed combustion has been introduced as an efficient and cost effective way to curb $NO_x$ emis-

sions, it can suffer from combustion dynamics as premixed systems are more susceptible to this type of instabilities [55]. This dilemma has been coined as the "innovation trap" [18, 95] and led to a large research effort that is still ongoing today.

Theoretical and experimental investigation of thermo-acoustic instabilities date back to the findings of Rayleigh [76] and the experimental work of Mallard and Le Chatelier [61]. Rayleigh established a criterion still used and quoted today by the combustion community. This criterion involves the Rayleigh index which is equal :

$$Ra_{index} = \int\int\int_{V} p^{'}(\underline{x},t)\ \dot{q}^{'}(\underline{x},t)dV \tag{1.1}$$

Where $p^{'}(\underline{x},t)$ and $q^{'}(\underline{x},t)$ are the fluctuations of pressure and heat release rate per unit volume, respectively, relatively to mean values. V is the volume of the combustion chamber domain, $\underline{x}$ is the spatial coordinate and t the time.

A modern interpretation of this criterion states that heat release oscillations act as an acoustic energy source if it is in phase with the pressure fluctuations. In other words, if the Rayleigh index ($Ra_{index}$) is positive then the total acoustic energy grows. It is known today that this criterion is only a necessary condition for instabilities to occur in the sense that if the heat release fluctuations and the pressure are in phase, the pressure fluctuations will grow. It is not sufficient since it does not account for acoustic energy losses. $p^{'}(x,t)$ and $q^{'}(x,t)$ can be in phase without observing thermo-acoustic instabilities when acoustic losses are large enough to damp the instability. Thus, the same criteria has been since extended later to take acoustic losses into account [68]: the linearized conservation of total acoustic energy shows that the acoustic energy growth rate depends on the Rayleigh index but also on the acoustic fluxes through the domain boundaries and the extended criterion for instabilities becomes:

$$\int\int\int_V \frac{\gamma-1}{\gamma\,\bar{p}} p^{'}(\underline{x},t)\;\dot{q}^{'}(\underline{x},t)dV > \int\int_S p^{'}(\underline{x},t)\;\underline{u}^{'}(\underline{x},t).\underline{n}dS \tag{1.2}$$

$p^{'}(\underline{x},t)$ and $\dot{q}^{'}(\underline{x},t)$ were defined above. $u^{'}(\underline{x},t)$ is the acoustic velocity fluctuation, dS a surface element of the domain boundary with normal $\underline{n}$.

Dynamic instabilities can have a dramatic impact on the hardware since extremely large sound pressure levels (SPL) can be reached. Indeed, as it can seen from Fig.1-1 - one of the few investigation of dynamic instabilities using syngas at various compositions done in our lab. - the overall sound level can increase by 25 dB, i.e. around 15 times increase in acoustic pressure fluctuations. Because of its critical importance, dynamic instabilities arising in premixed combustion have been intensively studied for decades and are still an active area of research. Despite these efforts our knowledge in this field is still incomplete, even for the most standard fuels like methane. This is also the reason why most of the research done in this field is still directed towards methane and relatively little research focused on hydrogen-rich fuels.

Over the past decades, multiple mechanisms that can lead to the coupling between the acoustic pressure and heat release fluctuations have been identified and documented. These have been reviewed by Ducruix and co-workers [83]. Candel [9] provides also a comprehensive review of the challenges pertaining to combustion instabilities and the advances made in understanding and controlling it. A more recent review was proposed by Huang et al. [37] that focuses on dynamic instabilities in swirl-stabilized combustors relying on both experimental and numerical work. They also surveyed different driving mechanisms for instabilities as well as the existing methods for mitigating this unwanted phenomena both in a passive and active fashion. Among common driving mechanisms are flame surface fluctuations or burning rate fluctua-

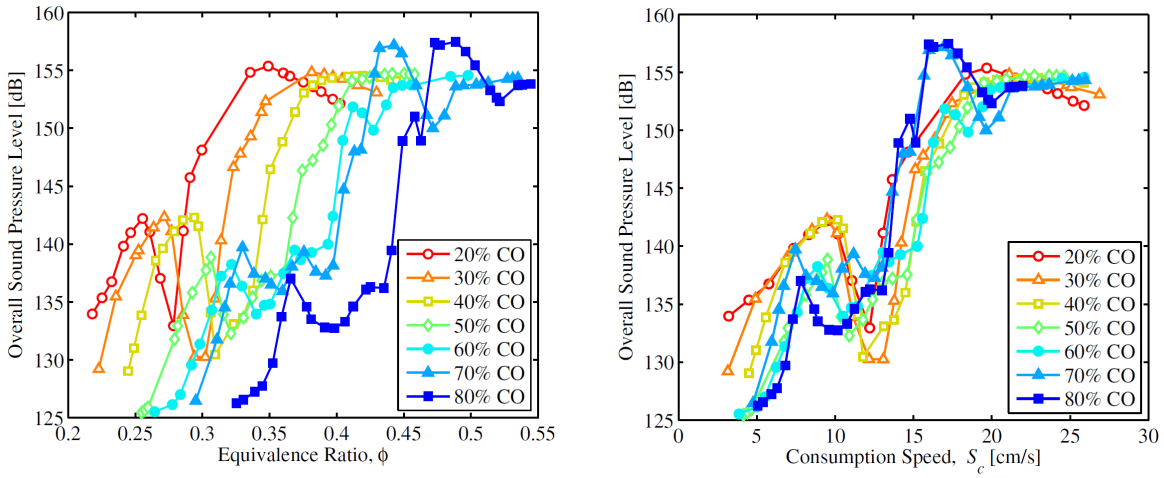


Figure 1-1: Overall sound pressure level and observed modes for two different Syngas compositions at inlet temperature of 300K (a) as a function of equivalence ratio (b) as a function of strained consumption speed as a scaling parameter (modified from [92])

tions due to vortex-flame interaction as well as wall-flame interactions. Equivalence ratio fluctuations are also among the important driving mechanisms for thermo-acoustic instabilities. In this thesis, as we will see later, the experimental setup allows only a negligible fluctuation in equivalence ratio, through the use of a choke plate at the inlet; this eliminates Equivalence ratio fluctuations mechanism as a possible mechanism for thermo-acoustic instabilities in our case.

A simplified way to identify possible mechanisms [57] leading to dynamic instabilities is to write the heat release rate as :

$$\dot{Q}(t) = \int_{Flame\ Surface} \int \rho_r \; S_{c,r} \; \Delta h_r \; dA \tag{1.3}$$

where $\rho_r$ is the reactant density, $S_{c,r}$ is the reactants consumption speed, $\Delta h_r$ is the heat release per unit mass of reactant and finally dA is a flame surface element. From the heat release expression (Eq.1.3) one can see the variety of mechanisms that can

lead to heat release fluctuations: changes in consumption speed, in flame surface area or heat of reaction could lead to unsteady heat release. Changes in fuel composition can affect any of these variables.

Fuel composition effect, in particular hydrogen, on dynamic instabilities has been investigated by several researchers [39, 16, 109, 33, 17, 92, 54] and briefly reviewed as well [78, 104]. It is agreed that changes in the fuel do have an influence on the dynamic characteristics of the combustion system. A simple time scale approach (change in chemical reaction time scale as well as the convection time scale) carried by Kushari et al. [49] and later by Janus et al. [39] showed that it is expected to see different dynamic response when fuel composition is modified. Fuel composition changes can affect combustion instabilities primarily by changing the flame shape and local dynamics, or the flame location thus the phase between heat release and pressure fluctuations for a same flame shape. This has the important implication that the effect of changing fuel composition can not only be destabilizing but in some cases stabilizing. By relying on a similar time scale approach as the one followed by Kushari et al. [49], Lieuwen et al. [104] highlighted that fuel composition variations can change the convection time from the origin of a fluctuation to the center of mass of the flame. Indeed, changing the mixture composition affects the burning velocity through a different diffusivity and chemical reactivity and also by changing the response of the flame to stretch, which affects the convective time scale.

Figura et al. [17] reached a similar conclusion; in their study they focused on flame-vortex driven combustion dynamics in a swirl-stabilized combustor operating with mixtures of natural gas and $H_2$. When fuel is changed by increasing $H_2$ content, the dynamically stable range was reduced and instability occurred starting at a lower equivalence ratio making it difficult to operate at the same equivalence ratio. The authors [17] show that, for the same combustor geometry thus fixing the natural modes

of the combustor, high pressure fluctuations appear around $\phi$=0.7 as equivalence ratio is increased, when operating with natural gas. Adding 25% $H_2$ to the mixture, keeping all the other operating variables the same, made the transition to instability occur earlier at $\phi$=0.6, as equivalence ratio is raised. Another major difference is that despite still transitioning to limit cycle oscillations, the sound pressure level recorded for the hydrogen mixture was halved, i.e. becoming less destructive. This was attributed to the lower heat release rate per unit volume which lead to a weaker acoustic energy source, as shown in Eq.1.3. In addition, a small change in the instability dominant frequency is noted; this is due to the lower temperature (due to the lower equivalence ratio) hence a slight decrease in the natural frequency of the combustion chamber. The authors [17] conclude that the dynamic stability of the combustor they analyzed, when fuel composition and operating conditions change, was to a large extend determined by the location of the flame center of heat release (average flame location) under stable conditions.

More recently, in our lab., Speth et al. [92] investigated dynamic instabilities for different syngas mixtures in a similar swirl-stabilized combustor as the one used throughout this thesis. This is one of the few studies focusing on syngas composition effect on dynamic instabilities. Different instability modes in a swirl-stabilized combustor were observed. With a fixed geometry, a swirl number of S=0.7 and Reynolds number held constant at Re=25,000, $H_2$-CO mixtures with volumetric fractions ranging from 20%-80% to 80%-20% at atmospheric pressure and temperature, were investigated at equivalence ratios ranging from near the lean blowout limit to near the flashback limit. As the equivalence ratio is raised, different mixtures of CO and $H_2$ have the same overall dynamic behavior i.e. will go through the same sequence of instability modes. So changing the fuel composition does not introduce new unstable or stable modes. However, there is one noteworthy difference: the sound pressure level (SPL) are shifted

to lower equivalence ratio, consistently with the widening of the static stability map (lower lean blowout limit) when $H_2$ content is raised. Thus, the stability map curves appear self-similar and this led the authors to search for a similarity variable that may collapse all sound pressure level curves and capture the transitions between the difference stability modes. While the adiabatic flame temperature and the laminar flame speed failed in collapsing the curves, a strained consumption speed succeeded. The strain rate value was found as the optimal value leading to the best collapse as an objective function; the strain rate value does not come in this case from experimental data due to the complexity of such a task in highly three dimensional swirling flows. While providing a useful criterion and a novel framework to scale stability maps across fuels, less attention was directed toward understanding the changes in the flow field and the interaction of the turbulent flow with the flame before instabilities occur and at the onset of thermo-acoustic coupling. This thesis comes as a continuation of the previous work to address these important points.

As mentioned briefly earlier, Figura et al. [17] showed that fuel composition, along with other operating conditions, like equivalence ratio and inlet temperatures influence the center of heat release. Flames with the same flame heat release center are likely to have the same dynamic response. This link between flame shapes and thermo-acoustic modes leading to an important and still on-going research effort to understand different flame anchoring modes, called mean flame shapes or macrostructures.

## 1.3 Swirling Flame Macrostructures

Several researchers reported the existence of different flame macrostructures in swirl-stabilized combustion. These have been previously documented as functions of several parameters such as the fuel composition [82, 47, 29], equivalence ratio and preheat

temperature [20, 13], and Reynolds number [97], swirl number and confinement [30] as well as centerbody geometry [12]. Multiple swirling flame configurations have also been reported for oxy-flames under stoichiometric conditions but with $CO_2$ mole fraction used as a parameter (replacing $N_2$ as a diluent) [87, 88].

Most of these studies reported the following flame macrostructures although possibly named differently [1]: a columnar tubular flame (I); an bubble-columnar flame (II); a single conical flame stabilized along the inner shear layer ISL (flame III); and a double conical flame with an additional flame front stabilized in the ORZ and along the outer shear layer OSL (flame IV). These flames can be lifted or attached to the centerbody and/or sudden expansion side wall. Examples of flame macrostructures are shown in Fig. 1-2 as a function of the equivalence ratio for a premixed $CH_4$ combustion in air. In **chapter**-3, we will see that a similar set of flame macrostructures is observed in our lab-scale swirl-stabilized combustor, used in this thesis. In **chapter**-4.1, we will focus on the mechanism and conditions leading to a transition from flame III to IV, for reasons that will become clear at the end of **chapter**-3.

It is essential to understand the controlling parameter for different flame macrostructures. The conditions under which transitions between flame types macrostructures and the mechanisms underlying it are of great interest. One of the main reasons is the potential shift in dynamic stability characteristics of certain combustors when changes in flame macrostructure occur. Few researchers highlighted this relationship. By changing the inlet temperature in their LES investigation of swirl-stabilized combustion, Huang et al. noted that there is a temperature threshold where the flame propagated into the ORZ. This change in flame macrostructure was accompanied by a numerical bifurcation to thermo-acoustic instability. The author argued that the presence of the flame in the ORZ, makes the combustor more prone to instability since a large amount of heat is

[1] Some authors use the V and M flames nomenclature, see [30, 29, 47]

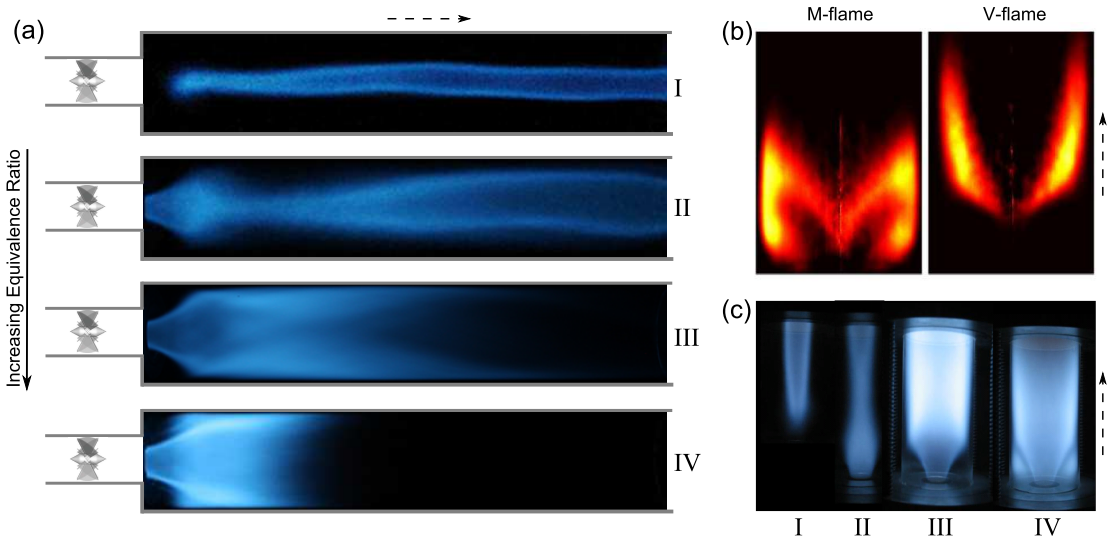


Figure 1-2: Dashed arrows show the direction of the flow. (a) Line-of-sight chemiluminescence showing flame macrostructures I to IV observed for $CH_4$/air combustion as a function of equivalence ratio, with a Reynolds number of 20,000 and axial swirler blade angle of 45 degree at atmospheric pressure. The geometry is the one used in this thesis (described in section-2.1.1). From top to bottom, increasing equivalence ratio ($\phi$=0.51, $\phi$=0.55, $\phi$=0.60, $\phi$=0.65). (b) M (left) and V (right) Abel-deconvoluted chemiluminescence images of $CH_4$/air flames, at $\phi$ = 0.62 - $U_b$ = 12.2 m/s and $\phi$ = 0.57 - $U_b$ = 12.1 m/s , respectively (Reproduced from [65]. (c) Line-of-sight chemiluminescence showing flame macrostructures I to IV observed for $CH_4$/air combustion at different equivalence ratio (Reproduced from [19]).

.

released within a confined area close to an acoustic anti-node [37]. Such a results favors a hypothesis of causality from a transition to ORZ flame to an onset of thermo-acoustic instabilities. In a study spanning a wider range of operating conditions, Fritsche et al. investigated both optical and acoustic characteristics of flames at different conditions: one of the goal was to explore the connections existing between flame types and noise levels. They showed that flame shapes closer to the lean blowout i.e. the columnar flames and single conical flames are always dynamically stable, and that the flames with reactions taking place in the ORZ can be stable or unstable depending on the choice of equivalence ratio and inlet temperature. The transition to thermo-acoustic instability as the equivalence ratio is increased, for a fixed inlet temperature, occurred along with the first appearance of a continuous flame front in the ORZ.

## 1.4 Thesis Goal, Approach and Outline

From the above literature results, we see that the relationship between flame macrostructures and thermo-acoustic stability has been observed but few systematic investigations of this relationship, spanning all possible macrostructures, were undertaken. In addition, it is still unclear from previous studies whether acoustic fluctuations are responsible for the flame macrostructures to change (in particular the propagation into the ORZ in flame IV) or if the change in flame shape leads to an increase in sound levels. In other words, more evidence is needed to know if flame macrostructure transitions are an acoustically dominated or a turbulent combustion dominated phenomenon. Moreover, more effort is required to understand the physics underlying the transition between different flame shapes and eventually its scaling over a wide range of operating conditions and fuels to make an additional step towards lean premixed fuel-flexible operations.

The main goal of this thesis is to to explore the relationship between different flame

macrostructures in a swirl-stabilized combustor at different equivalence ratios and its stability map, with the ultimate objective of predicting the onset of such instabilities using a wide range of fuel mixtures. To reach this goal, we will rely on advanced laser-based optical diagnostics complemented with Large Eddy Simulations. Experimental tools (pressure and temperature point measurements, integrated heat release rate measurements, line-of-sight flame chemiluminescence) and laser-based optical diagnostics (HS-PIV, OH-PLIF) are used to build stability maps and characterize different flame macrostructures, as well as to probe the flame and flow structures in a two-dimensional plane. Experimental data will be also used for LES code validation which will be performed to show the acceptable fidelity of such simulations. Once the LES code is validated, the simulated three dimensional reacting flow field will be used to examine the complex flow and flame interactions in such a flow configuration.

This thesis is organized as follows: in **chapter**-2, we will describe the lab-scale swirl-stabilized combustor used throughout this thesis as well as the different experimental and numerical tools. We will also present the Large Eddy Simulation setup and its validation study. In **chapter**-3, we will build the stability maps of the combustion system for different $CH_4$-$H_2$ mixtures and investigate the link between thermo-acoustic instabilities and flame macrostructures under acoustically coupled and decoupled conditions. This will demonstrate the importance of the flame transition from an inner shear layer (ISL) only flame (flame III) to a flame stabilized along both the ISL and OSL/ORZ (flame IV). The physical mechanism underlying the transition from flame III to flame IV will be examined in **chapter**-4. In **chapter**-4, we will also analyze the ORZ flame transition over a wide range of inflow conditions (inlet Reynolds and swirl numbers) and fuel compositions ($CH_4$ with $H_2$ up to 50% by volume). This will allow us to build a model for scaling this flame transition across these operating conditions. In **chapter**-5, we will extend our investigation of flame III to IV transition

to oxy-combustion and test the hypothesis that the model proposed in **chapter**-4 can be extended to this type of combustion. We will see that the same model based on a balance between the fuel's extinction strain rate and the prevailing bulk strain rate in the ORZ can be extended to oxy-combustion if the extinction strain rate computations are performed at realistic ORZ temperature. Finally, in **chapter**-6, we will examine the flame and flow structures observed in the experiment. LES simulations are performed to overcome the limitation of the experimental tools to two dimensional data. LES will be used to trace the origin and dynamics of the ISL-stabilized flame's large scale wrinkling highlighted by OH-PLIF data.

# Chapter 2

# Experimental Apparatus and Numerical Tools

## 2.1 Experimental Setup and Diagnostics Tools

### 2.1.1 Laboratory-Scale Swirl Combustor

Experiments are conducted in a swirl-stabilized dump combustor representative of can combustors found in modern gas turbines. Fig.2-1 shows the details of the experimental setup used in this study. The experimental setup is similar to the ones previously investigated by our research group [92, 51, 88]. The main additions to the setup compared to previous versions are the change of the combustor length to control the acoustic field, the added levels of insulation and thermocouples that will be used in the heat loss analysis as well as LES code validation. Fuel and air are premixed upstream of a choke plate. The role of the choke plate used here is two-fold. First, by choking the flow, a sonic Mach number is imposed preventing pressure waves from traveling upstream; thus, the fuel and air nozzles would not be disturbed by acoustic wave avoiding equivalence ratio fluctuations. This means that equivalence ratio fluctuations will

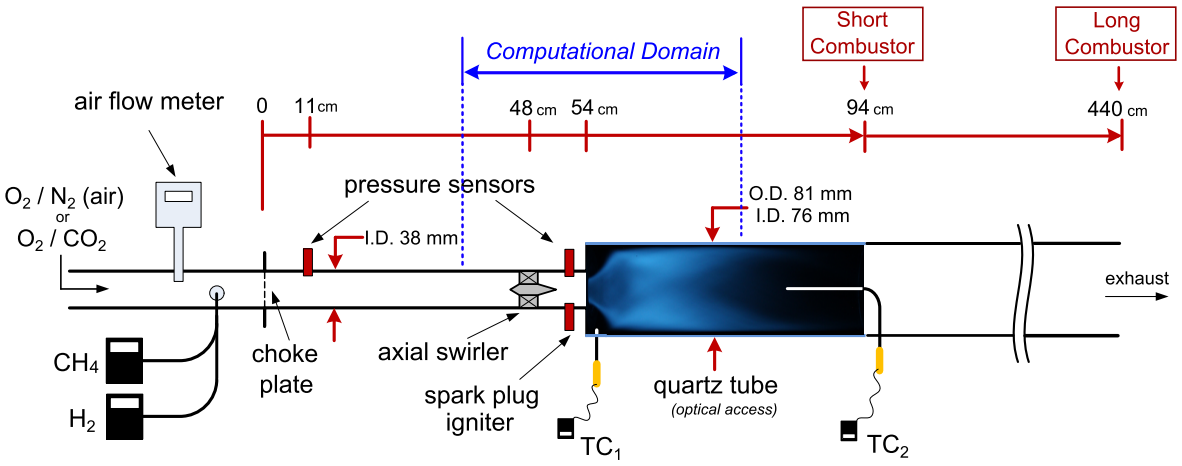


Figure 2-1: Experimental setup showing long and short combustor configurations for acoustic-heat release decoupling. The extent of the LES computational domain is shown.

not be a driving mechanism for any thermo-acoustic instabilities we observe. Second, the use of an orifice plate ensures very good premixedness of the fuel and air before reaching the combustion chamber.

After the choke plate, the mixture flows through a 316 stainless-steel cylindrical pipe with inner diameter of $D_{inlet} = 38$ mm and length $L_{inlet} = 14.2$ x $D_{inlet}$ i.e. sufficient length to reach quasi-full development of the flow. An axial eight-vane swirler with a streamlined centerbody and vane angle $\alpha_{sw}$ (shown in Fig. 2-2) placed at a distance $L_{swirler} = 12.6$ x $D_{inlet}$ downstream of the choke plate and 1.6 x $D_{inlet}$ upstream of the expansion plane is used to provide the flow with an azimuthal component before

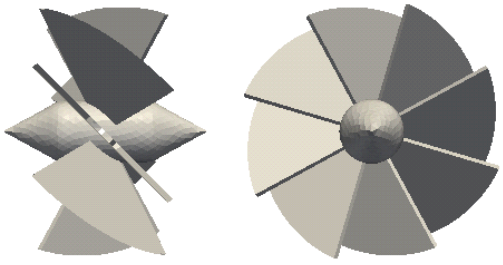

Figure 2-2: Axial eight-vane swirler with 45° vane angle and a streamlined centerbody with a diameter of 9 mm and a 60 ° cone angle.

entering the combustion chamber. Swirling flows are widely used in modern combustors. The vortex breakdown exhibited by swirling flows at some swirl and Reynolds numbers condition is a sought-after feature that contribute to stronger flame anchoring. A comprehensive review of swirling flows was done by Lucca-Negro et al. [60].

After the swirler, the flow passes through a sudden expansion (side wall in 316 stainless steel) from the upstream diameter to a downstream diameter $D_{outlet}$ = 2 x $D_{inlet}$. Sudden expansions are also commonly used in combustion systems as they force flow separation and create additional shear layers and recirculation zones. Finally, the exhaust plane is situated at $L_{exhaust}$ = 115.8 x $D_{inlet}$ downstream of the choke plate. The combustor discharges into a plenum at near atmospheric pressure. The length of the combustor can be changed; this will be done in **chapter**-3 to control the acoustics of the combustion chamber. The reference Reynolds number based on the inlet diameter is $Re_{D_{in}} = 20,000$ while the reference swirler's vanes angle is $\alpha_{sw} = 45$ degree; the corresponding swirl number can be estimated using the expression[3, 38]:

$$S = \frac{2}{3}\ \left(\frac{1-(D_{cb}/D_{in})^3}{1-(D_{cb}/D_{in})^2}\right)\ tan(\alpha_{sw}) \approx \frac{2}{3}\ tan(\alpha_{sw})$$

with $D_{cb}$ the diameter of the centerbody (fixed at 9 mm). This leads to S $\approx$ 0.7 at the reference conditions.

The reference conditions noted above are used throughout this thesis except in **chapter**-4 where $\alpha_{sw}$ is modified from 30 to 60 degrees and Re from 15,000 to 30,000. The pressure is atmospheric and that is the case in all the following investigations in this thesis. At these inflow conditions, a vortex breakdown occurs downstream of the swirler due to an adverse pressure gradient both in the non-reacting and reacting flows, creating a central recirculation zone. The presence of a sudden expansion exacerbates the adverse pressure gradient, stabilizes the axial location of the central or inner recir-

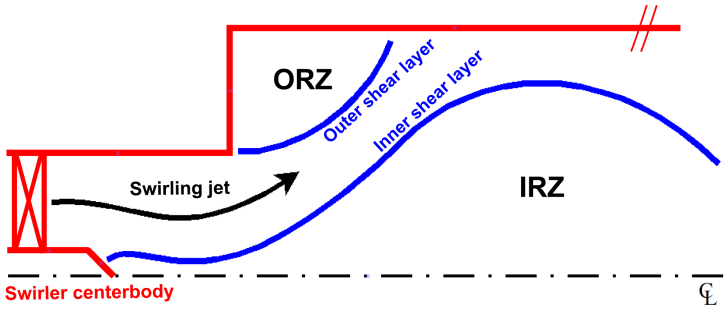


Figure 2-3: Schematic flow field in the swirl-stabilized combustor: outer recirculation zone (ORZ), annular incoming swirling jet and inner recirculation zone (IRZ) regions delimited by the outer and inner shear layers, in the mean flow sense.

culation zone (IRZ) and also creates an additional toroidal recirculation zone outside of the main jet leaving the inlet pipe called outer recirculation zone (ORZ); as we will see later a large part of this thesis will be dedicated to study this region of the flow (in **chapter**-4 and **chapter**-5). An inner and outer shear layers (ISL and OSL) separate the three zones: the IRZ, the annular swirling jet and the ORZ, as shown by Fig. 2-3. The fuels, methane and hydrogen, were supplied by a Sierra C100M Smart-Trak digital mass flow controller with a flow rate uncertainty of 1% of maximum capacity. A Sierra Instruments 780S Flat-Trak flow meter was used to measure the air flow rate with the same uncertainty. Subsequent measurement error on the equivalence ratio is 2%.

### 2.1.2 Diagnostics Tools

The use of multiple, complementary optical diagnostics tools is a key component in the different investigations undertaken in this thesis. We used a two dimensional, two-component (occasionally three-component) high-speed particle imaging velocimetry (PIV) system to interrogate the turbulent flow field in the axial-radial plane. We relied on OH Planar Laser Induced Fluorescence (OH-PLIF) to get the flame location and structure with high spatial resolution. CH* chemiluminescence was recorded using

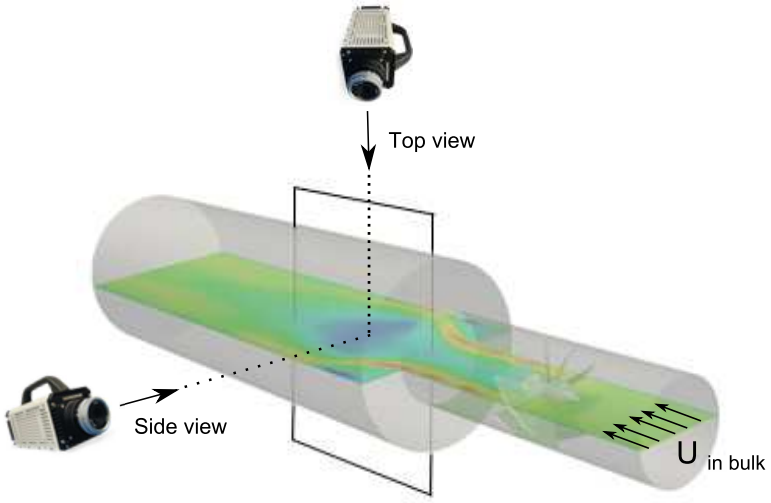


Figure 2-4: Schematic of the dual camera chemiluminescence setup for ORZ flame tracking.

one or multiple high speed cameras, both intensified and non-intensified, to obtained time resolved line-of-sight images of the flame. We also acquired Integral CH* chemiluminescence using a photomultiplier for high temporal resolution. In addition to the above optical diagnostics tools, point pressure and temperature measurements were made.

**Flame Chemiluminescence:**

A Hamamatsu H930602 photomultiplier tube (PMT) was used to record spatially-integrated radiation from the flame at a 10,000 Hz rate starting from the dump plane up to 300 mm downstream (3/4 of the quartz tube length). A 50 mm Nikon glass lens was used along with a band-pass filter (Andover 430FS10-50) centered at 430 nm allowing the selective transmission of CH* radical's radiation. The CH* chemiluminescence fluctuation is normalized by the mean value and considered as a surrogate for the flame heat release [53].

Intermediate (200 Hz) and high speed (1000 Hz) spatially-resolved chemilumines-

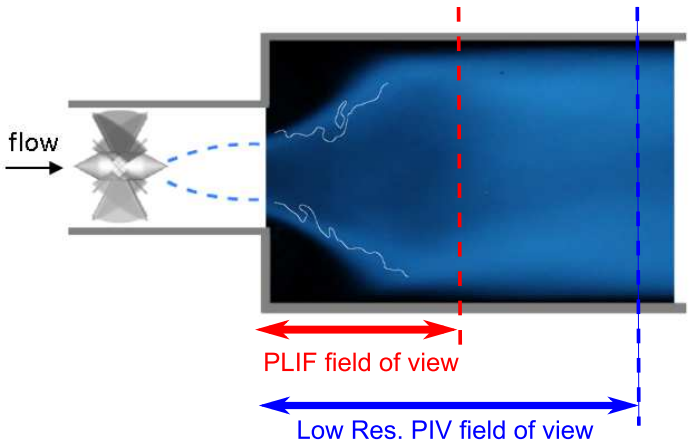


Figure 2-5: Example of flame macrostructure captured using the IR-filtered Canon T3i DSLR with an exposure time of 1/4 s. Example shown for acoustically decoupled methane-air combustion at $\phi$=0.60, Re=20,000 and $\alpha_{sw}$=45 degrees. An instanteneous flame edge extracted from OH-PLIF data (described below) is superimposed. Fields of views of low resolution PIV and OH-PLIF are also displayed.

cence flame imaging with an infrared (IR) blocking filter (a 2-mm thick CG-BG-39 Schott glass) was performed using two NAC GX-1 high-speed CMOS cameras mounted above and on the side the combustor. The use of two cameras — capturing simultaneously the top and side views of the combustor as shown in Fig.2-4 — was critical for our examination of the ORZ flame transition and its tracking in space and time, performed in **chapter**-4. Nikon NIKKOR lenses with a 50mm focal length and an aperture of f/1.2 were used. In some cases, in order to overcome modest signal-to-noise ratio achieved with the cameras mentioned above at relatively low $\phi$, we used an intensified camera HICAM 5000 Gen 3 from Axiom Optics. The HICAM is equipped with a GaAsP (Gallium arsenide phosphide) photocathode which has a electromagnetic sensitivity window from 350 to 800 nm. This camera was used without an IR filter at a frame of 2000 Hz and an exposure time of 0.25 ms.

The flame macrostructures are also recorded using a Canon T3i digital single-lens reflex camera with a larger exposure time (250 ms). When needed, the line-of-sight integrated mean flame chemiluminescence images are deconvolved using an inverse

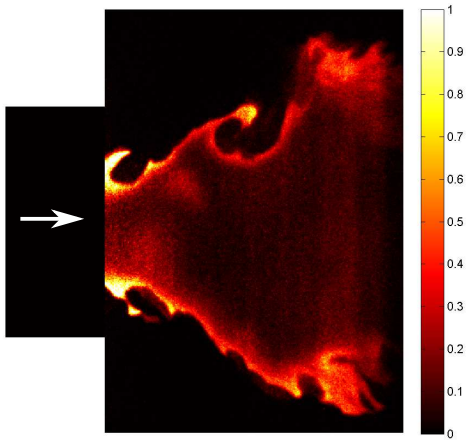


Figure 2-6: Example of OH-PLIF image. Example shown for acoustically decoupled methane-air combustion at $\phi$=0.60, Re=20,000 and $\alpha_{sw}$=45 degrees.

Abel transform in order to mark the location of the flame brush or envelope in the plane crossing the combustor's centerline and perpendicular to the camera. For the ORZ flame analysis, flame chemiluminescence images are not deconvolved due to the non-axisymmetry of the phenomenon, as will be shown later. An example of a non Abel-transformed flame macrostructure is displayed in Fig.2-5.

**OH-Planar Laser Induced Fluorescence:**

Planar Laser Induced Fluorescence (PLIF) images were acquired by exciting OH species at 283.56 nm using a Spectra Physics LAB 170 pump laser (355 nm output) along with a Sirah Cobrastretch dye laser (567 nm output) and a frequency doubler. The dye laser circulates ethanol dissolved Coumarin 153. Fluorescence from excited species returning to ground energy level was optically filtered and intercepted by a 1280 x 1024 pixel LaVision Nanostar CCD camera, with 2 $\times$ 2 binning. OH-PLIF measurements were performed at a 10 Hz rate with a gating time of 100 ns. A laser beam analysis system was used for the spatial and temporal non-uniformity of the laser sheet; it includes a beam splitter that deviates less than 1% of the main laser beam energy

to an Ophir Photonics SP620U CCD camera which records the beam profile for each pulse. The laser sheet profiles are computed from the measured laser beam profiles and the intensities in OH-PLIF images are divided by the correspondent profile to correct for spatial inhomogeneities. An example of a corrected OH-PLIF image is displayed in Fig.2-6.

**Particle Image Velocimetry:**

We used a two dimensional, three-component high-speed particle imaging velocimetry (PIV) system to interrogate the non-reacting flow field giving access to the azimuthal component of the turbulent velocity field. For the reacting cases, only two dimensional, two-component PIV was performed. Aluminum oxide $Al_2O_3$ seeding particles (diameter between 0.9 and 2.2 micron) were introduced into the main air flow upstream of the swirler. A dual pulse 50 W Nd:YLF laser is used along with sheet optics (a spherical lens with a focal length of 1000 mm and a cylindrical lens with a focal length of -20 mm) to produce a light sheet of wavelength 527 nm less than 1 mm thick. A 1280 $\times$ 1024 pixel high-speed NAC GX-1 CMOS camera is used with an F-mount Nikon 60 mm lens to collect the scattered light at a 1 KHz rate. The PIV measurements were processed using the LaVision DaVis 7.2 software. Data using two different fields of view were recorded to obtain different resolutions: one with a relatively large field of view (120 mm $\times$ 76 mm) encompassing the entire width of the chamber as well as the entire inner recirculation zone (dx = dy = 1.4 mm); the other with a narrower field of view (50 mm $\times$ 40 mm) focused on the inner and outer shear layers with a higher resolution of dx = dy = 0.6. At each operating condition, 538 pairs of images were recorded and repeated three times. A statistical uncertainty analysis on the PIV data was performed by computing the standard error of the mean; the mean velocity is computed for each of the three ensembles at the reference inflow conditions and $\phi$=0.60

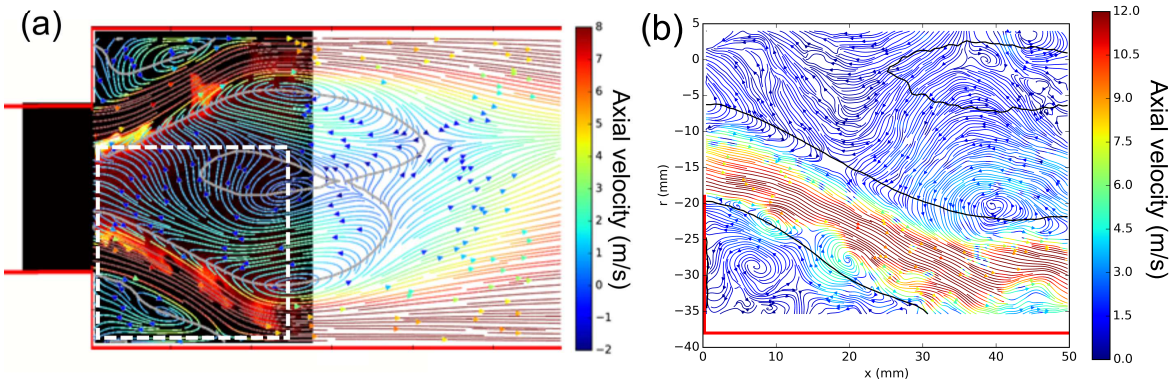


Figure 2-7: Example of (a) Low resolution LR-PIV image and (b) high-resolution HR-PIV. Example shown for acoustically decoupled methane-air combustion at $\phi$=0.60, Re=20,000 and $\alpha_{sw}$=45 degrees. A sample instanteneous OH-PLIF image is superimposed in (a). The box in (a) shows the field of view of the high resolution PIV shown in (b).

at the location of maximum mean axial velocity; we obtained $\mu_1$=12.27 m/s, $\mu_2$=12.37 m/s and $\mu_3$=12.32 m/s leading to a relative standard error of the mean of 1% (with 95% confidence). Examples of a mean PIV data (low resolution) and instanteneous high resolution PIV data are shown in Fig.2-7 (a) and (b), respectively.

**Pressure and Temperature Measurements:**

In addition to optical diagnostics, pressure and temperature measurements were performed. Pressure was recorded at a 10 kHz rate using Kulite MIC-093 transducers between at different locations : one close to the choke plate and one between the swirler and the expansion plane, closer to the flame location. Temperature measurements were performed using K-type sheathed thermocouples ($TC_1$ and $TC_2$). $TC_1$ was inserted through the quartz tube 10 mm downstream of the sudden expansion side wall and 5 mm into the ORZ (see Fig. 4-1). $TC_2$ was inserted downstream on the centerline. $TC_1$ and $TC_2$ have sampling rate of 20 Hz, a sheath diameter of 1/16 inches and a response time around 1 s. Multiple measurements were made to evaluate

an uncertainty of ± 5 K. $TC_1$ data will be used in chapter 4 and 5 to study the effect of heat losses on flame transition to the ORZ and stabilization along the ISL; the goal is to have a better understanding of the thermal conditions in the ORZ. $TC_2$ will be used for comparison with simulations for LES code validation. $TC_1$ is used to measure the relatively low temperature of the unburnt reactants in the ORZ before the appearance of a flame in that zone. The probe measurements can be subject to radiation error from different sources: gas radiation from the combustion products and radiative heating of the probe by the hot chamber wall. Radiation error in $TC_1$ measurements due to gas radiation were neglected for the following reason: by changing the diluent from $N_2$ (air combustion) to $CO_2$ (oxy-combustion) at the same adiabatic flame temperature, the change in $T_{ORZ}$ was within the error margin suggesting limited radiation exchange between the probe and products. The probe measurement was also not corrected for radiation error from hot walls; when comparing $T_{ORZ}$ for different levels of insulation of the chamber (which leads to different wall temperatures), a 30 K temperature difference was measured by the probe. This increase is attributed to the combination of lower heat losses at the boundary and higher artificial heating of the probe by the hot wall. The temperature obtained by the probe are considered as upper bounds for the ORZ gas temperature. $TC_2$ is used to measure the high temperature of the products downstream. This probe is more subject than $TC_1$ to radiation error through radiative cooling by the colder wall and surroundings. A radiation error was estimated to correct the temperature measured by $TC_2$; the correction method is described in **Appendix**-B.

### 2.1.3 Analysis Tools

**Proper Orthogonal Decomposition:**

The proper orthogonal decomposition (POD) is applied to the PIV data. POD — also known as the Karhunen-Loeve decomposition or principal components analysis in other disciplines — is a procedure for extracting a basis for a modal decomposition from an ensemble of signals [4]. It has been first applied to fluid dynamics and turbulence by Lumley[4]. Here we apply a POD algorithm to PIV data for the extraction of coherent velocity and structures from measured turbulent velocity fields. We follow a variant of POD called "method of snapshots" described by Sirovich et al.[89]. An overview of the POD procedure and the equations solved in order to obtain the orthogonal modes is presented here; more details can be found in the review by Berkooz et al.[4] . The 2D PIV data for axial (u) and radial (v) velocities ($N_x \times N_y$ points) over time ($N_t$ snapshots) is rearranged in a matrix $\mathbf{U}$ (of size $[N_x+N_y] \times [N_t]$). The symmetric positive definite correlation matrix $\mathbf{C} = \mathbf{U}^T.\mathbf{U}$ is then computed. $\mathbf{C}$ is orthogonally diagonalizable and the eigenvalue value problem $\mathbf{C}.\mathbf{a}_k = \lambda_k a_k$ solved . The outcome of the POD method is the sets of temporal eigenfunctions ($a_k$), spatial eigenfunctions (or modes $\phi_k = U.a_k$) and eigenvalues $\lambda_k$; the latter represents the portion of kinetic energy associated with each mode. The POD analysis results will be shown in **chapter**-6.

**Extinction Strain Rate Calculations:**

The extinction strain rate ($\kappa_{ext}$) is a fundamental flame property that will be used in this thesis to compute a characteristic time scale for premixed flames. $\kappa_{ext}$ calculations are performed in CHEMKIN-PRO [77] using a two-dimensional premixed twin-flame configuration. Air-flames kinetics for $CH_4$-$H_2$ combustion are modeled using the commonly used GRI 3.0 mechanism [90]. The oxy-flames kinetics (used in **chapter**-5) were

modeled using the mechanism proposed by Mendiara and Glarborg [64] which was recently developed specifically for methane oxy-combustion. This choice is based on a better agreement when comparing experimental non-premixed extinction strain rates by Maruta et al [63] and calculations using both GRI 3.0 and Glarborg mechanisms.

In this thesis, all extinction strain rate calculations relied on multicomponent transport properties and included the Soret effect. Gaseous radiation for oxy-flames was included using the optically thin radiation model available in CHEMKIN-PRO. Estimates of the effect of radiation led to an 11% and 4.2% error when neglecting radiation in oxy-combustion at $\phi$=0.55 and $\phi$=0.65, respectively. The correspondent errors for air-flames were estimated at 1.3% and 0.5%. Therefore, we included radiation in oxy-flames computations and neglected it for air-flames.

## 2.2 Large Eddy Simulations

### 2.2.1 LES Setup

**Governing Equations, SGS Models and Discretization:**

A truncated domain from the above experimental setup is modeled and meshed to perform Large Eddy Simulations. The truncated domain includes the swirler which is exactly represented in the numerical setup (imported from the same CAD[1] file used to manufacture the swirler) and about half of the combustion chamber (225 mm out of 400 mm of the round quartz tube is modeled); the extent of the numerical domain can be seen in Figs.2-1 and 2-8. The LES code is similar to the one described in previous studies by Kewlani et al. [44, 45]. This code was implemented using OpenFOAM's C++ libraries based on a finite volume method for spatial discretization. An implicit

[1]Computer-Aided Design

second order temporal schemes is used along with a combination of first and second order schemes for spatial discretization balancing numerical stability and accuracy. Few differences with the previous work relate to the grid, the choice of numerical schemes and the parameter choice for the combustion model.

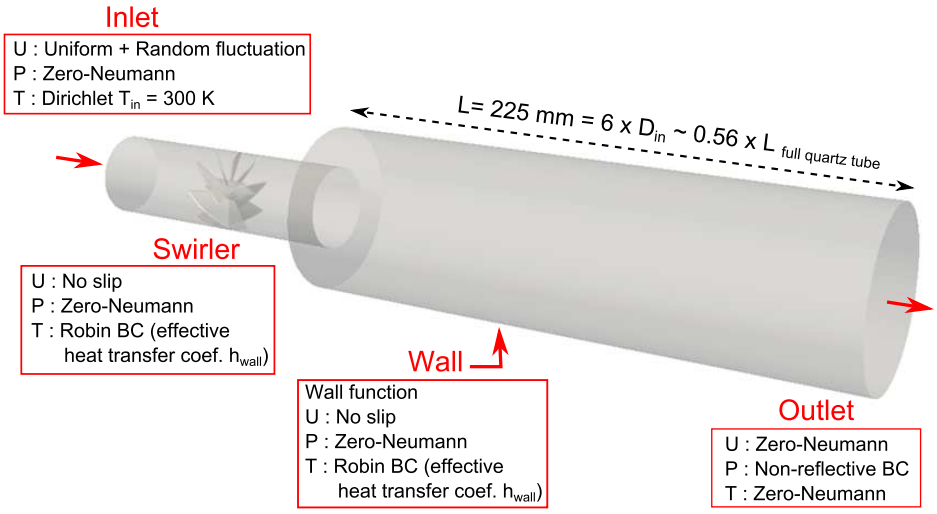


Figure 2-8: LES computational domain and boundary conditions

The partial differential equations (PDE) governing the flow are the mass, linear momentum, and sensible enthalpy conservation, closed using the ideal gas law as equation of state. The LES Favre-filtered governing equation are detailed in the appendix along with different approximations and modeling steps made. Reactions are taken into account using a reduced mechanism of Jones & Lindstet [41] containing 7 species and 5 reactions that gives an acceptable approximation of the adiabatic flame temperature and the laminar burning velocity in a laminar premixed flame setup. Each species require an additional PDE to be solved. The residual subgrid scale stress tensor is closed using the Prandtl's one equation model based on the turbulent kinetic energy (TKE) which uses the Boussinesq eddy viscosity postulate. The filtered reaction rate is closed using an Arrhenius rate law similar to a DNS approach which is one of the advantage of the artificially thickened flame combustion model (ATF) used here. In the

ATF model, a thickening factor F multiplies the flame thickness and the effective (sum of molecular and SGS: $D_{eff}$) diffusivities maintaining the propagation of the flame locally at the laminar burning velocity. Such a thickened flame can then be resolved on the numerical grid in a DNS-like approach. Because of the change in thickened flame response to the turbulent flow, an efficiency function E is used to recover the flame-flow interaction and heat release. This efficiency function is implemented following the algebraic expression proposed by Colin et al.[14]. A dynamic thickening approach is implemented here where F and $D_{eff}$ scalars are used to build associated fields ($F_{loc}$ and $D_{eff,loc}$) that depend on the location relative to the flame. In the ATF combustion model, the filtered species conservation becomes (with $\widetilde{Y}_k$ the filtered mass fraction of species k):

$$\frac{\partial \overline{\rho}\widetilde{Y}_k}{\partial t} + \frac{\partial \overline{\rho}\widetilde{u}_i\widetilde{Y}_k}{\partial x_i} = \frac{\partial}{\partial x_i}\left(\overline{\rho}F_{loc}ED_{eff,loc,k}\frac{\partial \widetilde{Y}_k}{\partial x_i}\right) + \frac{E\overline{\dot{\omega}_k}}{F_{loc}} \tag{2.1}$$

The dynamic thickening uses $F_{loc}$ and $D_{loc}$ calculated as follows:

$$F_{loc} = 1 + (F-1)\Psi(c) \tag{2.2}$$

$$D_{loc} = \frac{\mu}{Sc}EF_{loc} + (1-\Psi(c))\frac{\mu_{sgs}}{Sc_{sgs}} \tag{2.3}$$

$$\tag{2.4}$$

with $\Psi(c) = 16[c(1-c)]^2$ and $c = \left(1 - \frac{Y_{fuel}}{Y_{fuel}^{inlet}}\right)$ the progress variable. $\mu$ and Sc are the dynamic viscosity and the Schmidt number respectively. The efficiency function is calculated using the local filter width $\Delta$, the unstretched laminar burning velocity $S_L^0$, the laminar flame thickness $\delta_L^0$ and thickened flame thickness $\delta_L^1$ and the local SGS velocity fluctuation $u_\Delta^{'}$ following the expression suggested by Colin et al.[14]:

$$E = \frac{\Xi(\delta = \delta_L^0)}{\Xi(\delta = \delta_L^1)},$$

with the non-dimensional wrinkling factor $\Xi$:

$$\Xi(\delta) = 1 + \alpha \left( \frac{2ln(2)}{3C_{ms}(Re_t^{1/2} - 1)} \right) \left( \frac{u'_\Delta}{S_L^0} \right) \Gamma \left( \frac{u'_\Delta}{S_L^0}, \frac{\Delta}{\delta_L^0} \right)$$

and,

$$\Gamma \left( \frac{u'_\Delta}{S_L^0}, \frac{\Delta}{\delta_L^0} \right) = 0.75 \left( \frac{\Delta}{\delta_L^0} \right)^{2/3} exp \left[ -1.2 \left( \frac{u'_\Delta}{S_L^0} \right)^{-0.3} \right]$$

### 2.2.2 Computational Domain, Grid and Boundary Conditions

The computational domain and the main boundary conditions are summarized in Fig.2-8. A mixed tetrahedral and hexahedral mesh is constructed. The tetrahedral mesh is used around the swirler to better capture all its geometrical details. The grid is created denser around the combustion chamber expansion plane and a larger grid size is employed as we move downstream. The grid size is 0.65 million cells with an average cell sizes of : $\overline{\Delta x} = 1$ mm , a maximum and minimum cell size of $\Delta x_{max} = 1.6$ mm and $\Delta x_{min} = 0.32$ mm , respectively. The average cell size imposed a choice of a thickening factor F used by the combustion model. As the filter size ($\Delta$) was taken to be the cell size, a thickening factor F = 3 was chosen to allow approximately five grid points across reaction zone to have an acceptable resolution of the thickened flame :

$$F \times \frac{\alpha_{th(800K)}}{S_{L\ (\phi=0.6)}^0} \approx 5 \times \overline{\Delta x} \tag{2.5}$$

where $\alpha_{th}$ is the thermal diffusivity and $S_L^0$ is the laminar unstrained flame speed.

Grid sensitivity tests were performed for a 2 million cells grid. The computational time increased by a factor of three approximately. The results (not reported in this thesis for brevity) did not show a measurable improvements when compared to experiments to justify the increase of computational time. Computational time using the fine grid was too long to allow a practical use of LES in this case. Similar grid sensitivity tests can be found in previous work [44, 45].

The thermal boundary condition used at the wall is a Robin (mixed) type boundary condition that takes into account an effective external heat transfer coefficient ($h_{wall}$ in $W.m^{-2}$); Different values of $h_{wall}$ were tested: $h_{wall}$= 0 $W.m^{-2}$ (adiabatic), $h_{wall}$= 25 $W.m^{-2}$, $h_{wall}$=50 $W.m^{-2}$ and $h_{wall}$= 100 $W.m^{-2}$; the final results shown in this thesis were obtained with $h_{wall}$=50 $W.m^{-2}$. Radiative heat transfer within the gases and with the wall is neglected; This choice is based on a simplified one-dimensional heat transfer model used to estimate the major heat transfer mechanisms taking place at these conditions. For the reacting case studied in this thesis, the total power input is equal to 19.8 kW. Of this power input, about 18% was estimated to be lost by forced heat convection to the wall and 4% by radiation, by the end of the quartz tube. Details about this estimate can be found in appendix.

### 2.2.3 LES Code Validation

**Importance of Inflow Conditions:**

As a first step towards LES validation, the sensitivity to the inflow boundary conditions was experimentally and numerically tested for the non-reacting flow. In order to evaluate the sensitivity of our experimental setup to the turbulent inflow conditions, a flow straightener was added between the choke plate and the swirler. We compared the mean and rms flow fields obtained from PIV for the two cases with and without flow

straightener; only a negligible difference (less than 7% in average) in flow statistics was recorded; moreover, a slight change (less than 3%) in the dominant peak in the power spectra (corresponding to the precessing dynamics as we will see later) falling below the experimental uncertainty. The same experiment was performed by removing the swirler (non-swirling jet flow) and a large difference in flow field was noted resulting in a substantially different potential core length and vortex rings. This comparison shows the role of the axial swirler with narrow vane gap in acting as a flow straightener itself: despite large changes in the flow filed, as reflected by PIV when the swirler is removed, the swirler blades reset the flow and turbulence to a same level. The above result was accompanied with a comparison of simulation results when using experimental inflow profile (from PIV) or a simpler plug flow with added random white noise. The results showed also only a small difference, as expected from the experimental results. The sensitivity to the inlet conditions was dramatic only for the simulated non-swirling jet, also expected from the experiments. These results provide a first validation of the code and the chosen inflow conditions; they also limit the need for advanced and more accurate prescription of turbulent inlet velocity boundary condition for LES calculations in the geometry of interest here.

**Turbulent Flow Fields Statistics:**

The turbulent flow field for the two reference cases (Non reacting and reacting) is compared with the experimental data. The results are shown in the Appendix where an acceptable agreement between the simulations and experimental data can be seen. Few discrepancies exist and will drive future improvements : first, while the velocity fluctuations are well captured in the cold flow, the local deviation between experiment and LES calculations for the reacting case is larger; but the overall fluctuation levels and trends are still acceptably reproduced. Second, the average location of the stag-

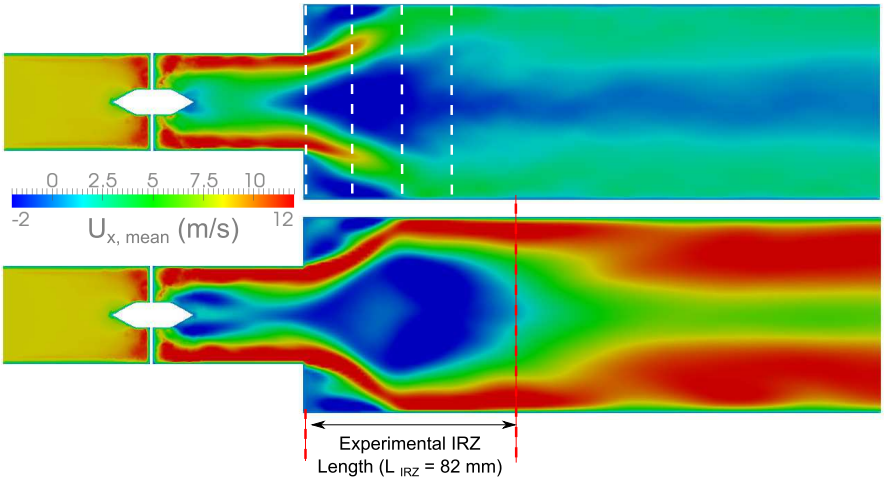


Figure 2-9: LES of Axial velocity contours of the non-reacting (top) and reacting (bottom) cases. The dotted lines in the top part represent the location of the velocity profiles used for LES validation. The dotted line in the bottom part locates the experimental position of the downstream stagnation point i.e. the length of the vortex breakdown bubble.

nation point is not exactly captured by LES; for the non-reacting flow, the experiment shows the stagnation point to be located right at the expansion plane whereas the simulation predicts the average stagnation point location to be upstream, inside the inlet tube. These discrepancies are considered minor here. The important features successfully captured by the LES calculations are shown in Fig.2-9; the figure compares the axial velocity contours obtained for the non-reacting and reacting cases using LES. The vortex breakdown in the non-reacting swirling flow (Fig.2-9-top) leads to an open recirculation zone suggesting a cone-type vortex breakdown [81, 5]; there is no downstream stagnation point within the field of view and the negative axial velocity region extends downstream. This compares well with the experimental PIV data. The non-reacting case shows also the presence of a comparatively small recirculation zone in the wake of the centerbody (this cannot be confirmed using experimental data as the optical access is restricted to be only downstream of the expansion plane). For the reacting case, we see that the simulated vortex breakdown features a closed “bubble"

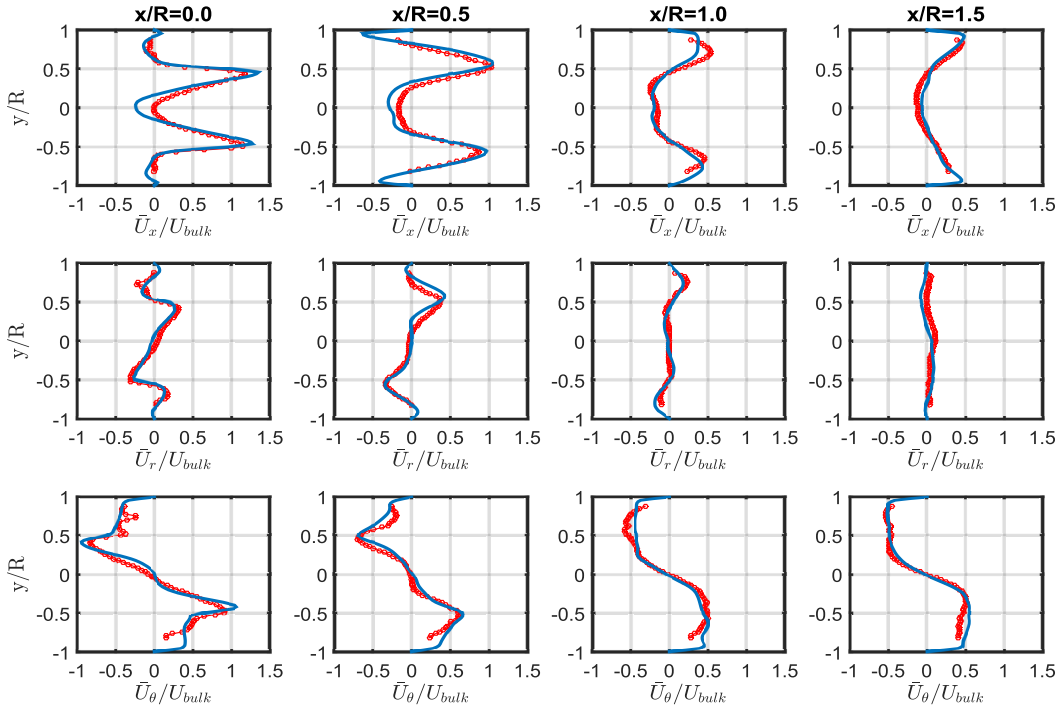


Figure 2-10: Non-reacting Mean velocity profiles: Exp. (red circle) vs. LES

recirculation zone which is also observed in the experiment; in Fig.2-9-bottom, one can see that the extent of the experimental and numerical recirculation zones compare fairly well. Additionally, LES shows that the recirculation zone bubble merges with the centerbody's smaller recirculation zone. LES predicts the flame anchoring to be at the centerbody which was visually confirmed in the experiment; by merging, the two recirculation zones create one tubular shear layer along which the flame can be stabilized.

**ORZ and Downstream Temperature:**

Temperature measurements are now compared to LES predictions for the reacting case ($\phi$=0.60) as an additional validation step; the steady state time averaged temperatures in the ORZ ($TC_1$) as well as downstream ($TC_2$) were probed at the locations shown in Fig.2-14-c. The temperature downstream was corrected for radiative heat exchange

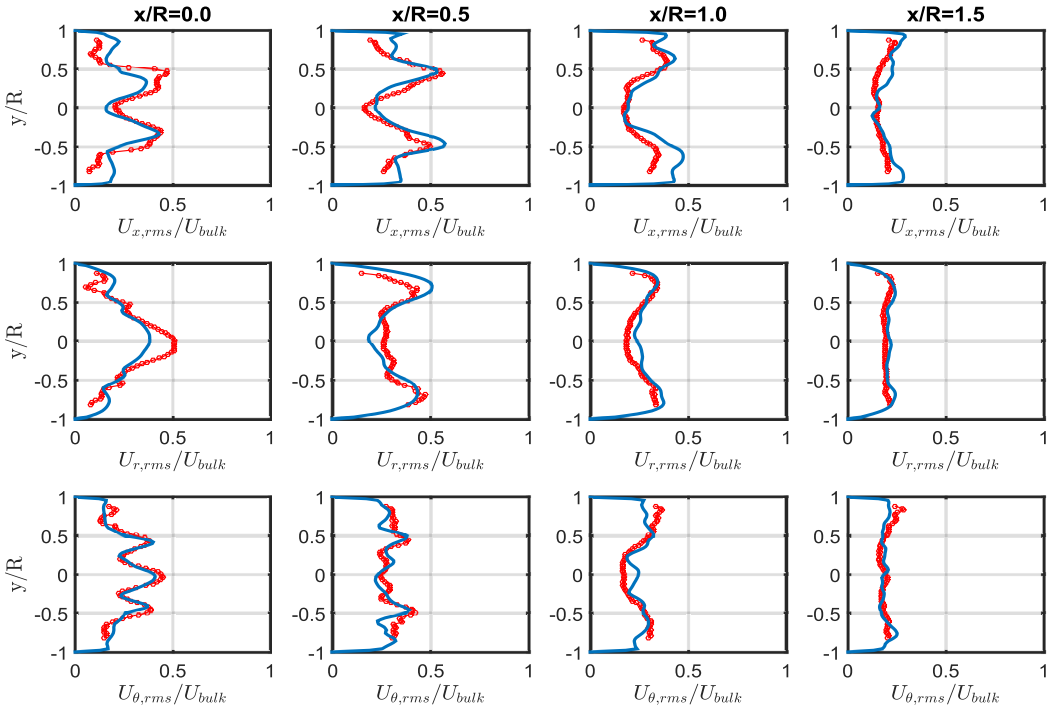


Figure 2-11: Non-reacting RMS velocity profiles: Exp. (red circle) vs. LES

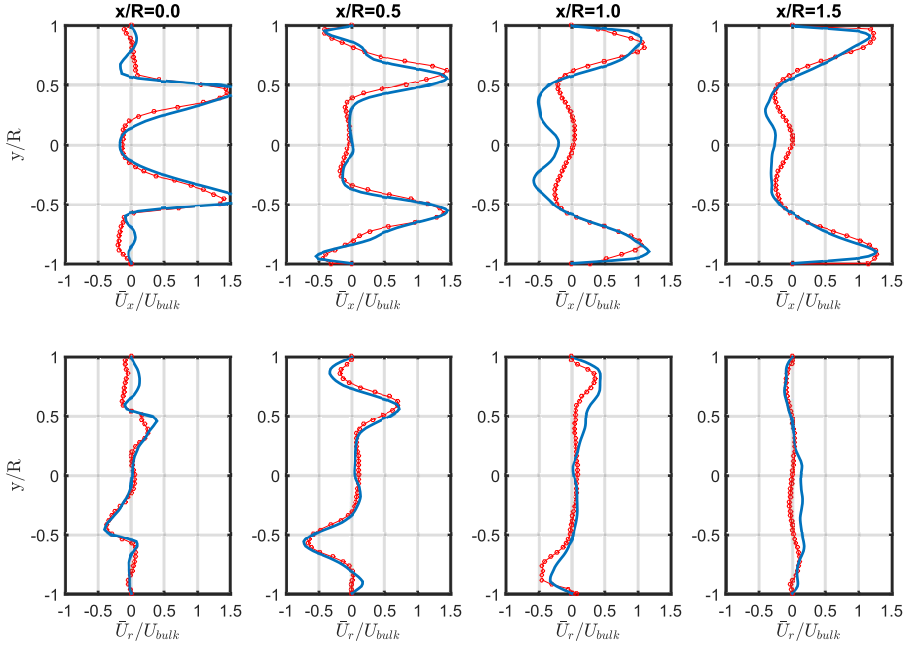


Figure 2-12: Reacting ($\phi$=0.6) Mean velocity profiles: Exp. (red circle) vs. LES

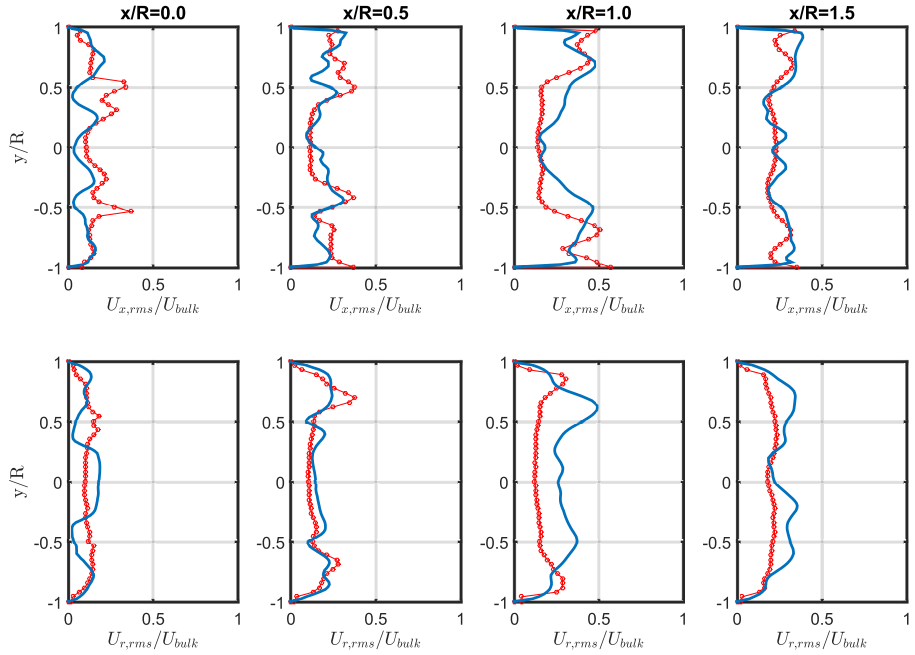


Figure 2-13: Reacting ($\phi$=0.6) RMS velocity profiles: Exp. (red circle) vs. LES

between the probe and the relatively colder wall. The correction method is detailed in Appendix. The LES temperature results and comparison with experiment are shown in Fig.2-14-a for the ORZ temperature and (c) for the downstream temperature.

Although the inlet temperature is ambient and no combustion is occurring in the ORZ, the measured value for the reactants recirculating in the ORZ is equal to 410 K $\pm$ 5 K. The simulations predict a temperature $T_{ORZ,\,LES}$=423 K which is in good agreement with the experiment (see Fig.2-14-a) but also give us an insight on the mechanism responsible for this temperature rise. Before reaching the ORZ, the fluid particles travel along the swirling jet separating the IRZ and the ORZ. The jet impinges the wall and splits into two parts: one continues downstream and one recirculates back into the ORZ. The flame is adjacent to the incoming jet as it is stabilized along the ISL; the reactants are thus preheated as they are convected along the jet. The residence time along this incoming jet (governed by both Re and S) governs the level of preheating. As radiation was not taken into account in this model and the computed temperature

shows a good agreement with the experimental data, it is plausible that convective heating of the jet is the main mechanism responsible for the ORZ heating.

The downstream temperature measurements using $TC_2$ give a steady state average temperature $T_{probe}$=1185 K; the temperature of the gas (corrected for radiative loss as shown in Appendix) is estimated at $T_{gas}$=1420 K. This deviation from the adiabatic flame temperature ($T_{ad,\ \phi=0.6}$=1660 K) is predominately due to convective heat losses at the chamber wall; LES simulated temperature at the same location is 1520 K, 100 K lower than the corrected experimental temperature. This deviation is likely due to neglecting losses from combustion products; this will be also an area of future improvement.

**Conclusion of the LES Validation Step:**

The comparison of the flow field statistics (mean and rms) as well as the ORZ and downstream temperature between experiments and simulations shows a fairly good and acceptable agreement although some discrepancy could be noted. The highly unsteady nature of such flows requires also comparison of time dependent features. This will be done in **chapter**-6, eventhough the purpose of the chapter is not purely validation but rather the extraction of information from simulations that cannot be retrieved experimentally using two-dimensional optical diagnostics.

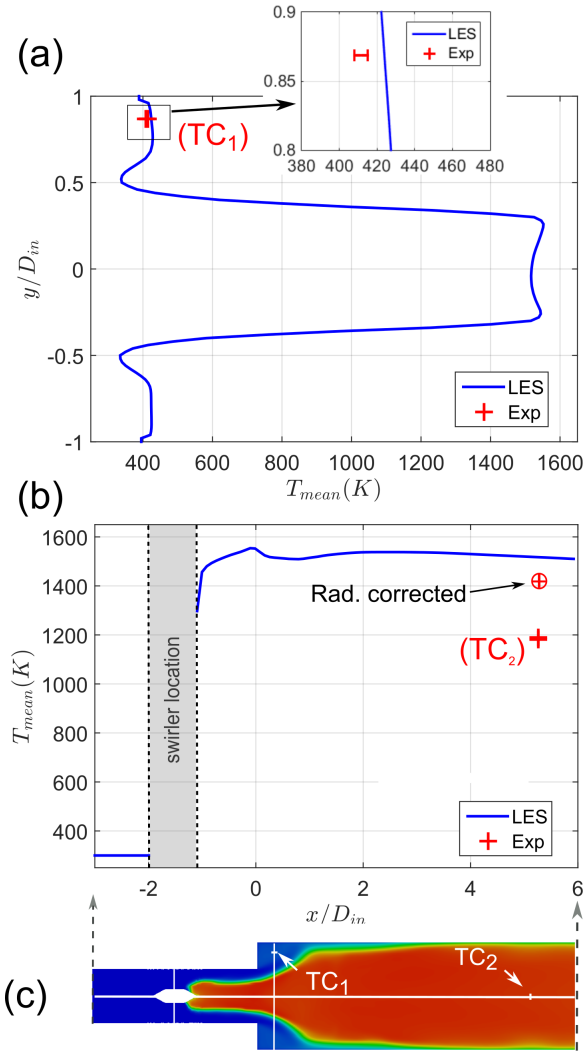


Figure 2-14: Comparison of Experimental and LES temperature in: (a) the ORZ ($TC_1$) and (b) along the combustor's centerline ($TC_2$). the location of $TC_1$ and $TC_2$ is shown in (c). The expansion plane corresponds to $x/D_{in} = 0$. The LES mean temperature contours are shown in (c) with the extracted temperature profiles location.

# Chapter 3

# Onset of Thermo-acoustic Instabilities

## 3.1 Chapter Overview

It has been suggested that combustion instability in swirl-stabilized combustors is associated with a change in the flame position and shape, or macrostructure[91] [20]. In this chapter, we investigate this link in more detail. This work comes as a natural extension of the work of Speth et al. [91, 92] in which the classical Rayleigh criterion was evaluated for different dynamic modes and a similarity parameter capturing the flame response to flow oscillations for different fuel compositions was proposed. We document the different flame macrostructures under acoustically coupled conditions and their close similarities to those observed under acoustically uncoupled conditions; how the transitions between the different configurations occur at the same equivalence ratio in both cases and the link between these transitions and the onset of thermo-acoustic instabilities. We will also investigate the role of fuel composition in determining the equivalence ratio at which the transitions among the different configurations occur.

The chapter is organized as follows: first we analyze the link between acoustically decoupled flame macrostructures and the onset of thermo-acoustic instability . This

will constitute the bulk of the chapter; we present the approach we followed. Then, we analyze the dynamic stability map of the combustor using pure methane and draw the correspondence with the changes in the flame macrostructure as the equivalence ratio is raised. Changing the combustor length without affecting the underlying flow allows the decoupling of the acoustics over an equivalence ratio range of interest. A comparison of the long coupled case and the short uncoupled case is performed. Fuel composition effect, via $H_2$ addition, on dynamic modes and flame configurations will be also investigated and used as a method to confirm and generalize our findings; Next, we propose an interpretation of the results based on a simple analysis of the non-linear characteristics of the constructed stability maps. Finally, for reasons that will become clear later in this chapter, we analyze in more detail the flame transition to the ORZ.

In this chapter, only the equivalence ratio and the hydrogen volume fraction in the fuel, for two combustion chamber lengths, have been modified, while all the other parameters were held constant at the reference conditions (Reynolds number Re = 20,000 and $\alpha_{sw} = 45$ deg.).

## 3.2 The link Between the Onset of Thermoacoustic Instability and Flame Macrostructures

### 3.2.1 Approach

First, we take measurements in the long, acoustically coupled combustor. Next, and in order to examine the onset of unstable thermo-acoustic modes and investigate their potential triggering and driving mechanisms, we decouple heat release from the reacting flow from the acoustic field by reducing the combustor length. The length modification alters the original combustor's resonant frequencies without changing the underlying

flow. Figure 2-1 shows the two lengths of the combustors considered. For each combustor length and fuel mixture, we follow the same experimental protocol: we increase the equivalence ratio from near the lean blowoff limit (LBO) up to 0.75. Each increment of $\delta\phi = 0.01$ is maintained for a 10s interval. The 10s duration is chosen to ensure both stabilization of the equivalence ratio around the target value and steady state thermal boundary conditions. In this section, only changes when increasing the equivalence ratio were investigated. In the following section (section-3.3), we will also construct the stability maps for decreasing equivalence ratio to test non-linear properties of the system (hysteresis).

### 3.2.2 Dynamic Instabilities and Flame Macrostructures

The stability map of pure methane combustion in the atmospheric pressure swirl-stabilized combustor is determined first: we increase the equivalence ratio from near the lean blowoff limit (LBO limit at 0.47 for pure methane in these conditions) up to 0.75 (below flashback). Each increment of $\delta\phi = 0.01$ is maintained for a $\delta t = 10$ seconds interval. This value is chosen to allow enough time for the equivalence ratio to stabilize around a set point and to provide a large enough Fourier number to ensure close to thermal steady state at the boundary ($F_o = \frac{\alpha_{quartz}\delta t}{\delta^2_{quartz}} \approx 2$).

At low equivalence ratios - close to LBO limit - combustion is stable and the recorded pressure fluctuation is relatively low (oscillating between $\pm 50$ Pa). As the equivalence ratio is raised the first unstable mode appears, before the combustor becomes quiet again. A further increase in the equivalence ratio leads to a second unstable mode. Figure 3-1 (b) shows the evolution of the pressure fluctuations upstream of the swirler as the equivalence ratio is raised. The solid line on the left corresponds to the lean blowoff limit. Figure 3-1 (c) shows the associated spectrogram on which we can differentiate five regions. The first region extends from lean blowoff until $\phi \sim 0.55 - 0.56$. In this

range, combustion is stable with a broadband turbulent combustion noise. No coupling with the acoustic field is taking place. Starting at $\phi = 0.56$ pressure fluctuations with a 38-40 Hz dominant harmonic but still with low amplitude appear. A weak coupling between combustion and the acoustic field takes place. As the equivalence ratio is raised further, a transition to the first unstable mode with a 40-42 Hz dominant frequency and large sound pressure level (around 145 dB) takes place. The onset of this instability occurs around $\phi = 0.61$. This "quiet" zone extends for a $\Delta\phi \approx 0.03$ beyond which a quasi-stable combustion appears again, similar to the quasi-stable region observed for $\phi \in [0.56 - 0.61]$. When the equivalence ratio reaches $\phi$=0.68, an abrupt increase of the sound pressure level occurs and a dominant oscillatory component appears at 117 Hz with a large sound pressure level around 150 dB. Table 3.2.2 summarizes the characteristic of the different regions observed. Similar dynamic modes have been previously reported by Speth et al. [91] using different syngas mixtures in a similar geometry.

The spatial distribution of the flame brush changes as the equivalence ratio is raised. The mechanisms underlying these changes are still not fully understood. In the current chapter we do not attempt to explain the reasons behind the transition between flame configurations but we focus instead on establishing the relationship between the mean flame configurations and the dynamic modes observed at the same conditions.

Figure-3-1 (a) shows the sequence of mean flame configurations observed. For a fixed swirl and Reynolds numbers, the flame configuration changes, along with the sound pressure level observed earlier. The transitions in mean flame configurations are marked by the vertical dotted lines in Fig. 3-1(b) and (c). At low equivalence ratio, close to the lean blowoff limit, the flame appears in a columnar shape in the shear layer delimiting the vortex core downstream of the vortex breakdown (flame I). As the equivalence ratio increases, the columnar distribution gets wider and a transition

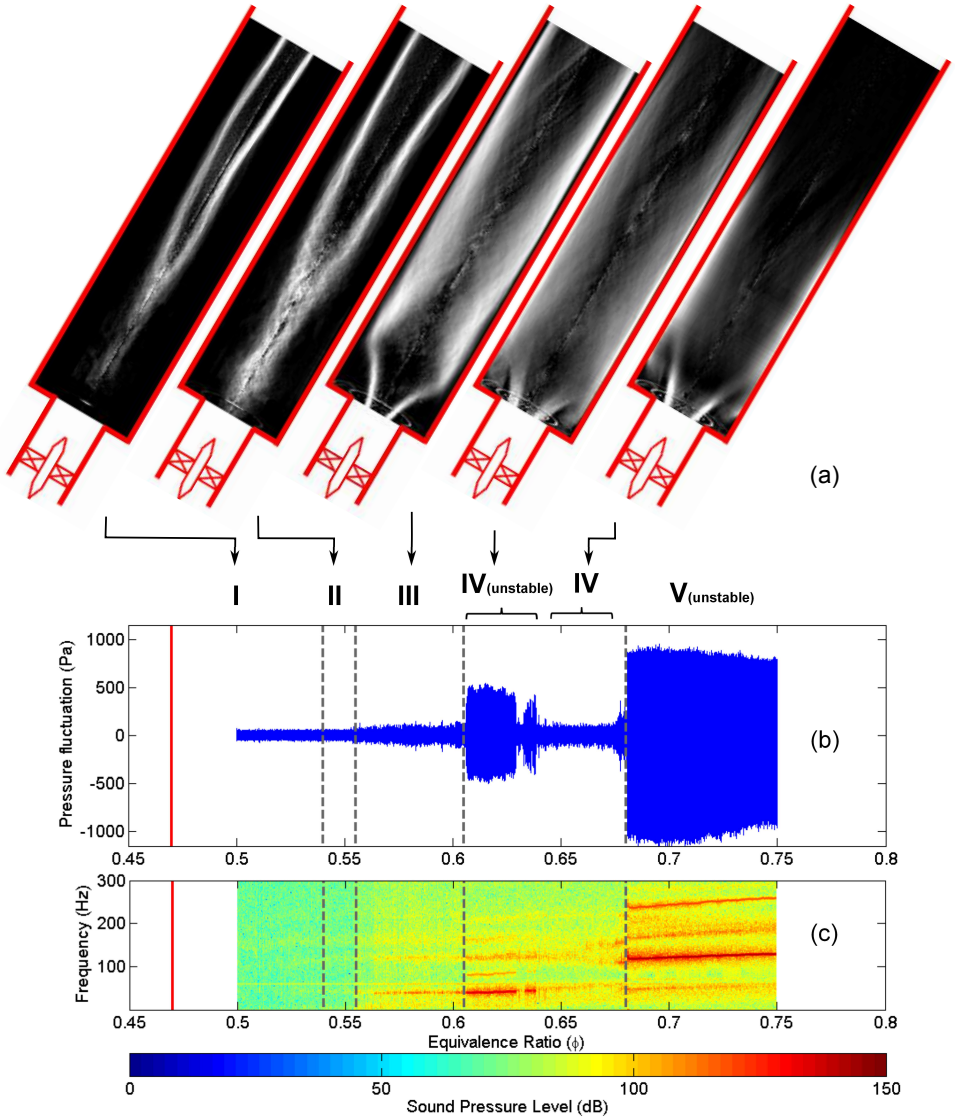


Figure 3-1: Correspondence between the flame macrostructures and thermo-acoustic in the long combustor for 100% $CH_4$ with increasing $\phi$. (a) Flame macrostructures (I to IV, V not shown). (b) Pressure fluctuations. (c) Spectrogram. The vertical solid line represents the LBO limit and dotted lines represent the transitions between macrostructures.

occurs at a certain value of the equivalence ratio ($\phi \sim 0.54$). The flame propagates inside and around the vortex breakdown bubble as well as along the shear layer defining the portion of the vortex core upstream of the breakdown (flame II). The flame is observed to extend inside the inlet tube reaching the swirling centerbody. This flame exist in a very relatively narrow range of equivalence ratio. The downstream portion of the flame is still columnar, similar to flame I, but with a larger diameter. Flame III appears suddenly (i.e. change occurs within a $\Delta\phi$=0.01). In this configuration, the flame brush appears close to the combustion chamber wall boundary layer. The major difference with the previous configuration is that combustion is not taking place inside the inner recirculation zone. A comparison between the mean flame chemiluminescence and the pressure measurement (see Fig.3-1) shows that this transition (II to III) is accompanied by the transition from stable to quasi-stable dynamic mode (region 2 to 3 described above) i.e. to the weakly oscillating 40 Hz mode. Increasing the equivalence ratio leads to a more and more compact flame but still with the same overall mean configuration, i.e. still flame III. At an equivalence ratio between 0.6 and 0.61, the onset of the $1^{st}$ unstable mode is accompanied by a flame configuration change. The flame transitions from configuration III to a configuration IV where on average the flame appears along the inner shear layer but also extends to the ORZ and OSL. When combustion becomes quasi-stable again (region 4 in table 3.2.2), the flame on average still appears in the inner shear layer, extending close to the wall, and remains also in the ORZ. At higher equivalence ratio, the sudden sound pressure level jump happens simultaneously with another transition in the mean flame structure. This corresponds to another configuration (flame V). The latter configuration is highly unsteady, oscillating at higher frequency, starting around 117 Hz. Flame V is not shown here and a phase-average analysis is more appropriate for this highly unsteady flame but this is out of the scope of the current study.

| Region | $\phi$ | Dominant Frequency | Stability | Macrostructure |
|---|---|---|---|---|
| 1 | 0.50 - 0.555 | broadband | S | I & II |
| 2 | 0.555 - 0.61 | $\sim$ 38 to 40 Hz (low amplitude) | QS | III |
| 3 | 0.61 - 0.64 | $\sim$ 40 to 42 Hz | $1^{st}$ U | IV |
| 4 | 0.64 - 0.67 | $\sim$ 48 to 55 Hz (low amplitude) | QS | IV |
| 5 | 0.67 - 0.75 | $\sim$ 117 to 129 Hz | $2^{nd}$ U | V |

Table 3.1: Characteristics of dynamic modes for the long combustor.

Superposing the sound pressure level and the mean chemiluminescence signal from the flame in Fig.3-1 shows a clear correspondence between the mean flame distribution - as reflected by the flame macrostructures I to V - and the dynamic behavior of the combustor. Some transition in flame macrostructures did not change the acoustic energy of the combustor (flame I to II) whereas other transitions (II to III and III to IV) were accompanied by a measurable change. It is important to see here that the first appearance of a continuous flame front in the ORZ (flame IV) as the equivalence ratio is raised matches with the onset of the first unstable mode. Moreover, flame IV can be unstable and quasi-stable. This is similar to the "noise island" previously reported by Fritsche and co-workers[21].

**The "Quiet" Zone:**

The stability map of the acoustically coupled system (long combustor) using pure methane is shown again with the equivalence ratio as parameter (everything else held constant). The sound pressure level is computed from the acquired pressure signal and shown in Fig.3-2-(a) for increasing equivalence ratio. As previously shown, thermo-acoustic coupling starts at $\phi$=0.61 which is the onset of the first limit cycle oscillations (LC-1-up). A "quiet zone" then exists before the onset of the second limit cycle. The frequency of the limit cycle oscillations is shown in Fig.3-2-(b): the first limit cycle

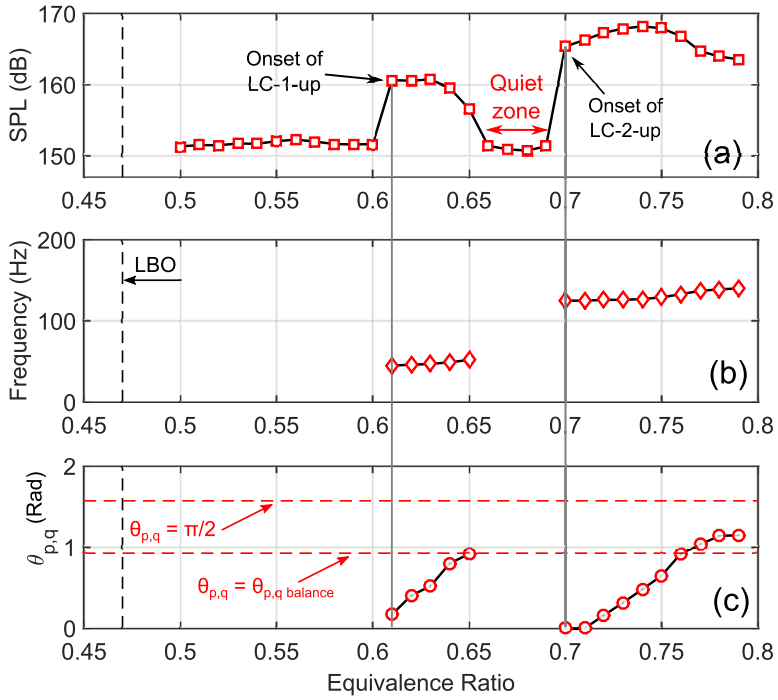


Figure 3-2: (a) Sound pressure level, (b) frequency and (c) the phase (in Rad) between pressure and heat release rate recorded while raising the equivalence ratio. Pressure recorded upstream of the swirler. LC-1-up/down stands for the first limit-cycle as $\phi$ is raised/lowered.

around 40 Hz (LC-1-up) and the second around 120 Hz (LC-2-up).

The phase between the pressure and heat release rate fluctuations is now computed and added to the plot in Fig.3-2-(c). At the onset of LC-1-up, the phase $\theta_{p,q}$ is close to 0 rad; it increases gradually with the equivalence ratio. At $\phi$=0.65, the phase reaches a value of $\theta_{pq,balance} = \pi/3.3$ where the sound pressure level decreases and the combustor becomes stable again. This is the value beyond which the acoustic energy losses balance the added acoustic energy due to pressure-heat release coupling, leading to the reduction in the total acoustic energy; this causes the "quiet zone" i.e. the low noise interval between $\phi$=0.65 and $\phi$=0.70. Theoretically, if the system does not experience any acoustic losses, this value of $\theta_{pq,balance}$ should be equal to $\pi/2$. This is also a way to estimate the system's acoustic energy losses. At $\phi$=0.70 the onset of

the second limit cycle oscillation (LC-2-up) takes place starting with a zero phase. A similar $\Delta\phi$ is needed to reach $\theta_{pq,balance}$; beyond this value, we see the sound pressure level decreasing again consistently with the pressure fluctuation drop observed during the first limit cycle.

### 3.2.3 Acoustically Decoupled Combustion Analysis

**Acoustic Decoupling:**

In order to examine in more detail the onsets of unstable modes and explore any potential causality between flame shape transition and onset of instabilities, we artificially decouple heat release fluctuations from the acoustic field. The method used for decoupling is the modification of the combustor's geometry downstream to alter the resonant frequencies without changing the underlying flow. By doing so, we break the feedback loop between unsteady heat release and acoustic pressure fluctuations. The eigen-frequencies of a combustor depend to a large extent on the geometry and the temperature distribution as these are the main sources of acoustic impedance change. Here, the combustor is shortened to achieve the decoupling of heat release and pressure in a range of equivalence ratio of interest. Figure 2-1 shows the geometry after changing the combustor's length. These two lengths lead to combustors with different sets of resonant frequencies.

The length of the combustor in both cases is larger than the largest diameter allowing for a one-dimensional modeling of the geometry. By taking into account a simple impedance change due to the presence of the flame, the resonant frequencies are estimated for both configurations. This simplified quasi-one-dimensional model assumes the flame as compact and doesn't take into account the flame transfer function. The flame, in this model, is only responsible for a sudden change in the flow temperature.

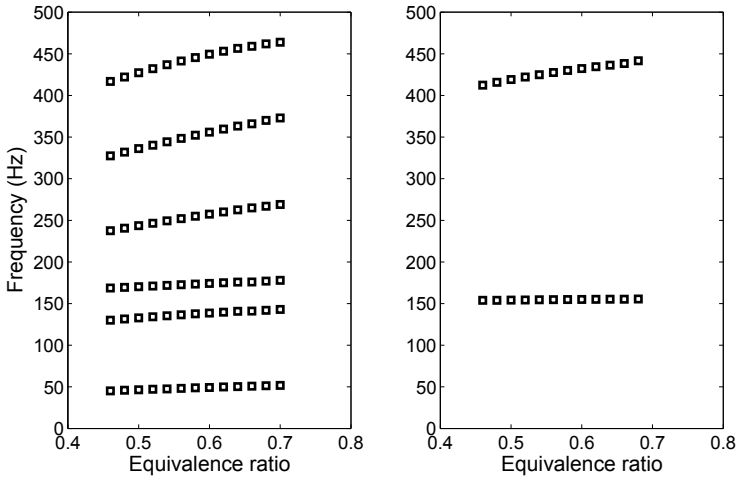


Figure 3-3: Predicted longitudinal modes of the combustor (left: long, right: short) using one-dimensional acoustic calculation.

Figure-3-3 shows the numerically predicted resonant frequencies of the initial length combustor as a function of the equivalence ratio (left) and these frequencies when the combustor is shortened by a factor of $\sim$10 (right). At $\phi = 0.61$ (onset of instability in region 3 shown previously) the first eigen-mode is estimated around 49 Hz which is in fair agreement to the frequency observed experimentally (40 Hz - see spectrogram in Fig.3-1). At $\phi = 0.68$ where region-5 instability starts, the second eigen-mode is estimated around 142 Hz to be compared to the frequency observed experimentally (117 Hz). After altering the length of the combustor, the two resonant modes mentioned above are shifted to higher frequencies and appear around 155 Hz and 440 Hz respectively. The comparison of the predicted and experimental resonant frequencies shows a fair agreement for the long combustor. A non-negligible discrepancy appears for the case of the short combustor, as will be seen later. This shows the limit of a simple one-dimensional modeling for this case where the assumptions made, like a compact flame, a large aspect ratio of the combustor, become more debatable.

Pressure fluctuations in the non-reacting flow and a near blowout (flame I) conditions are shown for the long and short comparison to further assess the above predic-

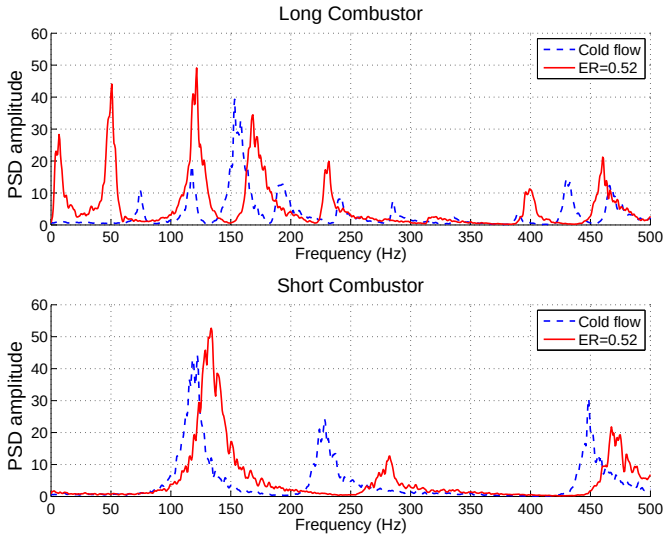


Figure 3-4: Experimental measurements of the combustors' natural frequencies, to be compared with predicted frequencies in Fig.3-3

tions. Fig.3-4 confirms the fair agreement found with predictions using the simplified acoustic network approach. We see that the natural frequency of the combustor are shifted to higher values, as expected with a shorter length. Additional peaks are observed in figure 6; these are potentially the results of non-linear interaction between acoustic modes and a precessing vortex core (PVC) [65] observed in cold flow and in flame configuration I. The PVC frequency is observed in the range 100-120 Hz, which is close to the second harmonic of the long combustor and the fundamental frequency of the short combustor. We also note the effect of the combustion and its heat release on the natural frequencies of the combustor especially for low frequency values. In the long combustor the fundamental frequency shifted from 70 Hz to around 50 Hz, for the non-reacting flow and the reacting flow at $\phi$=0.52, respectively.

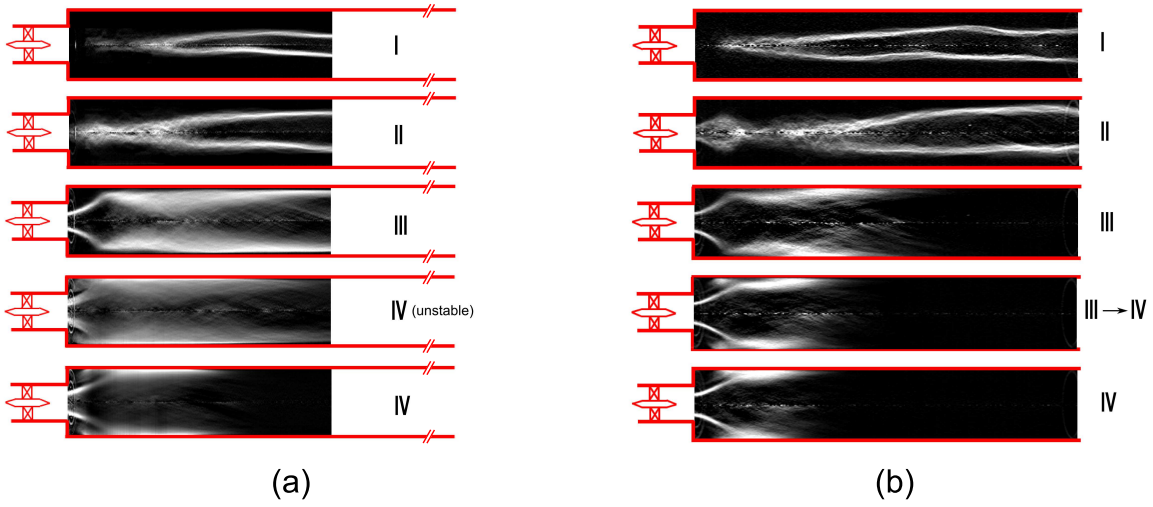


Figure 3-5: Abel-transformed flame macrostructures as $\phi$ is raised from the lean blowoff limit in the long (a) and short combustor (b). From top to bottom: $\phi$ : 0.51, 0.54, 0.57, 0.62, 0.66.

**Dynamic Stability and Flame Macrostructures in the Long vs. Short Combustor:**

We conduct the same series of experiments to determine the stability map of methane combustion in the modified combustor. A special care was given to ensure the same experimental protocol for both combustors to provide in particular similar thermal boundary conditions. We first see that the 40 Hz unstable mode is fully suppressed in the short combustor. We see also that combustion in the two previous quasi-stable regions are now fully stable. The short combustor still exhibits an unstable mode for equivalence ratio above $\phi \sim 0.7 - 0.71$ but with lower amplitude. The modification of the geometry succeeded in completely decoupling combustion from the acoustic field for equivalence ratio between the LBO up to $\phi \sim 0.7 - 0.71$.

When decoupling the acoustics from the heat release fluctuations, the swirling reacting flow in the short combustor still exhibits several flame macrostructures as we raise the equivalence ratio. As done previously, the mean flame distribution is inferred from long exposure flame imaging. Figure 3-5 (b) shows the different mean flame con-

figurations observed as the equivalence ratio is raised. The five configurations observed earlier are still observed. However, while the transition III to IV was previously accompanied by the onset of an unstable mode at the fundamental frequency of the long combustor, the transition occurs while the combustor remains stable, in the shortened version. This transition occurs gradually starting from $\phi \sim 0.61$. The flame starts to appear intermittently in the outer recirculation zone. Figure 3-6 shows a sequence of high speed flame images taken at a frame rate of 200 fps with an exposure time of 1/200 second, illustrating this intermittency and in which we see a flame appearing in the ORZ, disappearing and re-appearing again. This phenomenon is referred to as "ORZ flame flickering". ORZ flickering extends over a range $\Delta\phi \approx 0.03$ beyond which the flame becomes present in the ORZ with a probability close to 1 (as will be seen in section 3.4 which corresponds to configuration IV.

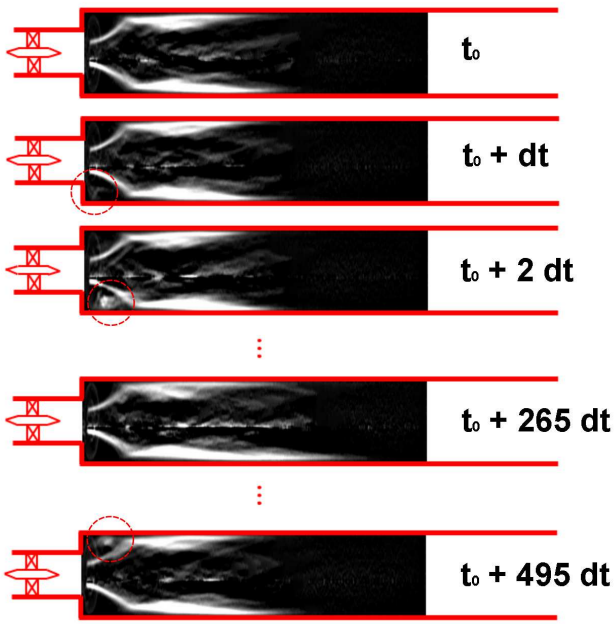


Figure 3-6: Sequence of high speed flame chemiluminescence images (200 fps, exposure time 1/200 s) showing intermittent appearance of flame in the ORZ in the short combustor. Here **dt** is the time step between two images, $\phi = 0.62$ (Combustion chamber outline shows extend of quartz tube to scale). Dotted circle shows flame in the ORZ.

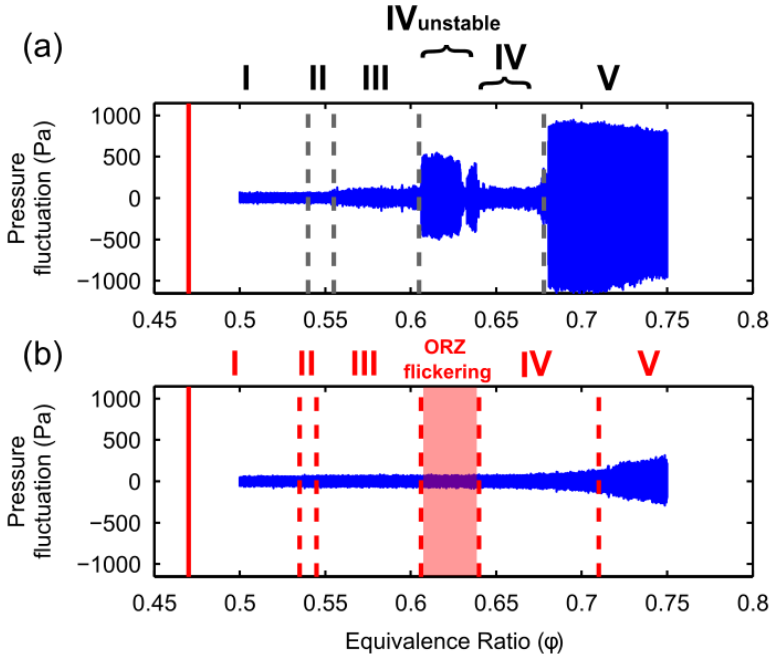


Figure 3-7: Correspondence between flame macrostructures and thermo-acoustic mode transitions for long (a) and short combustors (b) at 100% $CH_4$. The vertical solid line represents the LBO limit and dotted lines represent the transitions between macrostructures. Shaded zone in (b) shows extend of ORZ flame flickering.

| *LONG COMBUSTOR* | | | | *SHORT COMBUSTOR* | | | |
|---|---|---|---|---|---|---|---|
| $\phi$ | Freq(Hz) | Stability | Flame | Flame | Stability | Freq(Hz) | $\phi$ |
| 0.50-0.54 | broadb. | S | I | I | S | broadb. | 0.50-0.535 |
| 0.54-0.555 | broadb. | S | II | II | S | broadb. | 0.535-0.545 |
| 0.555 - 0.61 | 38-40 | QS | III | III | S | broadb. | 0.545-0.61 |
| 0.61-0.64 | 40-42 | $1^{st}$ U | IV | III-IV | S | broadb. | 0.61-0.65 |
| 0.64-0.67 | 48-55 | QS | IV | IV | S | broadb. | 0.65-0.71 |
| 0.67-0.75 | 117-129 | $2^{nd}$ U | V | V | $1^{st}$ U | 120-132 | 0.71-0.75 |

Table 3.2: Combustion dynamics and mean flame configurations in the long vs. short combustor. broadb. stands for broadband, S for stable, QS for quasi-stable and U for unstable.

Following the same approach as that used for the long combustor, we superpose the measured pressure signal - as the equivalence ratio is raised - and the different flame configurations observed. The result is shown in Fig.3-7 where transition points are carefully noted and ensemble-averaged over three experiments, performed following the same experimental protocol. We see that the observed sequence of mean flame configurations is not only the same in the long and short combustors, but the transitions (for configurations I, II, III and IV) occur at similar equivalence ratios as well. However, The transition from configuration IV to V occurs at a higher equivalence ratio compared to the long combustor case. Moreover, the ORZ flame flickering window between $\phi \sim 0.61$ and $\phi \sim 0.64/0.65$, overlaps with the range of equivalence ratio at which the long combustor exhibits its first unstable mode. Table 3.2.3 summarizes the combustion characteristics for both combustor lengths.

**Flow Field of Stable Flame Macrostructures:**

We now interrogate the flow field, in the decoupled short combustor, for each of the flame macrostructures (I to IV) using PIV. Under these conditions, these configurations are all dynamically stable. The velocity field undergoes dramatic changes as we

transition from a configuration to another, highlighting the strong coupling between the turbulent flow and the heat release. The left and right columns in Fig.3-8 show the time-averaged axial-radial velocity streamlines colored by the velocity magnitude and the total rms velocity, respectively. In addition, the zero axial velocity contour is shown , as an approximate location of the mean shear layer. Only, axial and radial velocities were measured using PIV so the mean velocity magnitude is estimated as:

$$V_{mag,mean} = \sqrt{[U^2_{x,mean} + U^2_{r,mean} + U^2_{\theta,mean}]} \tag{3.1}$$

$$\approx \sqrt{[U^2_{x,mean} + U^2_{r,mean} + (S\ \ U_{x,mean})^2]} \tag{3.2}$$

with S being the swirl number and $S\ U_{x,mean}$ an approximation of $U_{\theta,mean}$. The total root mean square velocity is calculated as:

$$V_{rms} = \sqrt{\frac{1}{3}[U^2_{x,rms} + U^2_{r,rms} + U^2_{\theta,rms}]} \tag{3.3}$$

$$\approx \sqrt{\frac{1}{3}[U^2_{x,rms} + U^2_{r,rms} + (\frac{U_{x,rms} + U_{r,rms}}{2})^2]} \tag{3.4}$$

We note that the equivalence ratios are only slightly different here compared to equivalence ratios of the mean flame images shown in Fig. 3-5 and these still correspond to the same configurations. The flow field at all equivalence ratios exhibits negative axial velocity region, namely the recirculation zones (IRZ and ORZ). These regions are bounded by the inner and outer shear layers. However, the flow strength, the presence and location of stagnation points as well as the relative size of recirculation zones are among the major differences between different flame macrostructures.

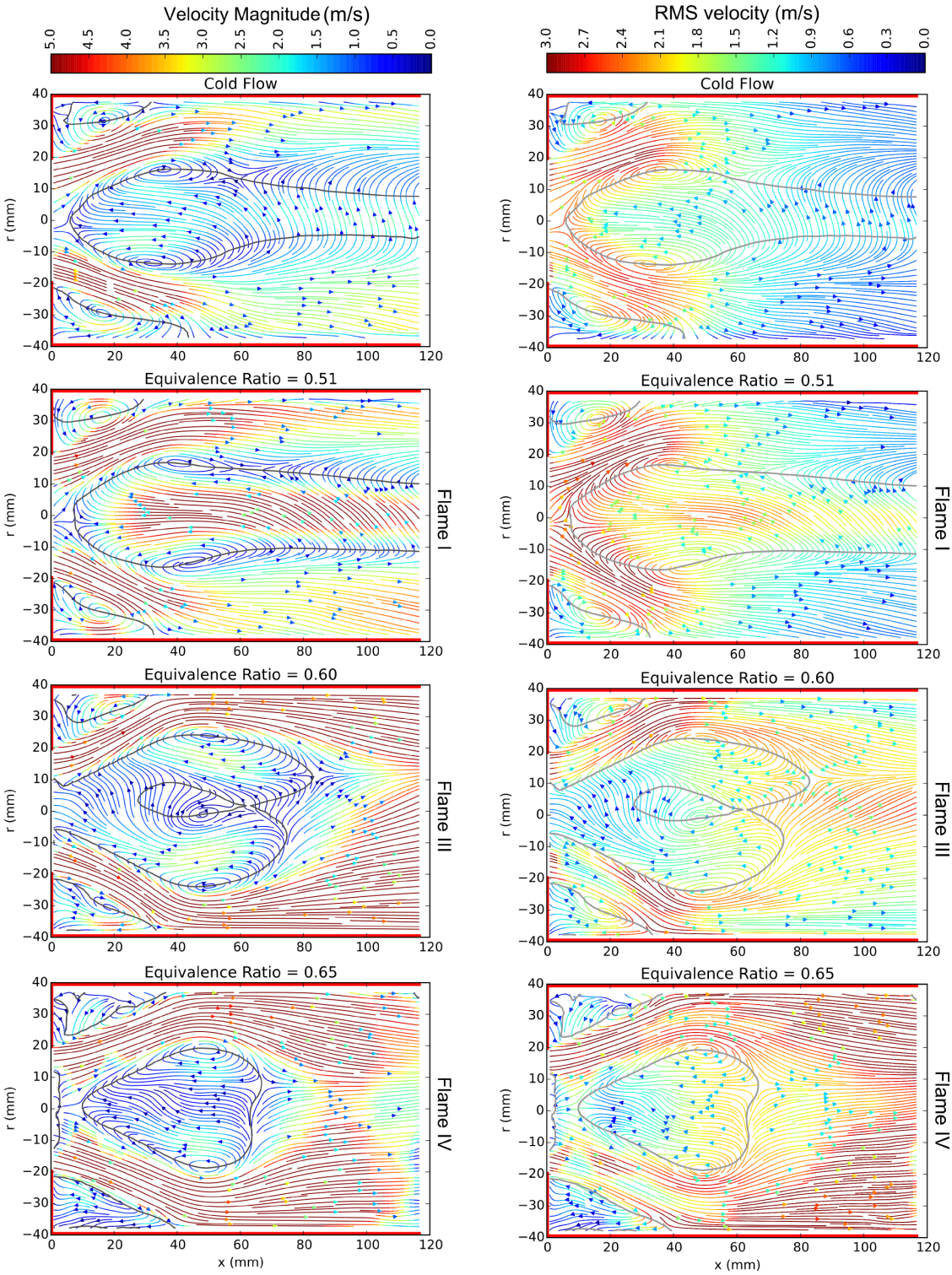


Figure 3-8: Mean velocity streamlines for non-reacting flow and flame macrostructures I ($\phi = 0.51$), III ($\phi = 0.60$) and IV ($\phi = 0.65$) colored by velocity magnitude (left column) and by total rms velocity (right column).

**Non-reacting flow:** The cold flow field shows the existence of a stagnation point around the sudden expansion plane close to the centerline. The inner recirculation zone extends downstream away from the field of view with a weak negative axial velocity. This field of view does not allow to conclude on whether this recirculation zone closes downstream or not. Two counter rotating vortices are observed on the shear layer one inlet diameter downstream of the stagnation point, contributing in average to the flow in and out of the recirculation zone. These two vortices in the plane are likely to be part of the same torroidal vortex ring. Moreover, a flow-flow impingement point is observed just downstream of the upper vortex along the inner shear layer. This point appears like an off-centered downstream stagnation point, further highlighting the cylindrical asymmetry of the flow at these conditions. This flow is similar to swirling flows with asymmetric helical mode of vortex breakdown reported in the literature for swirling flows[60, 99]. In fact, this flow exhibit a strong precessing vortex core (PVC) oscillating at a frequency around $f_{PVC}$=105 Hz or a Strouhal number $St_{PVC} = \frac{f_{PVC}\ D_{in}}{U_{in}} \approx 0.5$.

**Flame I:** The mean flow field in flame I ($\phi$=0.51) is similar to the cold flow. In the range of equivalence ratio where macrostructure I exists, which is very close to the lean blowoff limit ($\phi_{LBO} \approx 0.47$), the rate of heat release is relatively low and the effect of combustion on the flow dynamics is relatively weak. The major difference is the strength of the back flow as well the incoming jet reattachment length. The precessing vortex core is still observed for this flame with a slight shift upward in frequency.

**Flame III:** When flame III is established, the flow field is dramatically different from the non-reacting and flame I flow fields. A clearly defined inner recirculation zone bubble appears. While the upstream stagnation points disappears from the field of view, the downstream one's position becomes close to the combustor's centerline. An additional vortical structure appears in the middle of the inner recirculation zone,

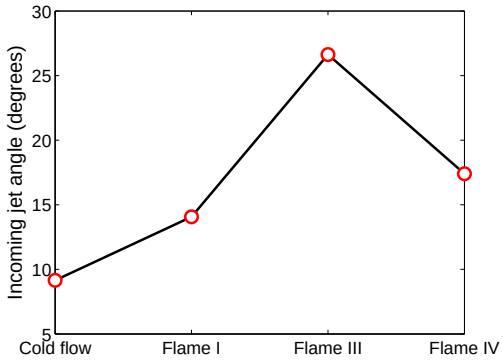


Figure 3-9: Comparison of incoming jet angle (defined using the combined axial-radial maximum velocity magnitude) for non-reacting flow and flame macrostructures I ($\phi = 0.51$), III ($\phi = 0.60$) and IV ($\phi = 0.65$).

in addition to the two vortices on the inner shear layer. The vortical structures of the inner recirculation zone lead to a two-lobe structure as shown by the axial zero velocity contour. These flame and flow field are characterized by their symmetry when compared to previous cases (cold flow and flame I).

**Flame IV:** The streamlines for $\phi$=0.65 show the mean velocity after the transition of the flame to the ORZ. A comparison with the flow field at $\phi$=0.6 shows a more compact inner recirculation zone without the two-lobe structure mentioned above. In addition, a larger incoming annular jet is observed along with the reappearance of the upstream stagnation point.

Increasing heat release level through the increase in equivalence ratio changes the flame macro-scale structure along with the flow field. The swirling flow field seems to shift from a spiral asymmetric mode dominated by a PVC with a clearly defined frequency — the PVC being observed in cold flow and flame I — to an axisymmetric vortex breakdown with a bubble-shaped inner recirculation zone, observed for higher order flames. The types of vortex breakdown observed in our experiments and their

characteristics extracted from PIV fit very well the description of the different types of vortex breakdown reported by lucca-negro et al. [60]. The suppression of the PVC has also been previously observed but there is still a lack of consensus around the mechanisms underlying it. As the equivalence ratio is raised, the heat release increases and induces a higher incoming jet velocity. Heat release only affects the meridional (axial-radial) velocity but not the swirling component. Thus, one expects the swirl strength to decrease. This could not be confirmed here as the azimuthal component of velocity was not measured. This decrease in swirl strength could potentially be the reason behind the shift from a strong asymmetric helical mode to the symmetric bubble mode of vortex breakdown instability, but this requires further investigation which outside the scope of the current study. Finally, the angle between the centerline and the mean incoming jet angle and its dependency on the equivalence ratio is plotted in Fig.3-9. The incoming jet angle and its reattachment length's corollary change as a function of equivalence ratio. The net effect of ORZ expansion and increased compactness of the IRZ lead to a larger width incoming jet. The jet forms a narrower angle in the mean flow sense for the cold flow and, as the equivalence ratio increases, the angle increases and recirculation zone becomes more compact due to higher heat release and hotter inner recirculation zone. This effect has been previously numerically studied [105]. This trend is reversed for flame IV. This can be explained by the appearance of expanded hot products in the ORZ forcing the incoming jet inward towards the combustor's centerline.

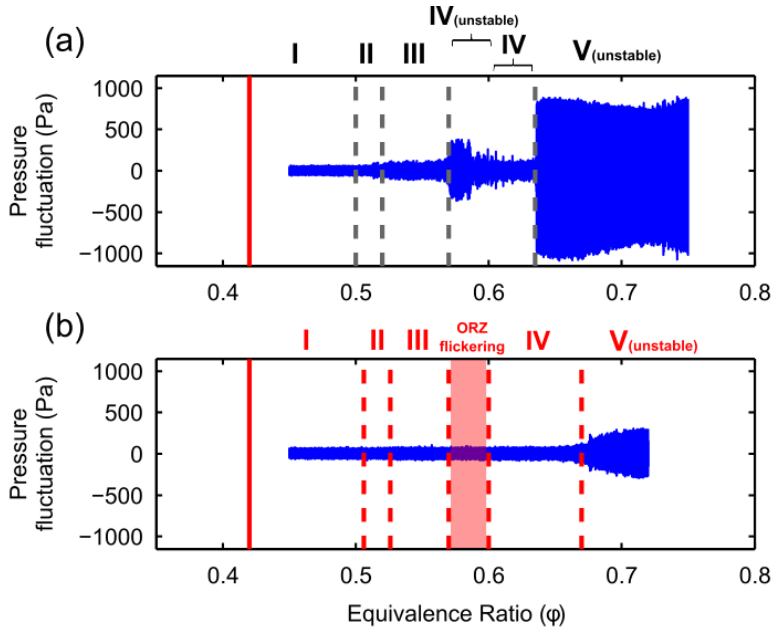


Figure 3-10: Correspondence between flame macrostructures and thermo-acoustic mode transitions for long (a) and short combustors (b) at 10% $H_2$. The vertical solid line represents the LBO limit and dotted lines represent the transitions between macrostructures. Shaded zone in (b) shows extend of ORZ flame flickering.

### 3.2.4 Effect of Fuel Composition

#### Effect of Hydrogen Addition

We conduct the same series of experiments for methane with 10% and 20% $H_2$ (by volume) to determine the stability maps using both the long and short combustors. Pressure fluctuations as a function of the equivalence ratio for the two fuel compositions are plotted in fig. 3-10 and Fig.3-11 in the same way as Fig.3-7). As expected [82, 98], we observe that leaner combustion is possible with the addition of hydrogen, as shown by the vertical solid line: LBO at $\phi$=0.42 and $\phi$=0.37 for methane with 10% and 20% $H_2$ (by volume) respectively. However, there is no fundamental difference between the stability maps of the three examined mixtures (0%, 10% and 20% $H_2$). Indeed, the same dynamic regions presented earlier can be observed again and each region has the same spectral characteristics as those observed for pure methane (spectrograms not

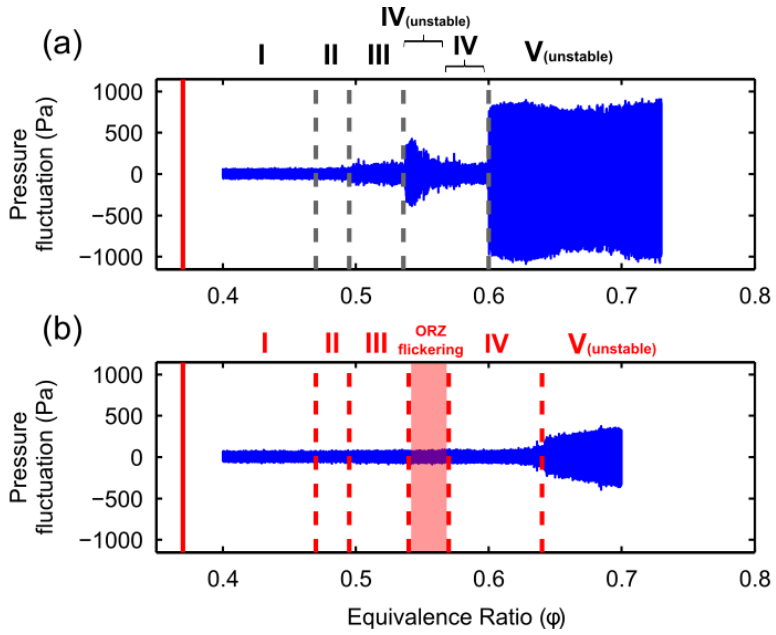


Figure 3-11: Correspondence between flame macrostructures and thermo-acoustic mode transitions for long (a) and short combustors (b) at 20% $H_2$. The vertical solid line represents the LBO limit and dotted lines represent the transitions between macrostructures. Shaded zone in (b) shows extend of ORZ flame flickering.

shown here). The main change is a shift, a broadening or narrowing of the different regions. In particular, $H_2$ addition widened the stable window in the equivalence ratio space. The same sequence of flame macrostructures is also observed for all the mixtures. The correspondence between the dynamic mode transitions and changes in the flame macrostructure also exist for 10% and 20% $H_2$. We also still observe that the onset of low frequency instability is associated with an ORZ flame flickering. We find that for a range of equivalence ratios, shown in Fig.3-10-(b) and Fig.3-11-(b), the flame appears again intermittently in the ORZ and is advected by the flow in this region leading to a circular motion at the same frequency previously extracted for methane i.e. 28 Hz.

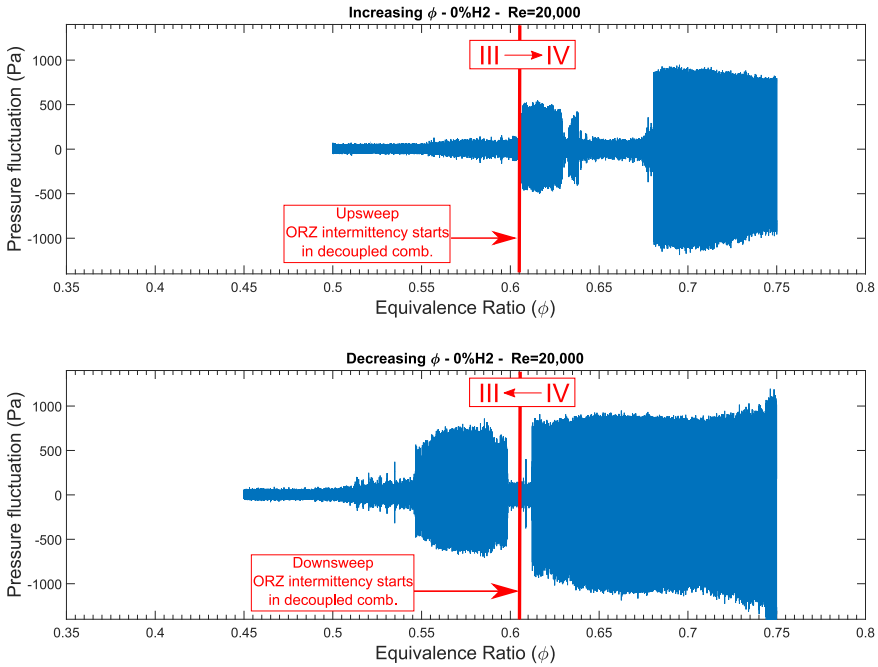


Figure 3-12: Stability maps of pure methane combustion for increasing and decreasing equivalence ratio. The vertical lines mark the onset of ORZ flame intermittency in the acoustically decoupled case.

## 3.3 Non-linear Dynamics Interpretation

The stability maps constructed in the analysis so far were obtained using the equivalence ratio as a parameter while increasing its value starting from the lean blowoff limit. Similar experiments were performed while lowering the equivalence ratio. The pressure signals for increasing and decreasing parameter are shown in Fig.3-12 for 100% methane. A hysteresis is observed for both limit cycles (LC-1 and LC-2). The existence of a sudden transition to limit-cycle oscillations along with the hysteresis suggest that the bifurcations taking place in the acoustically coupled system are of subcritical Hopf type. This type of bifurcations — that causes a sudden transition from steady state to self-excited limit cycle oscillations in the configuration we are investigating in this thesis — is not surprising. Indeed, multiple studies have previously highlighted the existence of subcritical Hopf bifurcations in simple thermoacoustic systems [62] but

also in realistic configurations [48, 56]; According to Kabiraj and Sujith [43], "it is well established that in thermoacoustic systems, transition to instability occurs through a Hopf bifurcation, often through a subcritical Hopf bifurcation.".

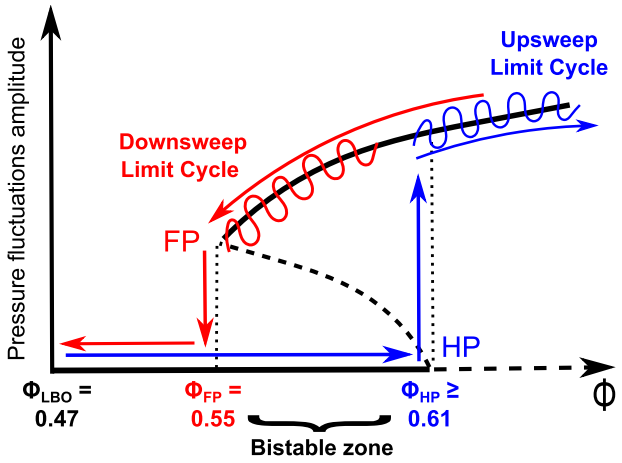


Figure 3-13: Schematic of a subcritical hopf bifurcation with Fold and Hopf points (FP and HP) extracted from the experimental stability maps of methane combustion in the acoustically coupled combustor.

A schematic bifurcation diagram for a subcritical Hopf bifurcation is shown in Fig.3-13. It is characterized by a Fold Point (FP) which is the boundary point between limit cycle and stable operations as the parameter is lowered, and a Hopf Point (HP) above which the limit cycle oscillations are the only possible state of the system (the zero pressure fluctuations fixed point is no longer stable in the non-linear sense) and an infinitesimal pressure disturbance from the zero pressure fluctuations fixed point leads to a transition to the limit cycle. The experimental stability maps in Fig.3-12 can also be seen as a bifurcation diagram with the equivalence ratio as a parameter; from these, it can be inferred that the fold point FP (for LC-1) is equal to $\phi_{FP}$=0.55. In a subcritical Hopf bifurcation, the interval between FP and HP is the bi-stable zone also called the "triggering zone" where triggering of the limit cycle is possible if the system is subject to a large enough perturbation. From the experimental stability map, it can be inferred that the Hopf point's equivalence ratio $\phi_{HP}$ has to be larger or equal to

0.61 when the onset of the first thermo-acoustic instability is observed experimentally. Based on the above discussion, a possible interpretation of the link between the onset of instability and the appearance of the flame in the ORZ is the following: the conditions of existence of flame III (Flame with no combustion taking place in the ORZ and no flame stabilized along the OSL) may match the conditions where the system is bi-stable. If the system is subject to a "large enough" pressure perturbation (due for instance to a heat release rate perturbation by an intermittent creation and destruction of flame surface) is applied to the system, the bifurcation to a limit cycle oscillation may take place. The intermittent appearance and disappearance of the ORZ flame can potentially provide this perturbation. We will see in **chapter**-4, that this flame transition is indeed associated with a highly unsteady heat release rate which provides evidence toward the above hypothesis. An additional piece of evidence that support the hypothesis that the intermittent flame in the ORZ can trigger the onset of instability lies in the comparison of the stability maps with changes in flame macrostructure as the equivalence ration is reduced (downsweep). The downsweep intermittency of the flame in the ORZ is observed to take place in the acoustically decoupled system at $\phi_{IV\ to\ III} = 0.605$ (ensemble average over three realizations). Meanwhile, the onset of the 40 Hz limit cycle oscillations occurs at $\phi = 0.60$, as shown in Fig.3-12. Similar results obtained for methane with 10% $H_2$ (Fig.3-14) and 20% $H_2$ (Fig.3-15) confirm the above observation.

## 3.4 Flame Transition to the ORZ : a First Analysis

The previous analysis established a relationship between the different dynamic modes and the mean flame macrostructures observed. We saw that even when decoupling the reacting flow from the acoustic field, the flame brush spatial distribution still changes

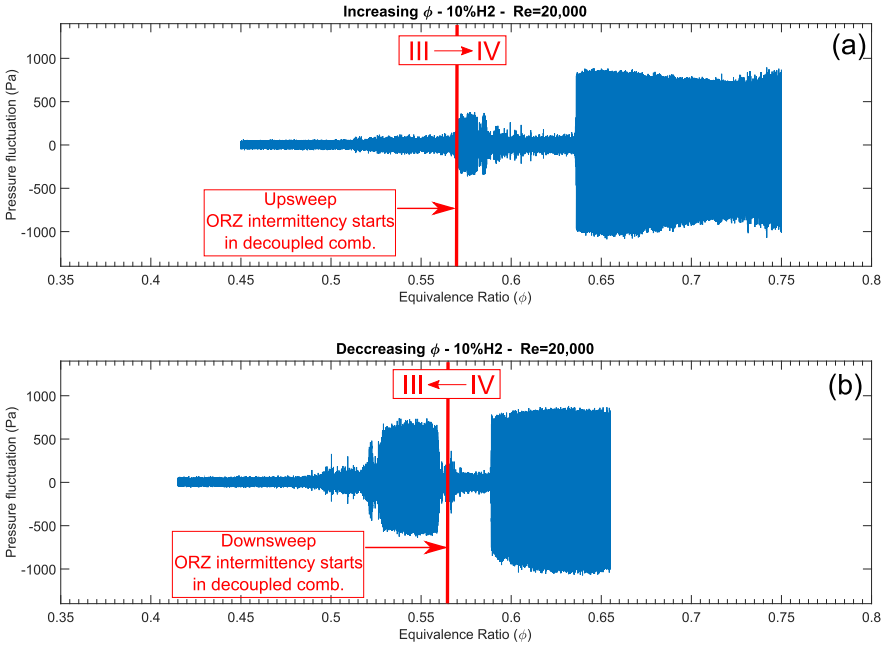


Figure 3-14: Stability maps of methane combustion with 10% $H_2$ for increasing and decreasing equivalence ratio. The vertical lines mark the onset of ORZ flame intermittency in the acoustically decoupled case.

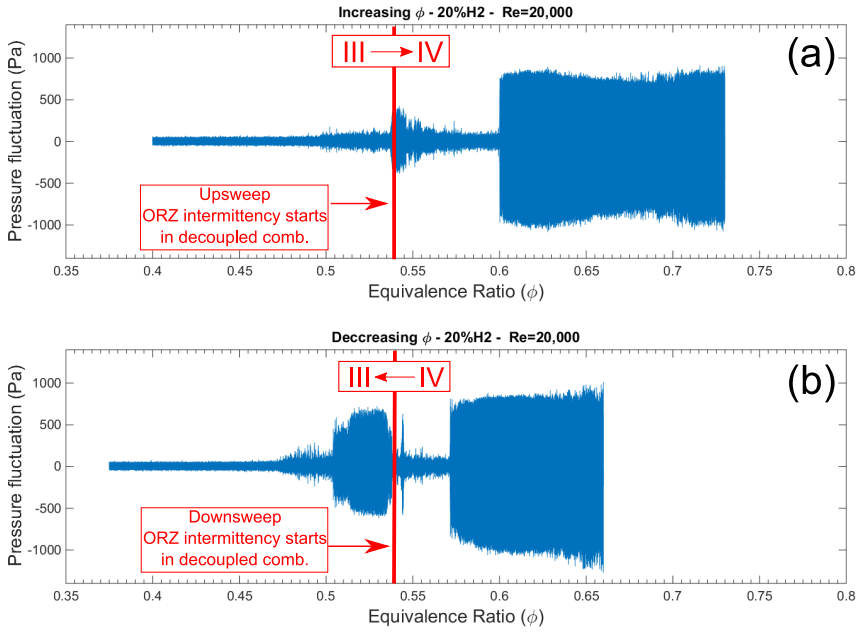


Figure 3-15: Stability maps of methane combustion with 20% $H_2$ for increasing and decreasing equivalence ratio. The vertical lines mark the onset of ORZ flame intermittency in the acoustically decoupled case.

and transitions occur around the same equivalence ratio. The onset of instability at the fundamental frequency of the long combustor is of particular interest as it is associated with a specific event: the change in flame configuration from flame III to IV through an intermittent appearance of the flame in the outside recirculation zone (see Fig.3-16) as highlighted earlier. In this section, we aim to explore this transition in more detail.

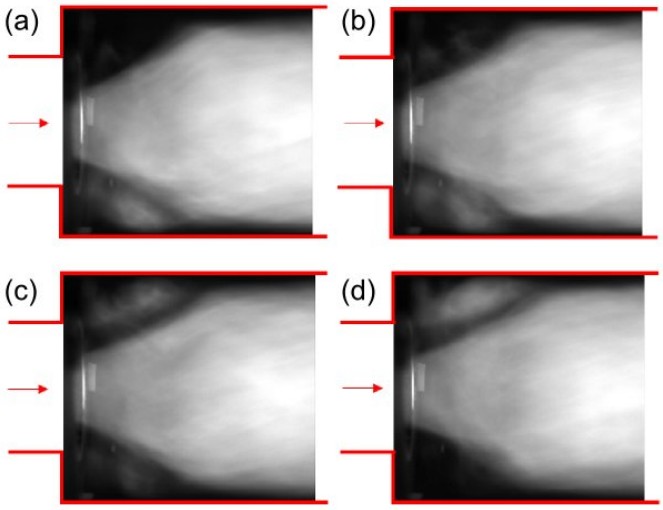


Figure 3-16: Consecutive non-Abel-deconvolved flame chemiluminescence images at 200 Hz. Time between images: 5 ms. Equivalence ratio $\phi$=0.62.

Using the shortened version of the combustor, we increase the equivalence ratio - following again the same procedure. When reaching the flickering interval, the equivalence ratio is maintained and infrared-filtered high speed images are recorded at a frame rate of 200 frames per second, an exposure time of 5 milliseconds, from $\phi$=0.59 to $\phi$=0.66 i.e. a wider range encompassing the transition between flame III and flame IV. This enables us to follow the flame dynamics and extract potential spectral information. Figure 3-16 shows a consecutive sequence of high-speed camera images. These line of sight images show the appearance of a flame pocket in the outside recirculation zone. We also observe a circular motion of the ORZ flame around the centerline, which will be confirmed below. Flame chemiluminescence intensity is extracted from

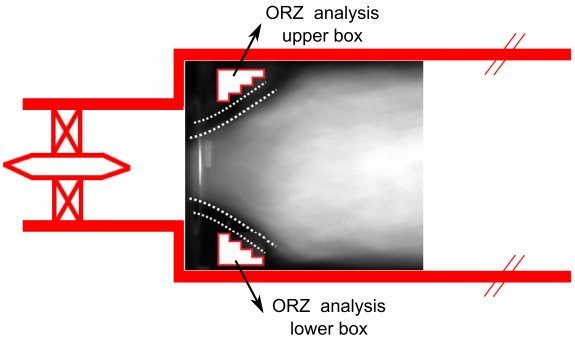


Figure 3-17: Schematic of the ORZ flame analysis regions (dotted lines show schematically the locations of the incoming swirling jet and shears layers).

a selected region in the ORZ, displayed in Fig. 3-17, and spatially averaged over that region. The probability of a flame to be present in the ORZ is computed and plotted in this range of equivalence ratio (see Fig.4-6). The probability is calculated using the flame CH*-chemiluminescence images as follows:

$$P_{ORZ}(\phi) = \frac{\left\{ \#Frames(\phi) \;\middle|\; \frac{[CH*]_{ORZ}(\phi)}{max([CH*]_{ORZ}(\phi{=}0.63))} \geqslant 1\% \right\}}{\{\#Frames(\phi)\}}$$

As the equivalence ratio is raised the probability of having a flame in the outside recirculation zone increases, with an inflection point at $\phi$=0.63. For $\phi \leq 0.65$, the flame becomes continuously present in the ORZ as reflected by its probability $P_{\phi=0.65}$=0.97.

The ORZ space-averaged flame intensity is now plotted over time in Fig.3-19 for $\phi$=0.60, $\phi$=0.63, $\phi$=0.66 along with its discrete Fourier transform using the FFT algorithm. The spectral analysis shows the presence of low frequency events in the range $\sim$[5 Hz - 10 Hz] and a clear tone occurring around 28 Hz.

From the temporal variation of the signal, we see that the low frequency events correspond to the re-appearance of the flame in the ORZ. In some of these appearance instances, the flame reaching the ORZ is quickly extinguished. In other instances, the flame remains in the ORZ and appear to be rotating in that zone around the combustor centerline. To demonstrate this flame rotation along the ORZ, we analyze the intensity

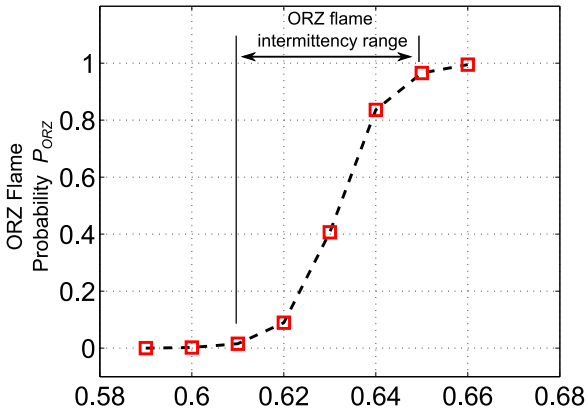


Figure 3-18: Probability of flame presence in the ORZ calculated from chemiluminescence images as the numbers of frames where the flame is in the ORZ over the total number of frames.

signal obtained from high-speed chemiluminescence in the regions highlighted in fig. 3-17. The flame intensity signals from the two regions are overlaid in fig. 3-20 over a shorter time window, showing the in-phase character of the low frequency and the out-of-phase nature of the high frequency. In this time window, the low frequency component of the signal correspond to the appearance of the flame in the ORZ at times 3s and 3.2s, whereas the 28 Hz component appears clearly between 3.3 and 3.4s.

The phase difference between the two signals is extracted by, first, analyzing their coherence then by extracting the phase of their cross-power spectral density. Figure 3-21-(c) shows maximum coherence for f=28 Hz. At this frequency, the phase delay is approximately equal to $(-\pi)$, as shown in fig. 3-21-(d). This result confirms quantitatively the observation made earlier: the flame appears intermittently at one location of the ORZ and is advected azimuthally by the flow in a circular motion around the combustor centerline.

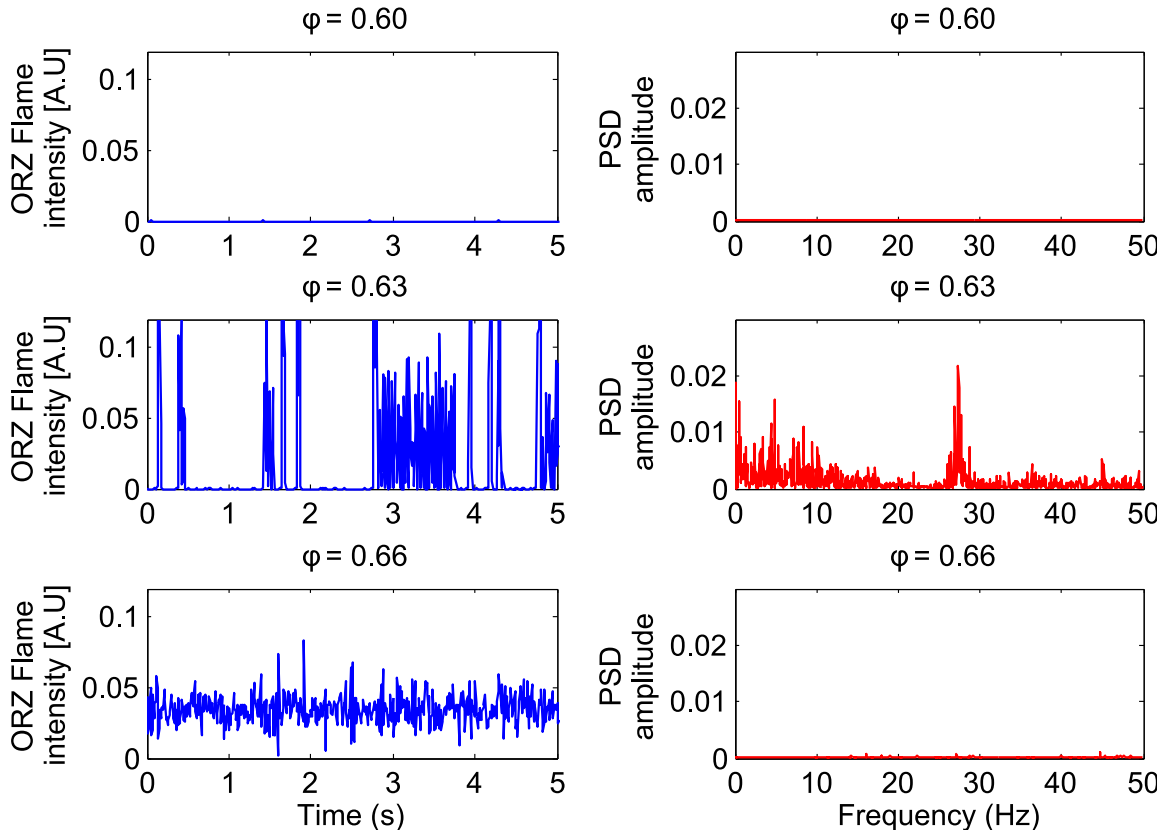


Figure 3-19: ORZ flame spectral analysis for $\phi$=0.60 (flame III), $\phi$=0.63 (flame III $\leftrightarrow$ IV), $\phi$=0.66 (flame IV): normalized space-averaged IR filtered chemiluminescence intensity signal in ORZ (left) and its fast Fourier transform (right).

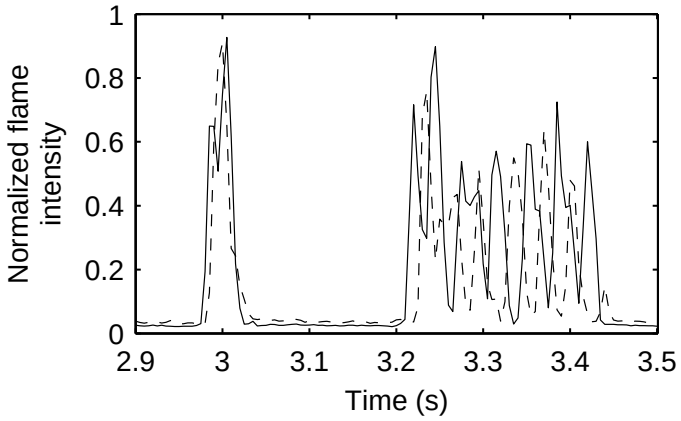


Figure 3-20: Normalized intensity in upper (solid line) and lower (dotted line) ORZ analysis regions for 100% $CH_4$ at $\phi$=0.62 between t=2.9s and t=3.5s.

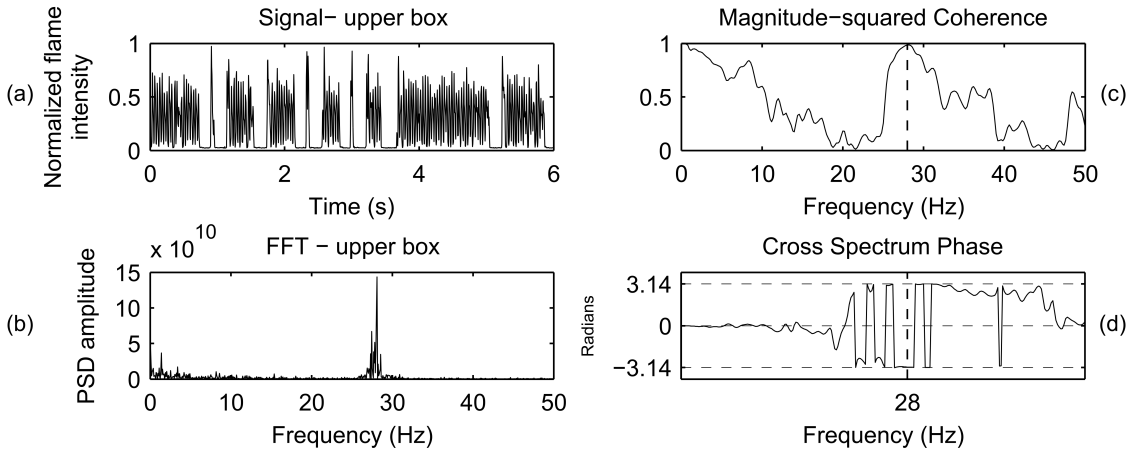


Figure 3-21: ORZ flame analysis at $\phi = 0.62$: Normalized intensity signal in upper ORZ region (a), Power Spectral Density amplitude (b), and phase analysis (c) and (d).

## 3.5 Chapter Conclusion and Next Step

In this chapter, we examined the link between the combustion thermo-acoustic modes and flame macrostructures in an atmospheric pressure premixed swirl-stabilized dump combustor under coupled and uncoupled conditions, and for different fuel mixtures. By breaking the feedback loop between the heat release rate and acoustic pressure fluctuations, through modifying the resonant frequencies of the combustor without changing the flow, the transition between different flame configurations as the equivalence ratio grows was analyzed. We conclude the following:

1. Each dynamic mode in the long acoustically coupled combustor is associated with a specific flame configuration (I to V). In a subset of these configurations - III, IV and V - transitions are accompanied by changes in the dynamic mode. The same sequence of time-average flame configurations persists in the short combustor, occurring at similar equivalence ratios as the observed transitions in the long combustor (for I, II, III and IV). In particular, the onset of the low frequency unstable mode in the long combustor matches with the transition to a configu-

ration in which the flame appears in the ORZ, in the long and short combustor.

2. Intermediate speed chemiluminescence analysis of the transition from macrostructure III to IV shows that the intermittent appearance of the flame in the ORZ is characterized by a tonal frequency band at 28 Hz along with a weaker broadband region at lower frequencies between [5-10] Hz. We show that the 28 Hz frequency corresponds to the frequency of the flame circular motion as it is azimuthally advected by the ORZ flow.

3. $H_2$ addition, up to 20%, lowers the LBO as expected but also widens the stability window in the equivalence ratio space. The addition of $H_2$ confirmed the correspondence between the uncoupled flame configurations and the different thermo-acoustic modes. ORZ flame flickering at the same frequency (28 Hz) is also observed when $H_2$ is added to the fuel mixture and linked to the onset of the low frequency unstable mode in the long combustor as well.

In the next chapter, we continue the analysis of the flame transition from III to IV. We will focus on the physical mechanism leading to the flame appearance in the ORZ, and examine it dependence on different inflow conditions (Reynolds and swirl numbers) and fuels. The goal is to propose a criterion that will allow us to predict this transition under any desired operating condition.

# Chapter 4

# ORZ Flame Transition: Mechanism, Dynamics and Scaling

## 4.1 Introduction

Among the different flame configurations observed in swirl-stabilized combustion systems, flames III (ISL stabilized flame) to IV (ISL and ORZ/OSL stabilized flame) and the transition between them are of particular interest as seen in **chapter**-3. The sharp and sudden transition to a large amplitude limit cycle concomitant with the appearance of the flame in the ORZ suggested that the latter event may act as a mechanism for a bifurcation to thermo-acoustic instability. Thus, understanding the conditions for the existence and transition of different flame macrostructures is of critical importance as it also impact the flame position and overall length of the combustion zone, which contributes to other processes such as emissions ($NO_x$) and heat losses to the wall.

### 4.1.1 ORZ/OSL Flame in the Literature

Schefer et al. [82] investigated the effect of hydrogen addition to lean premixed methane combustion on static stability of a swirling system as well as CO and $NO_x$ emissions. They concluded that the "flame characteristics were affected most significantly by reactions in the corner torroidal zone". When adding 12% of hydrogen (by volume) to the methane, the flame started appearing intermittently in the ORZ. A complete transition with a continuous flame in the ORZ occurred at a higher hydrogen level (29% by volume). It was postulated that the changes observed due to hydrogen addition are mainly the result of higher OH, H, and O radical concentrations i.e. higher reactivity. Similar to Schefer et al., our analysis in **chapter**-3 showed the ubiquity of this transition for different fuel and quantified its intermittency. We extracted the frequency associated with the ORZ flame and showed the increasing probability of finding a flame in the ORZ as the equivalence ratio is raised. In an other study looking at the effect of $H_2$ addition, Kim et al. [47] also found that the propensity of having a flame front propagating in the ORZ and along the OSL increases with hydrogen content. They conjectured qualitatively that this effect is due to the higher flame propagation speed as well as the enhanced resistance to extinction when hydrogen is added. In addition they found that different combinations of equivalence ratio and hydrogen content can lead to similar flame shapes. Another recent work, by Guiberti et al. [29] looking at the effect of hydrogen on thermo-acoustically stable combustion confirms the above findings in a more quantitative manner. Guiberti et al [29] quantified the probability of flame presence in the ORZ by extracting the OH signal from PLIF images. They found that hydrogen addition increases the probability of an M-flame (a flame stabilized along both the ISL and OSL).

In these studies, efforts focused on modifying primarily the mixture transport and thermo-chemical properties. Another way of affecting these properties is by changing

the oxidizer composition as in Shroll et al. [87, 88] in their investigation of turbulent oxy-flames for swirl-stabilized combustion. The mole fraction of $CO_2$ was modified, and it was shown that the same sequence of flame shapes is observed when compared to air combustion.

Other studies focused primarily on investigating the effect of inflow conditions and combustor geometry on different flame macrostructures and their transition points. Chtrerev et al. [13] analyzed the effect of flow conditions through changing the Reynolds (in the range 84,000 to 170,000) and swirl numbers (using axial swirlers with vane angles $\alpha_{sw}$ of 37 and 45 degrees) on the transition between flames III and IV. They emphasized the existence of hysteresis making the transition point from flame III to IV occur at higher equivalence ratio compared to the transition from flame IV to III. The extent of the hysteresis zone was shown to depend on the flow conditions. While the sensitivity to the swirl number was found to be relatively weak, a higher equivalence ratio was needed to establish a flame in the ORZ/OSL at higher swirl. It was argued that this behavior was "counter-intuitive" since increasing swirl number is commonly expected to have a flame stabilizing effect and that the swirl effect on flame stabilization are complex and requires further analysis. The effect of the Reynolds number on transitions between flame shapes is more straightforward; the relationship to the inlet Reynolds number is more intuitive based on the widespread conjecture that the higher strain rate in the outer shear layer prevents the flame from stabilizing in that location at lower equivalence ratio.

### 4.1.2 Modeling the Transition Between Flame Macrostructures

While previous studies documented experimentally the transition between flames III and IV, only few attempts have been made to scale this transition across operating conditions.

Foley et al. [19] proposed the use of the laminar extinction strain rate to collapse the transition points between all observed flame configurations across a range of preheat temperatures (366 K to 533 K) and equivalence ratios (0.40 to 0.70). The results showed that a flame transitions from a configuration to another when reaching an extinction strain rate threshold, including the ORZ flame related transition albeit a 40% variability was observed in some cases.

Guiberti et al. [30] proposed a model to explain the transition of the flame to the outer shear layer (V to M flame in their nomenclature). Based on the observation that the flame strongly interacts with the wall in their setup, they investigated the scenario originally proposed by Huang et al. [35] (using LES) in which the flame appears to flashback to the ORZ through the boundary layer. They estimated a flashback Karlovitz number that incorporates the velocity gradient across the boundary layer and a turbulent displacement speed based on the laminar flame speed corrected by the Lewis number. The latter correction originates from the turbulent flame speed correlations extensively reviewed by Lipatnikov et al. [58]. The authors show that the Karlovitz number they define captures reasonably well the trend of flashback onset into the ORZ but the transitions didn't occur at a unique Karlovitz number when flow conditions and confinement ratio were changed (in order to affect the velocity gradient at the wall). While a spatially resolved data on the flame as it propagates through the boundary layer were not shown, this investigation points out the importance of flame interaction with the wall at the conditions they explored. Different physical mechanisms responsible for the ORZ flame might exist depending on system design (mainly the expansion ratio and level of jet interaction with the wall). In our present study, with a fixed expansion ratio of 2, we highlight a different physical mechanism responsible for the flame inception in the ORZ.

### 4.1.3 Chapter Overview

The objectives of this chapter are to:

1. Elucidate the physical mechanism underlying the transition to an ORZ flame in an acoustically uncoupled combustion system.

2. Explain the way this transition and its dominant dynamics are affected by different operating conditions such as fuel composition, Reynolds and swirl numbers, and thermal boundary conditions.

3. Propose a model for scaling its onset across a wide range of conditions.

The current chapter is organized as follows. First, we present the different operating and thermal boundary conditions we explored. Next, the instantaneous flame and flow structures acquired using OH-PLIF and PIV are analyzed to characterize flame III and IV. These two flames bound the transition we are examining. Afterwards, the mechanism through which the transition takes place is investigated. We explore the dependency of the transition and major dynamics to fuel composition, Reynolds and swirl numbers as well as heat loss. Finally, we propose a single non-dimensional number that successfully capture the observed dependence.

## 4.2 Operating conditions

The experimental setup used in this chapter is the fully premixed swirl-stabilized experimental combustor we investigated in the previous chapter in its acoustically decoupled version (short combustor). The main additions compared to previous study include a circular opening centered at 10 mm downstream of the expansion plane to allow a K-type thermocouple to be placed through to interrogate the ORZ temperature and

| Re | $\alpha_{sw}$ | Fuel | $\phi$ | Insulation |
|---|---|---|---|---|
| 15,000<br>20,000<br>25,000<br>30,000 | 30.0<br>45.0<br>52.5<br>60.0 | $(1-x)$ $CH_4 + x$ $H_2$<br>x $\in$ [0%, 50%] | Spanning<br>flame III<br>and IV | Non insulated<br>Partially insulated<br>Fully insulated |
| 20,000 | 45.0 | 100% $CH_4$ | 0.56 to 0.66 | Non insulated |

Table 4.1: Operating parameter space and different thermal boundary conditions investigated (the reference case is shown in the bottom row)

the different levels of thermal insulation (see Fig.4-1). The operating and boundary conditions used in this chapter are summarized in Table 4.1. In the reference case, we operate the combustion system using pure methane with a Reynolds number Re=20,000 (defined based on the inlet bulk velocity and inlet tube diameter) and a swirler blade angle $\alpha_{sw} = 45$ arc degree with no added insulation i.e. a stainless steel side wall at the sudden expansion and the 2.5 mm thickness quartz tube.

At the reference flow conditions, we raise the equivalence ratio in the range [0.56 - 0.66] encompassing the transition between flame III and IV. The same approach is followed for all the other operating conditions. The analysis in the first part of this chapter is carried at the reference case. In the second part of the chapter, we modify the Reynolds number, the swirler blade angle, the fuel and the level of insulation around the combustor, in the range shown in Table.4.1. The effect of heat loss is explored at the reference Reynolds and swirl numbers by testing two additional thermal boundary conditions; a partially insulated case where the stainless steel wall (thermal conductivity of 17.5 $W.K^{-1}.m^{-1}$ at 100 C and 20.9 $W.K^{-1}.m^{-1}$ at 500 C) is replaced by a ceramic wall composed of 85% alumina ($Al_2O_3$) and 15% silica ($SiO_2$) (thermal conductivity of 0.16 $W.K^{-1}.m^{-1}$ at 250 C). The ceramic material density and specific

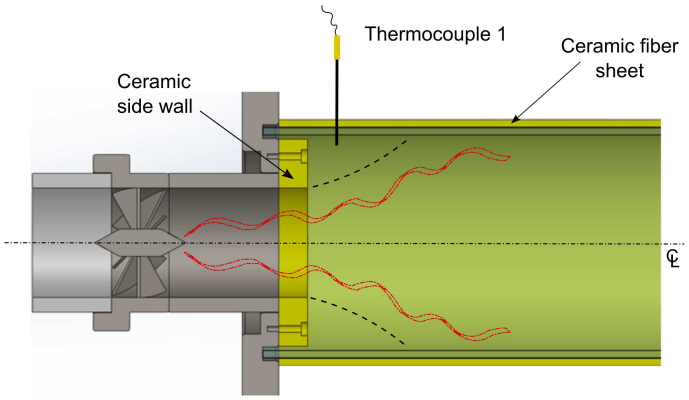


Figure 4-1: Ceramic insulation used to investigate thermal boundary condition effects, and location of the K-type thermocouple probing the ORZ temperature. The ceramic fiber sheet covers the entire Quartz tube length.

heat capacity are 750 $kg.m^{-3}$ and 1047 $J.K^{-1}.kg^{-1}$ respectively, at ambient temperature and pressure. The third thermal boundary condition case is the fully insulated one where, in addition to the ceramic side wall, a flexible ceramic fiber sheet of thickness 5-8 mm is used to cover the fused silica quartz tube (the fused silica's thermal conductivity is around 1.55 $W.K^{-1}.m^{-1}$ at 200 C). The detailed location of the ceramic pieces can be seen in Fig.4-1.

## 4.3 Inception of an ORZ/OSL flame

### 4.3.1 ISL and ORZ/OSL flames

In the previous chapter, we showed the existence of several flame macrostructures (see Fig. 1-2) as we changed the equivalence ratio or the hydrogen content of the methane fuel mixture. These flames include the conical flame (flame III) where the reaction zone is mainly located along the ISL separating the vortex breakdown bubble and the incoming swirling jet. Flame IV was shown to appear at higher equivalence ratio or at higher hydrogen content while keeping the same equivalence ratio. The latter

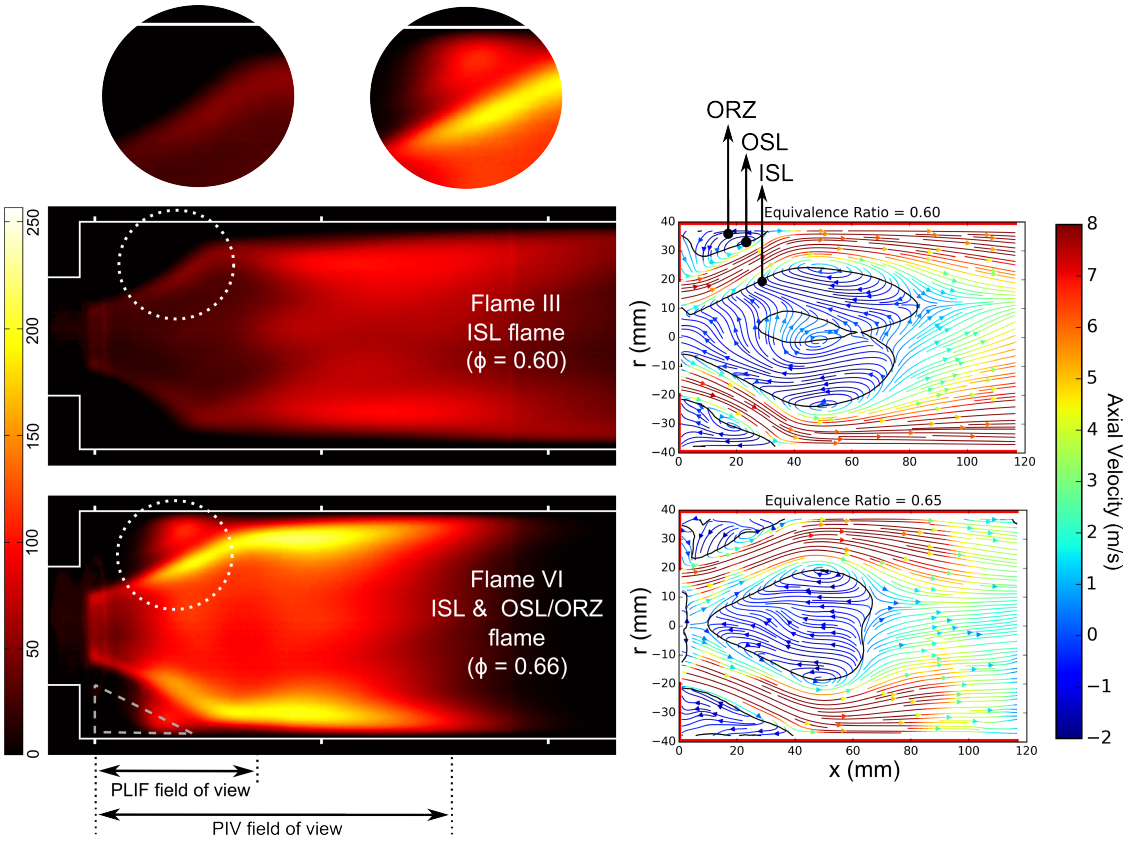


Figure 4-2: Left: IR-filtered chemiluminescence from flame III at $\phi$=0.6 and flame IV at $\phi$=0.66 at the same intensity scale: average of 1800 images taken at 100 Hz and exposure time of 4 ms taken at the reference conditions (pure methane, Re=20,000 and swirler angle of 45 deg.). The two circular images (top) show a zoom on the ORZ delimited by the dashed circle. The dashed triangle shows the ORZ analysis box. Right: Mean axial-radial velocity streamlines colored by velocity magnitude multiplied by the sign of axial velocity, for flame III at $\phi$=0.6 and flame IV at $\phi$=0.65.

flame is characterized by the presence of a reaction zone within the ORZ as well as a flame stabilized along the OSL (not necessarily extending to the sudden expansion section), besides that propagating along the ISL. These two flames — III and IV in our nomenclature — bound the transition we are focusing on in this chapter.

Line-of-sight chemiluminescence from flame III at $\phi$=0.60 and flame IV at $\phi$=0.66 is shown in Fig. 4-2 for the reference case. After the transition to flame IV, the turbulent flame becomes on average more intense due to the increased heat release at higher

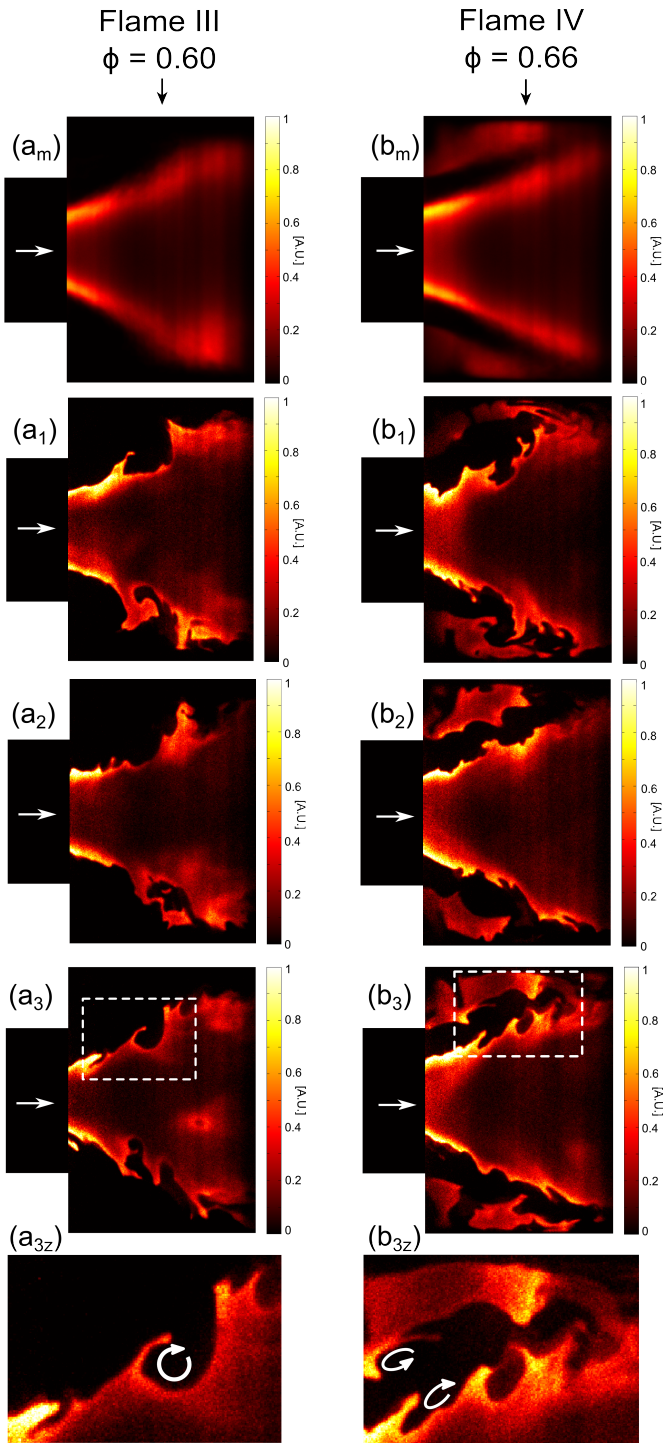


Figure 4-3: $CH_4$/air OH-PLIF of flame III at $\phi$=0.60 (column 1) and flame IV at $\phi$=0.66 (column 2):($a_m/b_m$) Mean OH-PLIF using 256 instantaneous images. (($a_1/b_1$) to ($a_3/b_3$)) representative non-consecutive OH-PLIF. (($a_{3z}/b_{3z}$)) zoom of region shown in ($a_3/b_3$). Note: the chamber's wall coincides with the edge of the images.

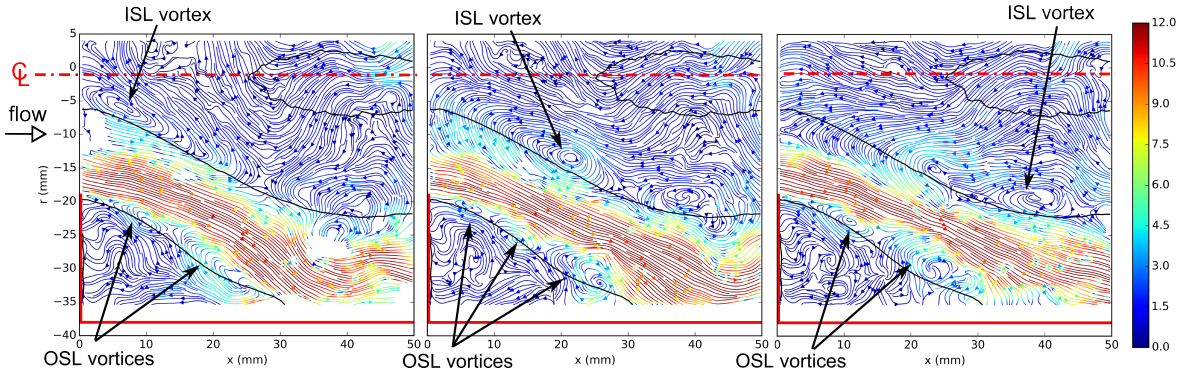


Figure 4-4: Instantaneous and consecutive (at 1000 Hz) velocity streamlines of flame III ($\phi$=0.60) exhibiting inner and outer shear layer vortical structures. Streamlines are colored by axial-radial velocity magnitude (in m/s). The solid black line corresponds to the zero mean axial velocity.

equivalence ratio. The flame becomes also more compact; a shorter flame is due to the higher burning velocity requiring lower flame surface area. It is also due to the creation of a new flame surface around the ORZ. The mean velocity streamlines in Fig. 4-2 show the location of the shear layers in the mean sense. A slight change in incoming flow angle is observed; this can be attributed to the thermal expansion of the ORZ when the flame appears there as this zone becomes recirculating combustion products instead of reactants. Moreover the interrogation of the flow field highlights the change in the IRZ structure when the transition takes place. Flame III mean flow field shows a lobe shaped IRZ that can also be noticed from the associated chemiluminescence image. This lobed structure, having a region of positive velocity along the IRZ's centerline, disappears when the flame becomes established in the ORZ. This change in structure during the transition was studied using DMD (Dynamic Mode Decomposition) and shown to take place at very low frequency (5-10 Hz) [52].

We examine now the flames microstructure. OH-PLIF images are taken with a gating time of 100 ns and the spatial resolution of these images is equal to 8.3 pixels per mm which allows us to extract the detailed instantaneous structure of the flame, or

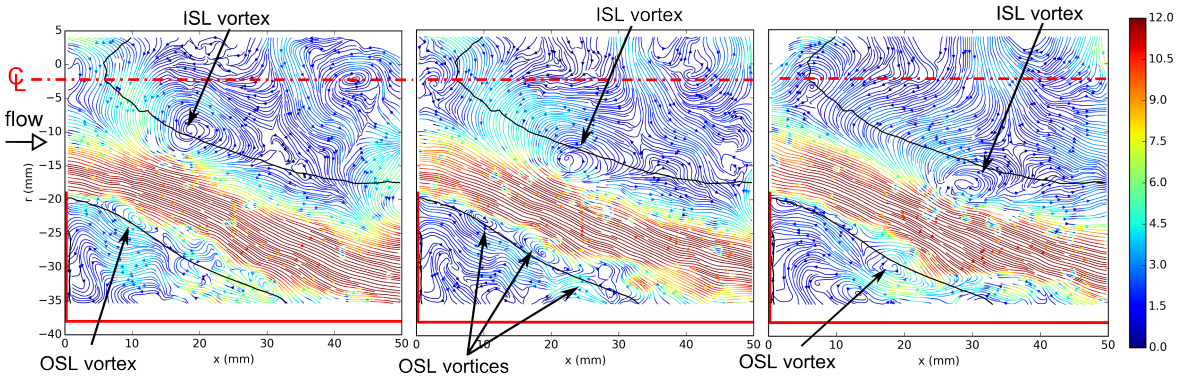


Figure 4-5: Instantaneous and consecutive (at 1000 Hz) velocity streamlines of flame IV ($\phi$=0.65) exhibiting inner and outer shear layer vortical structures. Streamlines are colored by axial-radial velocity magnitude (in m/s). The solid black line corresponds to the zero mean axial velocity.

microstructures. OH is present in both the reaction zone and in the products zone (at relatively lower levels) as it is slowly consumed in burnt gases when compared to its production rate at the flame front [28]. Representative OH-PLIF images for $\phi = 0.60$ and 0.66 are shown in Fig. 6-6 along with a zoom on shear layers and the average OH-PLIF images. At $\phi = 0.60$, we see the flame stabilized along the ISL. In addition, the flame is convoluted by what appears to be shear layer vortices rolling-up. The presence of such vortices is confirmed by the high resolution flow field PIV data, in Fig. 4-4, showing vortical structures along the ISL of similar scale as the wrinkle scale observed in the OH-PLIF data. The streamlines in Fig. 4-4 show that the vortical structures along the ISL have a counter-clockwise motion (and a clockwise rotation in the upper ISL, not shown here) consistent with the flame wrinkling. These vortices can be due to the instability of the ISL vorticity sheet or also to helical instability of the swirling flow. The necessity of a vortex line to close on itself (away from a wall) suggests that the upper and lower ISL vortical structures are part of the same spiral vortex structure as shown in other studies [35, 72]. The vortical structures along the ISL, as indicated by the flame wrinkling, appear to have counter-rotating counterparts along the OSL.

This can be clearly observed in Fig. 6-6-($a_3$). Figures 6-6 shows also a wide range of wrinkle sizes; These can be as large as $\approx$ 8 mm in diameter i.e. approximately 1/5 of $D_{in}$ and larger than the methane laminar flame thickness estimated around 1.5 mm at these conditions. Few other observations can be made at this point based on the flame microstuctures uncovered by the OH-PLIF images; at $\phi = 0.60$ i.e. when the flame is only stabilized along the ISL, the flame appears to occasionally extend towards the ORZ. At $\phi = 0.66$, the flame appears along the OSL and extends deeply inside the recirculation zone as we can see in Fig. 6-6-($b_3$). We also observe the flame intermittently extending to the expansion section along the shear layer.

### 4.3.2 Flame transition to the ORZ/OSL

In this section we investigate the origin of the ORZ flame, from its inception to spreading and continuous presence. To this end, we focus on the equivalence ratio range between 0.60 and 0.66 at the reference operating conditions i.e. between the flames shown in Fig. 4-2. This is the range where the intermittent appearance of the flame in the ORZ is observed. Within this range, the probability ($P_{ORZ}$) of flame presence in the ORZ increases with the equivalence ratio. This probability was defined in chapter-3. $P_{ORZ}$ is equal to 0.002 for $\phi$=0.60 and equal to 0.995 for $\phi$= 0.66 signaling the end of the transition between flames III and IV.

The flame CH*-chemiluminescence signal integrated over the triangular region encompassing the ORZ (shown in Fig. 4-2) is plotted over time for $\phi$=0.62 at which $0 < P_{ORZ} < 1$. The result is shown in Fig. 4-7-(b); large intensity peaks (highlighted by the arrows on Fig. 4-7 correspond to the spread of the flame into the ORZ after having only unburnt reactants in that zone. Within the 4 seconds of data shown in Fig. 4-7-(b) this takes place 6 times but a major difference can be seen between the first five events and the last one occurring around t=3.2s; while the flame disappears from the

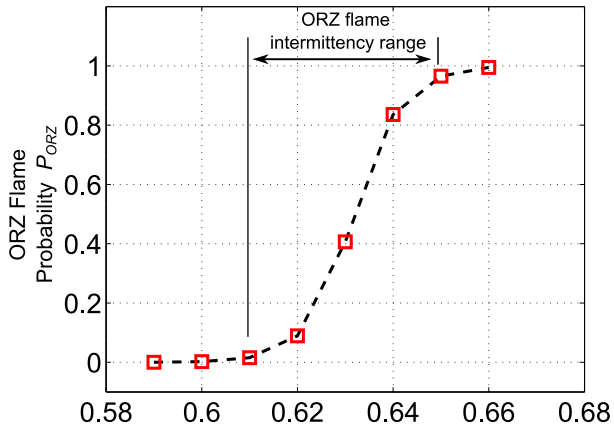


Figure 4-6: Probability of flame presence in the ORZ calculated from chemiluminescence images as the numbers of frames where the flame is in the ORZ over the total number of frames.

ORZ shortly after each of the first five peaks, at t = 3.2s it persists; remaining in the ORZ for a relatively longer time until t=3.7s. During this last event, the oscillatory signal seen in the zoomed-in version of the ORZ intensity signal in Fig. 4-7-(a) is due to the flame spinning inside the ORZ around the combustor centerline at a clearly defined tone. At the reference operating conditions this frequency is equal to 28 Hz which is in line with the results shown in the previous chapter. The ORZ flame spinning frequency will be analyzed in more detail in section 4.4.1. Both types of events — namely the fast appearance and disappearance of the of flame in the ORZ on the one hand, and, the appearance followed by flame rotation around the ORZ, on the other hand — are repeatedly observed at the transitional equivalence ratios.

We now focus on the first transition in the data set shown in Fig. 4-7 (b). This transition occurs between 820 and 920 seconds i.e. lasting approximately 100 ms, as shown in the zoomed-in box in Fig. 4-7 (c). The maximum intensity occurs at t = 861 ms. The corresponding line-of-sight dual flame chemiluminescence i.e. the simultaneous acquisition of both the top and side views of the combustor can be seen in Fig. 4-8 ranging from t=827 ms to t=861 ms. The flame images are binarized

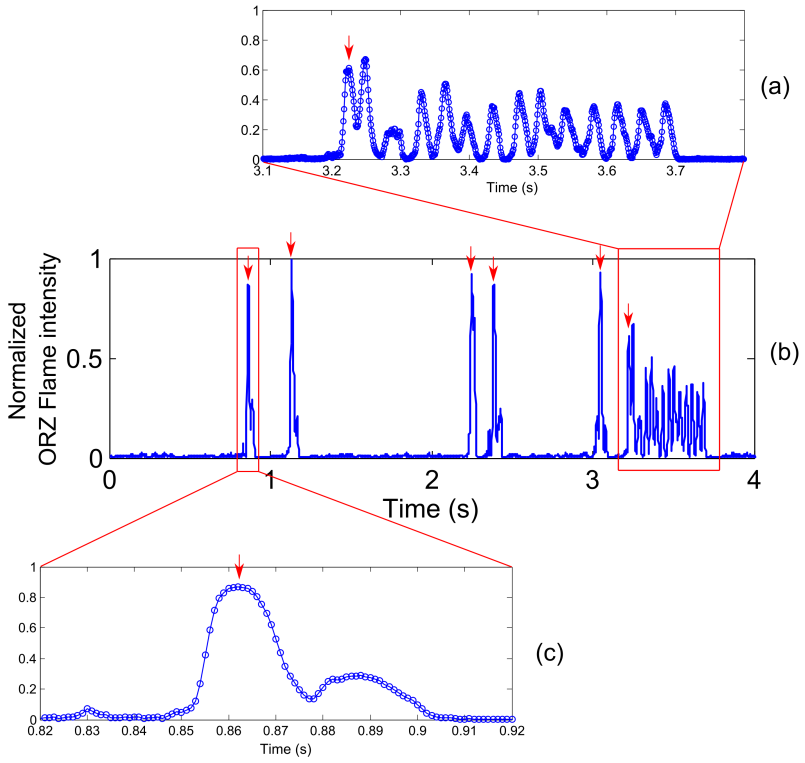


Figure 4-7: ORZ flame intensity as a function of time showing the intermittent appearance and disappearance of the flame in the ORZ ($\phi$=0.62).

here for clarity allowing easier visual tracking of the flame (flame brush in this case as it is subject to motion blur). At time t=828 ms a flame front extends out of the ISL flame before the jet impingement location on the wall. The form of the flame front reaching out to the ORZ at t=828 s suggests that it is entrained by a counter-clockwise vortex i.e. an OSL vortex as discussed earlier (Fig. 6-6). One millisecond later, a flame kernel detaches from the ISL flame and moves into the ORZ. When this burning zone disappears from the top view, it is captured by the side camera and can be further tracked. At time t=836 ms, the burning zone within the ORZ becomes larger as it expands while traveling azimuthally along the ORZ torus. This continues until the entire ORZ — initially filled with recirculating unburnt reactants — gets engulfed in the burning zone. Meanwhile the incoming swirling jet angle is

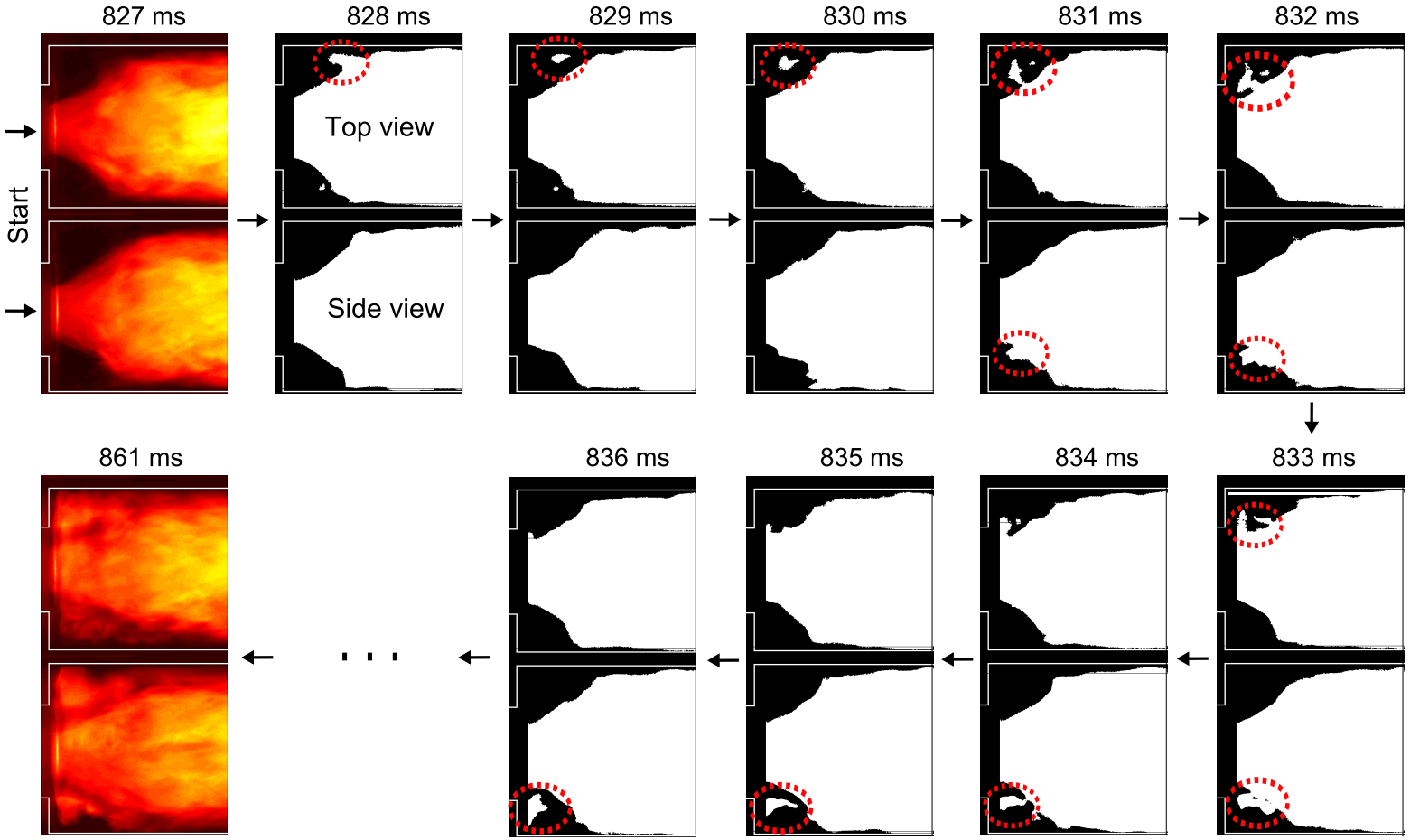


Figure 4-8: Consecutive binarized chemiluminescence images showing the ignition of the ORZ recirculating reactants ($\phi$=0.62). Images sampled at 1000 Hz with 1 ms exposure time using non-intensified camera.

reduced due to thermal expansion of the ORZ volume. This time corresponds to the maximum ORZ chemiluminescence intensity shown in Fig. 4-7-(c) (t = 861 ms). Each ignition of the ORZ is observed following a similar mechanism; we do not observe flame propagation along the side wall or flame propagation upstream directly along the OSL, at the experimental conditions studied here.

The use of two high speed cameras is critical for capturing the mechanism described above, that is the advection of a burning pocket from the ISL causing the sudden ignition of the ORZ. This two-camera approach captures the three dimensional and complex nature of the ORZ flame origin. This approach has its own limitations and should be complemented with other diagnostics, as only a rough visualization of the flame kernel can be obtained due to line of sight data and motion blur.

OH-PLIF is used to complement our interpretation of the data. Figure 4-9 shows non-consecutive OH-PLIF images, post-processed in the same fashion as in Fig. 6-6. These images confirm the intermittency of the flame appearance in the ORZ; in Fig. 4-9 (b) and (f) the flame does not appear in the ORZ in the interrogated plane. In (a), the snapshot shows a flame only in the upper side of the ORZ with a weakly connected reaction zone between the ISL and the ORZ. In (c), a flame exists in both sides of the ORZ. In this case, the flames along the ISL and in the ORZ/OSL are connected near the downstream side although the OH signal appears to be weak at the connection. Snapshot (c) suggests that the two shear layer flames get closer to each other as we go downstream. Figure 4-9 (b) and (f) shows also how the flame is wrinkled by the flow, and is entrained towards the ORZ. The flame entrainment in Fig. 4-9 (b) is opposite to the ISL vortices rotation. This suggest that the flame in the ISL is potentially entrained by vortical structures of the OSL towards the ORZ.

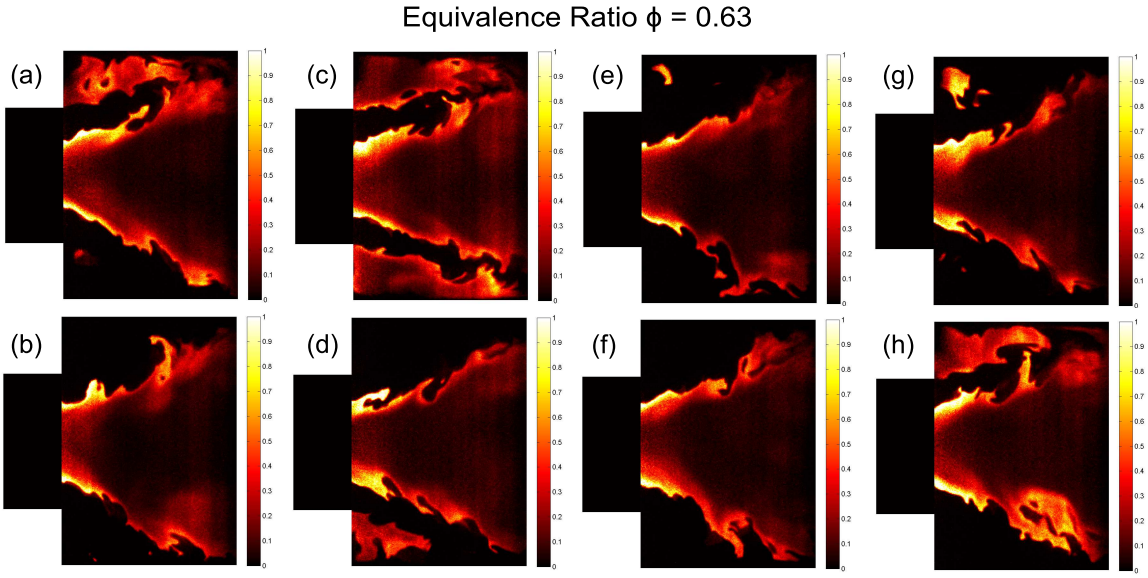


Figure 4-9: Non-consecutive OH-PLIF images of transitional flame III-IV (at $\phi$=0.63) showing the intermittency of burning in the ORZ and ISL flame occasionally extending towards the ORZ

### 4.3.3 ORZ Flame below the critical equivalence ratio

As we raised the equivalence ratio from that corresponding to flame III, the ignition of the ORZ started intermittently when $\phi$ reached a critical value $\phi_{onset} = 0.61$ (for which $P_{ORZ}$ become strictly non-zero). As documented earlier, the ignition of the entire ORZ region starts with a flame kernel entrained from the ISL flame. A natural question arises at this stage : can the flame reach the ORZ below $\phi_{onset}$ ? The answer lies in Fig. 4-10. The figure displays consecutive images acquired using an intensified high speed camera (taken at 2000 Hz with an exposure time of 0.25 ms) for an equivalence ratio lower than the critical value: $\phi = 0.58 < \phi_{onset}$, corresponding to an ISL only flame (flame III). The intensified camera was needed to compensate for the relatively low signal-to-noise ratio at this low equivalence ratio. In the zoomed-in portion of the flame snapshots, we see that even at lower equivalence ratio corresponding to flame III, a flame kernel can occasionally reach the ORZ following a similar mechanism as

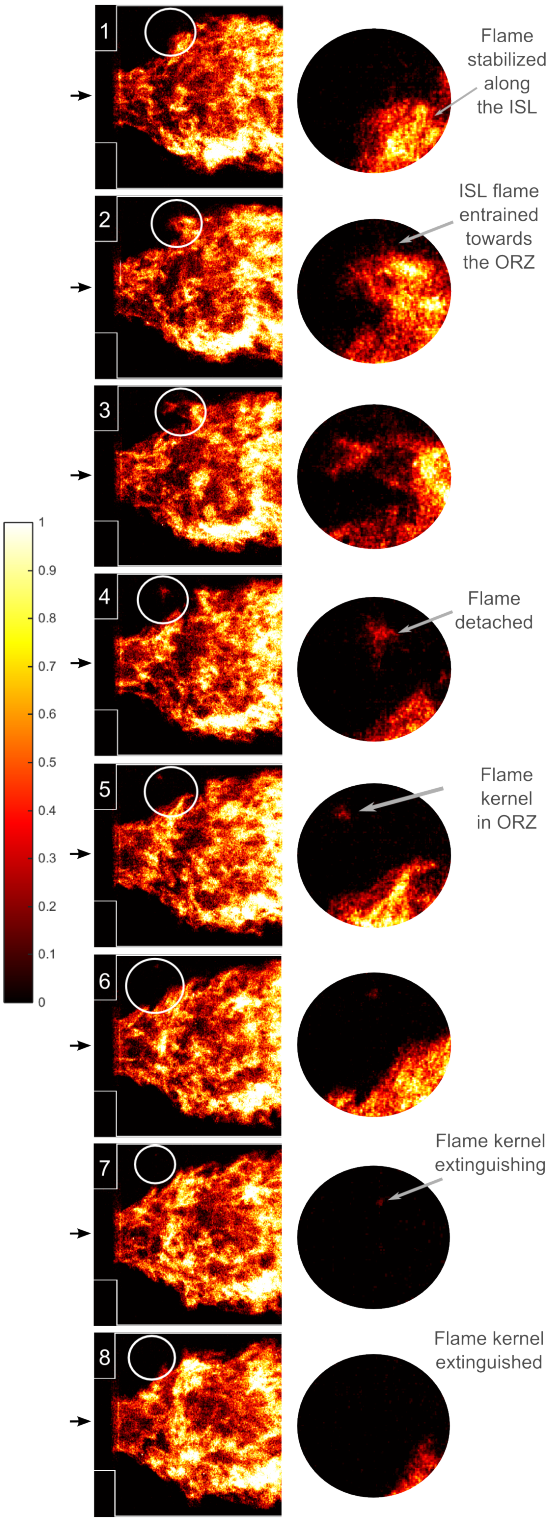


Figure 4-10: Consecutive intensified chemiluminescence images at $\phi$=0.58 (below the critical $\phi_{onset} = 0.61$) showing a flame kernel reaching the ORZ but failing to expand. Images taken at 2000 Hz with an exposure time of 0.25 ms using the HICAM intensified high speed camera.

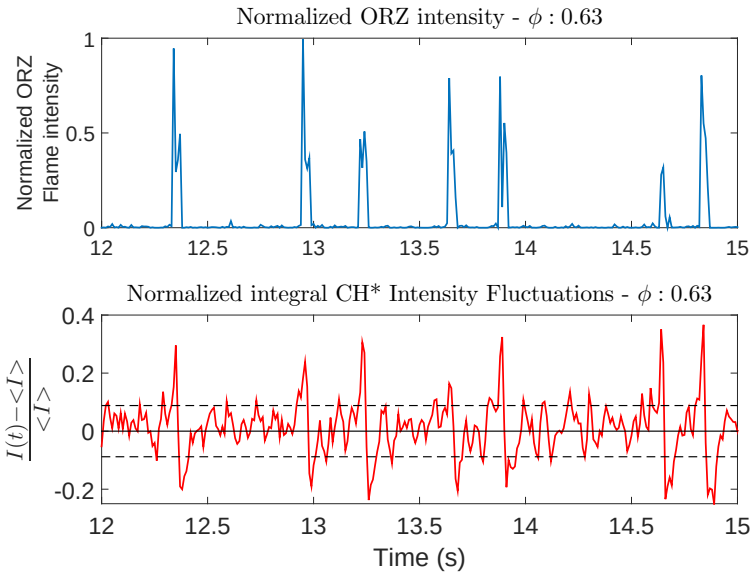


Figure 4-11: Synchronized ORZ-extracted chemiluminescence (top) and normalized integral flame intensity fluctuations (bottom) at $\phi$=0.63. Dashed line represents the standard deviation.

the one described earlier. However, in all these events with no exception the life time of such a kernel does not exceed 2-3 ms. The flame kernel quickly extinguishes failing to expand and ignite the ORZ reactants, and hence unable to initiate a flame in that region of the flow. The above result shows that a flame originating from the ISL can still reach the ORZ but there is a threshold (here in terms of $\phi$) beyond which the flame kernel is not extinguished and is capable of propagating within the ORZ and ultimately igniting the entire ORZ.

### 4.3.4 Consequence on heat release rate

The entrainment of a flame kernel towards the ORZ and the subsequent ignition of the recirculating reactants following the mechanism described above is concomitant with the sudden and relatively fast rise in the overall heat release rate. In Fig. 4-11, we can see this correlation as large peak-to-peak fluctuations in normalized overall CH*

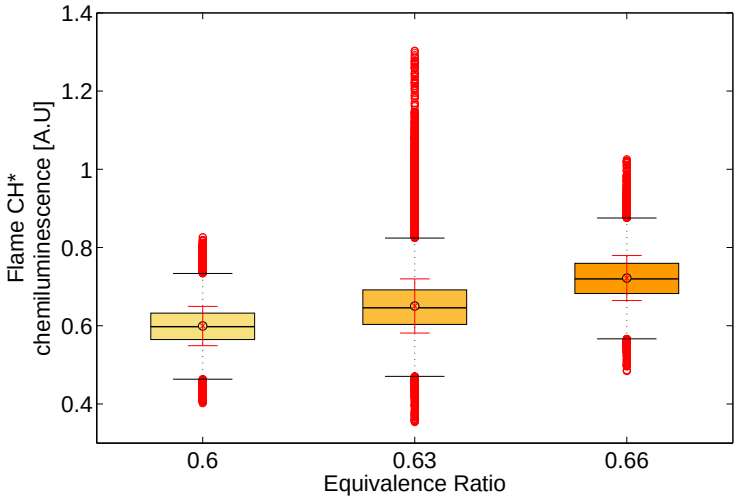


Figure 4-12: CH* radiation statistics for transitional flame (at $\phi$=0.63) as compared to flame III and flame IV: Mean (black circle), median (black line), standard deviation (smaller red whiskers), 25th and 75th percentiles (box edges), approximate 99.3% coverage (larger black whiskers) and outliers (red circles).

intensity (used as the surrogate for normalized heat release rate) appear simultaneously with spikes in ORZ intensity. The quick rise in overall CH* intensity is followed by a sharp drop below the average CH* level; during the latter phase, the ORZ products are evacuated and the region is replenishing with unburnt reactants.

The intermittency of the ORZ flame leads to a substantially different heat release rate distribution when compared with both flame III and IV as shown in Fig. 4-12: while the extreme heat release rate values obtained from flame III and IV are around 40% of the mean intensity, the “transitional" flame at $\phi$=0.63 is characterized by a larger number of outliers with peak values reaching more than 100% of the mean. The above results show that although the ORZ volume is small compared the volume encompassing the entire flame, its sudden and intermittent ignition has a impact on the overall heat release rate and constitute a non-negligible disturbance.

## 4.4 Effect of operating conditions

Thus far we analyzed the physical mechanism underlying the flame transition to the ORZ; we provided experimental evidence on how the transition takes place and its consequence, all at the reference case i.e. for pure methane as fuel at Re=20,000 and $\alpha_{sw} = 45$ deg. in a non insulated chamber. We found that a precursor to an OSL flame stabilization is the intermittent appearance of the flame in the ORZ along with its spinning at a clearly defined frequency. This flame originates from the ISL and it reaches the ORZ as a detached flame kernel. However, the flame kernel can only survive and propagate through the ORZ reactants above a certain threshold in terms of equivalence ratio. When changing the operating conditions (see Table 4.1) a similar sequence of events is observed. Here, we analyze the effect of changing the operating conditions on the spinning frequency of the flame when it appears in the ORZ as well as the change in $\phi_{onset}$ for a flame kernel to successfully ignite the ORZ.

| $H_2$% in $CH_4$ | $f_{ORZ}$ (1/s) | $\phi$ | $S_l^0$ (cm/s) | $T_{ad}$ (K) |
|---|---|---|---|---|
| 0% | 28.1 | 0.63 | 13.9 | 1719 |
| 10% | 28.3 | 0.60 | 12.4 | 1671 |
| 20% | 28.0 | 0.56 | 9.9 | 1604 |

Table 4.2: Effect of fuel composition on the ORZ frequency: change in flame spinning frequency around the ORZ as a function of the hydrogen content (by volume). The frequency is computed based on high speed images acquired at the equivalence ratio $\phi$ shown here. $S_l^0$ is the laminar burning velocity and $T_{ad}$ the adiabatic flame temperature calculated using GRI-Mech 3.0 [90] at an inlet temperature of 300 K.

### 4.4.1 Effect of operating conditions on the ORZ flame spinning frequency

At the reference conditions, the flame spinning dynamics takes place at a clear tone measured at $f_{ORZ} = 28.1$ Hz. This frequency is obtained by applying a Discrete Fourier

Transform algorithm to the flame chemiluminescence signal spatially integrated over the ORZ shown in Fig. 4-7 (a). When blending $H_2$ with methane, the intermittent transition and flame spinning in the ORZ are still observed but at lower $\phi$. Table 4.2 shows the ORZ flame spinning frequency obtained for different $CH_4$-$H_2$ mixtures along with the change in the laminar unstretched burning velocity and adiabatic flame temperature. When increasing the hydrogen content in the methane fuel mixture, the ORZ frequency is unchanged despite a non-negligible change in its thermo-chemical properties, as reflected by the laminar unstretched burning velocity and the adiabatic flame temperature. This result suggests that the spinning frequency of the flame is predominately of hydrodynamic nature. The latter statement can be confirmed by examining the flow field in the ORZ. The axial, radial and azimuthal velocity components of the ORZ (point A), the incoming jet (point B) and the IRZ (point C) are provided in Table 4.3 for the non-reacting flow at Re=20,000 and $\alpha_{sw} = 45$ deg. (reference inflow conditions). The location of these points (A, B and C) is displayed in Fig. 4-13. In addition to having a large turbulent intensity (of about 50% in terms of the mean azimuthal velocity), we see that the ORZ flow is predominately azimuthal : $|U_{\theta\,@A}| = 2.8\ m/s\ >>\ |U_{x\,@A}| > |U_{r\,@A}|$; although stereo-PIV is not available for the reacting cases, one can expect that the dominance of the azimuthal component to be still valid in the reacting flow. Along an average perimeter of the ORZ, thw non-reacting azimuthal velocity corresponds to a flow rotation frequency around 20 Hz. Although obtained from the non-reacting flow field, this frequency is of the order of the extracted flame spinning frequency ($f_{ORZ}$=28 Hz) as estimated by the following expression:

$$\frac{1}{f_{ORZ}} = \int_0^{1/f_{ORZ}} dt \approx \int_0^{2\pi} \frac{\bar{R}\, d\theta}{\bar{U}_\theta} = \frac{2\pi\bar{R}}{\bar{U}_\theta} \quad \Rightarrow \quad f_{ORZ} \approx \frac{\bar{U}_\theta}{2\pi\bar{R}}$$

with $\bar{U_\theta}$ being the average azimuthal ORZ velocity and $2\pi\bar{R}$ the average perimeter of the ORZ torus.

| Location | Statistics | $U_x$ | $U_r$ | $U_\theta$ |
|---|---|---|---|---|
| A (ORZ) | mean | -0.6 | -0.3 | -2.8 |
| A (ORZ) | rms | 1.0 | 1.1 | 1.4 |
| B (Jet) | mean | 8.3 | 2.4 | -5.7 |
| B (Jet) | rms | 3.2 | 2.1 | 2.5 |
| C (IRZ) | mean | -0.2 | 0.3 | -0.3 |
| C (IRZ) | rms | 1.5 | 3.3 | 3.0 |

Table 4.3: Mean and RMS Flow velocities (in m/s) for non-reacting flow showing the dominance of the azimuthal component in the ORZ. Pints A, B, C as shown in Fig. 4-13

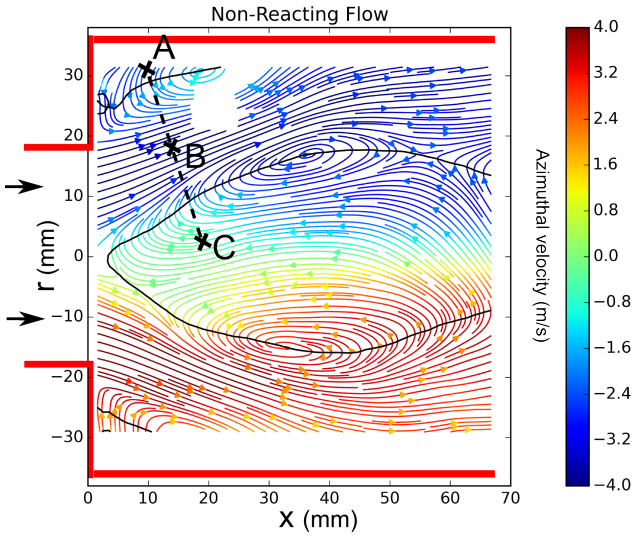


Figure 4-13: 2D velocity streamlines colored by azimuthal velocity. Points A (in the ORZ), (B) in the incoming swirling jet, and (C) in the IRZ are displayed. Values for these points are shown in Table 4.3

These results imply that the ORZ flame spinning frequency can be used as a surrogate for the mean azimuthal velocity in the ORZ i.e. for the flow field in the ORZ since this flow field is predominately azimuthal. This also means that the ORZ bulk azimuthal velocity can be extracted from simple chemiluminescence rather than stereo PIV.

Changing the inflow conditions (both the Reynolds number and the swirl number) is expected to change the flow field within the ORZ. This in turn is expected to change the flame spinning frequency ($f_{ORZ}$) but this needs to be confirmed: the same approach consisting in extracting the intensity of the flame chemiluminescence in the ORZ over time to compute the flame spinning frequency is performed at different Reynolds (from 15,000 to 30,000 solely by changing the upstream pre-swirler inlet bulk velocity $U_{in,b}$) and swirler blade angles (30 to 60 arc degrees). In this range, a linear dependence of $f_{ORZ}$ on the inlet bulk velocity is found for a fixed swirler blade angle. This dependence can be seen in Fig. 4-14; at a swirler angle of 45 arc degree, the ORZ spinning frequency changes from about 20 Hz at Re=15,000 to 42 Hz at Re=30,000, reflecting a proportional increase in the azimuthal flow velocity within the ORZ. Figure 4-14 shows also the effect of the swirl number through the blade angle change. Increasing the swirler blade angle at a fixed inlet velocity increases the flame spinning frequency. However, the $f_{ORZ}$=$f_{\alpha_{sw}}(U_{in,b})$ slope increases with the swirler blade angle. All lines tend asymptotically and logically to zero frequency for zero inlet bulk velocity, i.e. in the asymptotic situation of no flow.

The dependence of the ORZ flame spinning frequency $f_{ORZ} = f(U_{in,b}, \alpha_{sw})$ on both the inlet velocity and swirler angle can be combined within a unique non-dimensional number. It is common in the fluid dynamics literature to non-dimensionalize a frequency in such flows using the ratio of the inlet bulk velocity and inlet tube diameter to form a Strouhal number ($St = \frac{f_{ORZ}\, D_{in}}{U_b}$). Such an approach does not take into account the swirl number and fails to collapse all the curves drawn in Fig. 4-14. This method only succeeds in collapsing the data for each swirler angle separately, leading to a different St values for each angle. However, by including a non-linear trigonometric

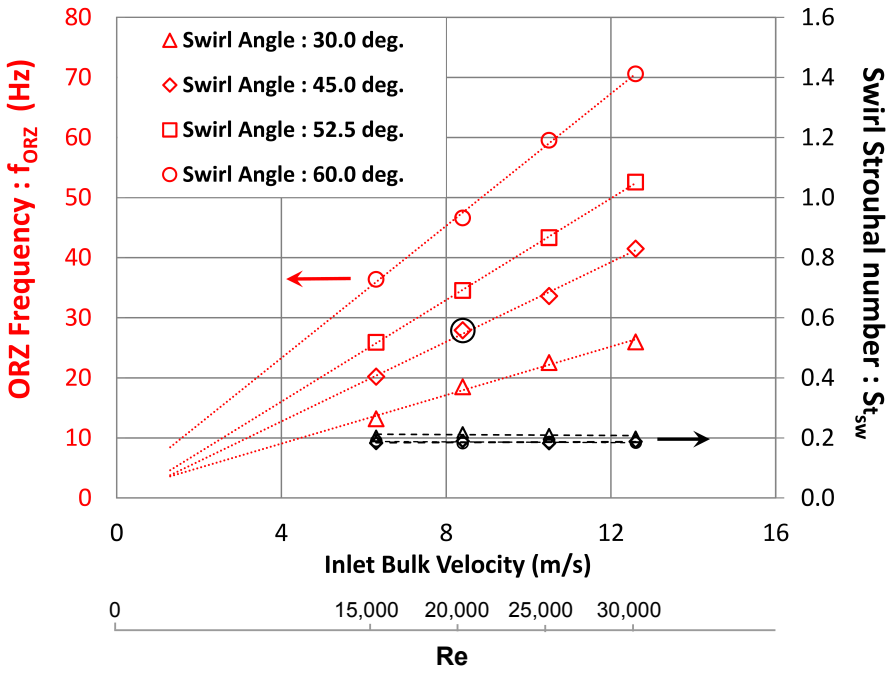


Figure 4-14: ORZ flame spinning frequency and Strouhal number as a function of inlet bulk velocity (and the Reynolds number) and swirler blade angle for pure methane. The frequency is computed from ORZ-extracted chemiluminescence at a transitional equivalence ratio for each operating condition. The circled value for $U_{in}$=8.4 m/s and $\alpha_{sw}$=45 deg. corresponds to the frequency at the reference conditions (28 Hz).

dependence on the swirl angle through tan($\alpha_{sw}$) such that :

$$St_{sw} = \frac{f_{ORZ}}{(\frac{U_b}{D_{in}})\ (\frac{2}{3}tan(\alpha_{sw}))} = \frac{St}{S}$$

all curves collapse and lead to a unique value of the swirl Strouhal number $St_{sw} \approx 0.19$ (note here that the 2/3 factor is added to let the approximation of the swirl number S by 2/3 $tan(\alpha)$ appear in the definition of $St_{sw}$). Therefore in this range of conditions $St_{sw}$ is constant and independent of the Reynolds number meaning that the ORZ spinning frequency is proportional to the inlet bulk velocity. This $St_{sw}$ definition includes the inlet (pre-swirler) velocity and the swirl number effects, all of which can be controlled by the operator and do not require measurements.

These results show also that the frequency can be predicted using the $St_{sw}$ expression. By knowing $\alpha_{sw}$ and $U_{in,b}$, the frequency can be computed (instead of measured from ORZ flame chemiluminescence) meaning that the mean azimuthal velocity in the ORZ can also be approximated.

### 4.4.2 Effect of operating conditions on the onset of an ORZ flame

**Effect of Inflow Conditions:**

The frequency of flame advection by the ORZ flow can be considered as a surrogate for the ORZ bulk azimuthal flow. Thus, we expect that higher Reynolds and swirl numbers lead to a stronger recirculation zone in terms of azimuthal velocity. Here, we investigate the effect of such changes on the equivalence ratio required for a flame to survive and expand in the ORZ when it reaches it.

We changed Re and $\alpha_{sw}$ again within the range [15,000-30,000] and [30-60] arc de-

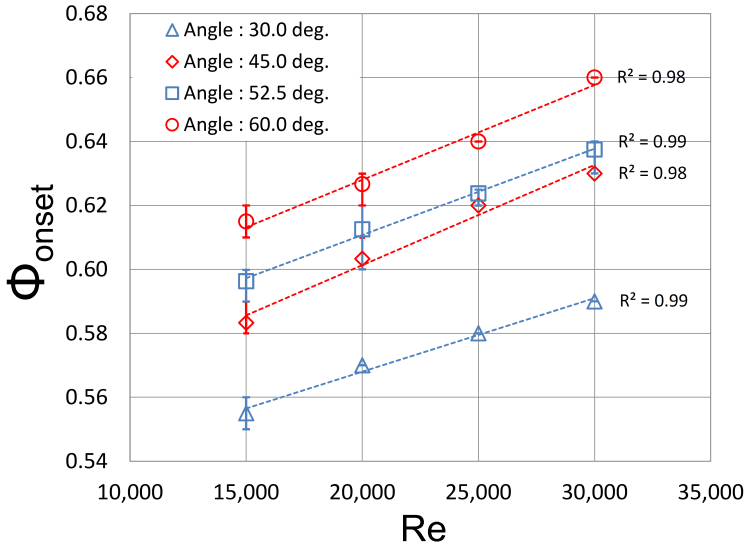


Figure 4-15: Effect of Re and S on $\phi_{onset}$. Error bars show the min and max over 3 realizations.

grees, respectively. The Reynolds number was controlled by changing the inlet bulk velocity upstream of the swirler, with no changes in density and dynamic viscosity. For each Re and $\alpha_{sw}$, the equivalence ratio is raised starting from lean condition corresponding the an ISL-only stabilized flame. The equivalence ratio at the onset of an ORZ flame is recorded and each experiment repeated three times. The results are shown in Fig. 4-15; when increasing the Reynolds number, while maintaining the swirler angle constant, a higher equivalence ratio is required to start observing a flame reaching, surviving and igniting the ORZ. Within the range of Re investigated, a linear monotonic trend is observed. A larger Re is expected to increase the magnitude of the incoming swirling jet velocity (all components proportionally) into the combustion chamber. As seen earlier, the azimuthal component of the ORZ flow also increases for larger Re as shown by the larger flame spinning frequency.

Increasing the swirler blade angle has also the effect of requiring a larger equivalence ratio to ignite the ORZ. Here also, a larger swirler angle leads to a larger azimuthal rotation of the ORZ flow. However, we expect here a weaker incoming jet in the axial-

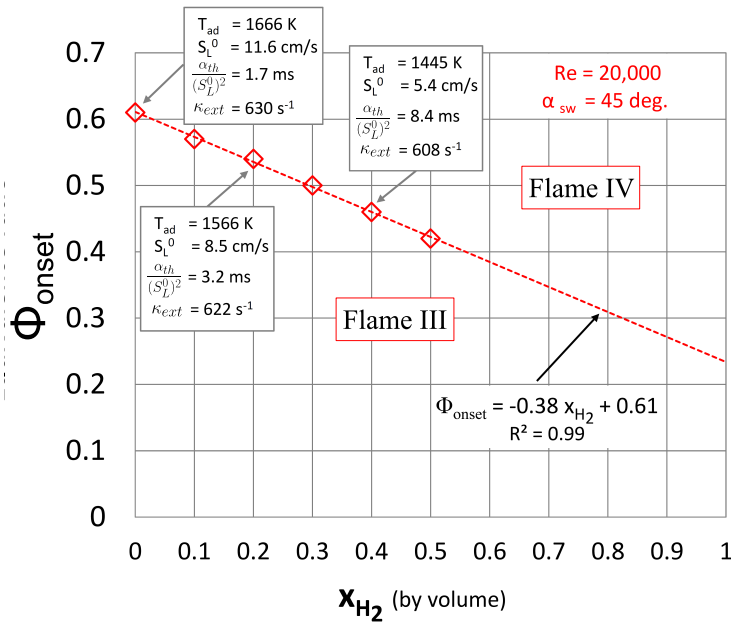


Figure 4-16: Change in $\phi_{onset}$ as a function of the $H_2$ volume fraction in the $CH_4$-$H_2$ fuel mixture. Boxes include the adiabatic flame temperature, the laminar unstretched flame speed, the ratio of the thermal diffusivity and the squared laminar unstretched burning velocity and finally the extinction strain rate all calculated using Cantera [27] and ChemkinPro [77] with GRI-Mech 3.0 [90] at an inlet temperature of 300 K.

radial direction since a larger swirler angle would shift a larger portion of the incoming axial momentum towards the azimuthal momentum.

**Effect of Fuel Composition:**

We now investigate the effect of fuel composition on $\phi_{onset}$. The fuel composition is modified by adding $H_2$ to $CH_4$ from a volume fraction of 0% to 50% at the reference inflow conditions (Re=20,000 and swirl angle of 45 deg.). Hydrogen addition is known to shift the transition between flame shapes to leaner equivalence ratio [82, 100]. The results, plotted in Fig. 4-16, confirm such a trend. In addition, a linear and monotonically decreasing trend is exhibited when the $H_2$ volume fraction is raised. For an equi-molar $CH_4 - H_2$ mixture, the onset of an ORZ flame takes place at $\phi_{onset}$=0.42 significantly lower than $\phi_{onset}$=0.61 required for pure methane.

**Effect of Thermal Boundary Condition:**

We now examine the effect of heat loss on the onset of an ORZ flame through different levels of insulation. Due to the difficulties of optical access for the fully insulated case, temperature measurements of the ORZ are used to infer the flame appearance in that region; the first ignition of the ORZ leads to a temperature spike recorded by the thermocouple. Starting at $\phi = 0.58$ (flame III) and after waiting for 2 minutes, the equivalence ratio is raised by 0.01 increment; a duration of 40 s is allowed between each increment to reach thermal quasi-steady state. Table 4.4 summarizes the results obtained over two ensembles in terms of $\phi_{onset}$ and the ORZ temperature before the first inflammation of the ORZ was recorded. The thermal conductivities of the different wall types are different by an order of magnitude leading to a different heat flux at the wall; table 4.4 shows that for the case with minimum heat loss (fully insulated case), $\phi_{onset}$ remains unchanged. Meanwhile, the ORZ temperature increases from an ensemble average of 412 K in the reference non-insulated case to 445 K in the fully insulated one but this has no effect on the ability of flame kernels reaching the ORZ to propagate and ignite the zone. This independence of $\phi_{onset}$ to heat loss at the ORZ boundary is consistent with the transition mechanism described earlier: the flame kernel detaches from the ISL and reaches the ORZ before reaching the wall.

| Insulation | $\phi_{onset}$ Test 1 | $T_{ORZ}$(K) Test 1 | $\phi_{onset}$ Test 2 | $T_{ORZ}$(K) Test 2 |
|---|---|---|---|---|
| Non insulated | 0.61 | 414 | 0.60 | 411 |
| Partially insulated | 0.61 | 417 | 0.60 | 414 |
| Fully insulated | 0.61 | 452 | 0.60 | 439 |

Table 4.4: Effect of heat loss at the ORZ boundary on $\phi_{onset}$ and ORZ temperature $T_{ORZ}$ at the reference operating conditions. Experiment repeated twice (Tests 1 and 2). $T_{ORZ}$ is the time average of the ORZ temperature over a 20 s period prior to the first ignition of the ORZ.

## 4.5 Modeling the transition of the flame to the ORZ

Scaling the transition to an OSL stabilized flame remains a challenge, due in part to the lack of insight on the physical mechanism, and need to understand the characteristics of the flow field within the ORZ i.e. where the flame first appears. In section 4.3, we addressed the former limitation and described the different steps leading to the onset of an OSL flame. This mechanism is valid for our combustor geometry; for different designs (for instance smaller expansion ratios), different mechanisms may exist (such as the flame flashing back along the wall [29]). The second limitation was addressed in section 4.4: the predominately azimuthal turbulent flow in the ORZ was linked to the ORZ flame spinning frequency — a phenomenon taking place during the transition — which was found to be scalable using a Strouhal number. In this section, building on these insights, we propose a model for this transition. Our hypothesis is the following: when a flame is capable of expanding and not extinguishing when reaching the ORZ, a characteristic flame time scale ($\tau_{flame}$) should be of the same order of magnitude as a characteristic time scale of the flow ($\tau_{flow}$) within the ORZ. This flow time scale should reflect the flow conditions the flame kernel reaching the ORZ finds when entrained in that region.

Based on our previous results, a natural choice for $\tau_{flow}$ is the inverse of the ORZ flame spinning frequency. This is the time for the average ORZ flow to do one revolution around the combustor's centerline. A local version of the same time scale is $\tau_{ORZflow} = 1/(2\pi\ f_{ORZ})$. This frequency reflects the flow condition in the ORZ and it can also capture simultaneously the effect of the Reynolds and swirl numbers. As we will see later, $(2\pi\ f_{ORZ})$ can be interpreted as a quantity proportional to the bulk azimuthal strain rate in the ORZ.

The choice of the characteristic flame time scale $\tau_{flame}$ is less straightforward. Po-

tential candidates for a flame time include:

- The ratio of the thermal diffusivity and the squared laminar unstretched burning velocity ($\frac{\alpha_{th}}{(S_L^0)^2}$). However, this time scale fails to capture the onset of an ORZ flame; Fig. 4-16 (see boxes) displays the adiabatic flame temperature, laminar unstretched burning velocity as well as $\frac{\alpha_{th}}{(S_L^0)^2}$, all evaluated at $\phi_{onset}$. This is shown for 0%, 20% and 40% $H_2$ at the reference inflow conditions with similar $f_{ORZ}$ i.e. similar ORZ flow conditions. The results show that none of these combustion properties governs the transition of interest here. In particular, this choice of flame time scale leads to a large scatter from 1.7 ms for pure methane to 8.4 ms for a methane mixture with 40% $H_2$. A variant of this approach is to rely on a strained consumption speed to include the effect of the strain rate on chemistry; this was previously applied successfully to scale dynamic modes in a premixed combustor [93, 34]. However, such an approach requires a knowledge of the strain rate to compute the strained consumption speed which is a difficult task in complex geometries like swirl-stabilized combustors.

- The ratio of the thermal diffusivity and the squared turbulent flame speed ($\frac{\alpha_{th}}{(S_T)^2}$). The difficulty in this method is the choice of a suitable turbulent flame speed correlation. Although most correlations agree on the dependence of turbulent burning velocity on the flow velocity fluctuation u' and $S_L^0$ as $S_T \propto u'^{0.5}\ (S_L^0)^{0.6}$, other dependences like the Lewis number effect (as proposed by Kido et al. [46, 67]) are not fully established [58]. Another difficulty is the need to use an effective Lewis number for fuel mixtures and this choice is also not straightforward [8, 103]. The knowledge of u' may also be a hurdle when choosing this approach.

- Yet another option for a characteristic flame time scale is the inverse of the extinction strain rate ($\frac{1}{\kappa_{ext}}$). The extinction strain rate has been proposed in the past

to explain the transitions between different flame macrostructures and dynamic modes in a swirl-stabilized combustor [19, 84] as well as flame anchoring/lifting [110]. It has the advantage of being easily computed. Such a choice takes into account fuel composition effect and also embeds thermo-diffusive effects.

Here, we choose the inverse of the extinction strain rate as a characteristic flame time scale. The extinction strain rate is calculated using a two dimensional opposed flow model under laminar conditions using ChemkinPro [77] with GRI-Mech 3.0 [90] for chemical kinetics and including multicomponent transport and Soret effect. . Combustion at the conditions studied in this chapter, is turbulent and expected to take place in the “reaction sheet" or “thin reaction zone" regime of the Borghi-Peters diagram [74] which is confirmed qualitatively by OH-PLIF results in Fig. 6-6. Under such regime, it is generally accepted that, locally, the flame can be considered as laminar and strained. A limitation of using the extinction strain rate is that it cannot capture the turbulence effect of enhancing both transport and chemistry.

Based on the choices made above for the time scales, we can define an ORZ Karlovitz number ($Ka_{ORZ}$) as follows:

$$Ka_{\,ORZ} = \frac{\tau_{flame}}{\tau_{ORZ\ flow}} = \frac{1/\kappa_{ext}}{1/2\pi f_{ORZ}} = \frac{2\pi f_{ORZ}}{\kappa_{ext}}$$

$\tau_{flame}$ and $\tau_{ORZ\ flow}$ are computed at $\phi_{onset}$ for each of the operating conditions spanning the (Re, $\alpha_{sw}$, $x_{\mathrm{H_2}}$) space, at ambient pressure (1 bar) and temperature (300 K) with no added insulation. $\tau_{flame}$ is plotted against the flow time scale and the result is shown in Fig. 4-17. the following correlation is found and the trend is well captured by the linear least-square fit:

$$\tau_{flame} = 0.19\ \tau_{ORZ\ flow}\ +\ 0.66$$

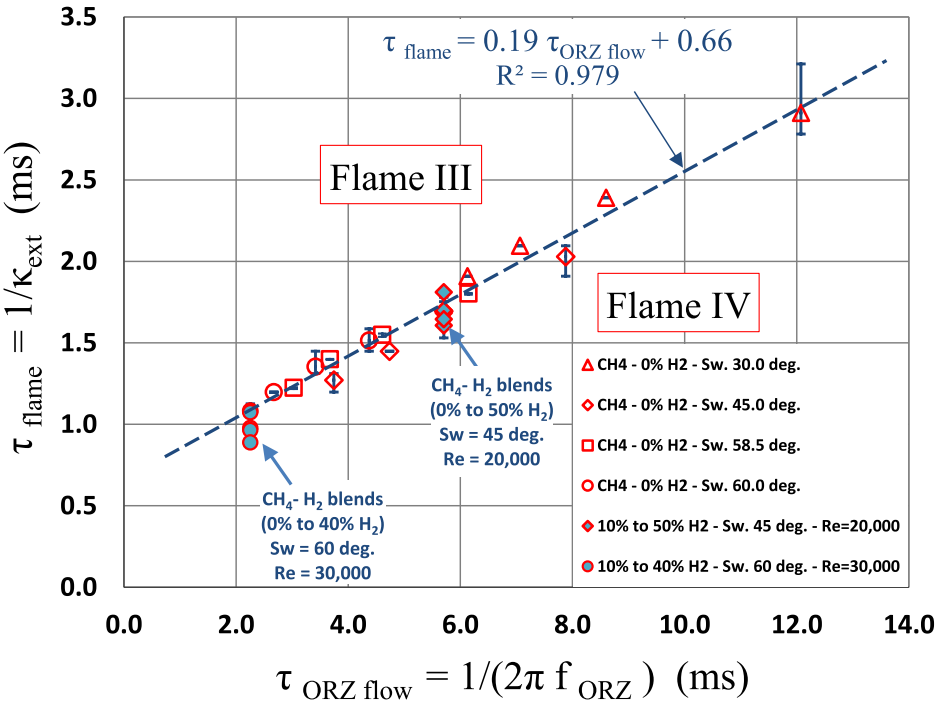


Figure 4-17: Characteristic flame time versus characteristic ORZ flow time. Each data point correspond to a transition of the flame to the ORZ in the (Re, $\alpha_{sw}$, $x_{H_2}$) space. The vertical error bars stem from the uncertainty obtained on $\phi_{onset}$ for which experiments were repeated three times.

Within the explored range, $\tau_{flame}$ is proportional to $\tau_{ORZ\ flow}$ leading to a constant Karlovitz number. Flame III will typically have a Karlovitz number larger than $Ka_{onset}$ and chemistry is too slow compared to the ORZ flow time scale. As the equivalence ratio is raised or $H_2$ is added, $Ka$ decreases and when reaching the critical value, the flame is able to expand in the ORZ, ignite it and ultimately stabilize along the OSL.

This model provides a criterion that captures the transition from flame III to IV in swirling flows. Using this criterion, the transition to an ORZ flame can be predicted for any combination of fuel, swirl and Reynolds numbers in a swirling flow design similar to the one studied here. It is based on variables that can be either numerically calculated (like the extinction strain rate) or measured like the ORZ flame spinning frequency. This approach is made even simpler knowing that a single constant Strouhal number

($St_{sw}$) embeds the effects of the inlet bulk velocity and swirl number and can be used to estimate the ORZ spinning frequency. The framework described here is valid when the physical mechanism responsible for the flame appearance in the ORZ is similar to the one highlighted earlier in this chapter.

**Additional interpretation:** The above scaling can be seen as a balance between a characteristic flame time to the ORZ flow time scale but also as the ratio of the bulk hydrodynamic strain rate that the flame would be subject to when reaching the ORZ to the flame extinction strain rate. Indeed, the ORZ flame spinning frequency $f_{ORZ}$ can be interpreted as an approximation of this bulk strain rate within the ORZ; based on previous results showing the dominance of the azimuthal component in the ORZ flow field, an average hydrodynamic strain rate in the ORZ can be approximated as follows:

$$\bar{\epsilon} \approx \frac{\Delta \overline{U_\theta}}{\Delta x} \approx \frac{(\overline{U_\theta} - 0)}{L_{ORZ}} \approx \frac{2\pi \bar{R} f_{ORZ}}{L_{ORZ}}$$

with $\overline{U_\theta}$ the average azimuthal velocity, $L_{ORZ}$ the ORZ length and $2\pi\bar{R}$ an average ORZ perimeter. From the PIV data shown in Figs. 4-4 and 4-5, $\bar{R} \approx \frac{3}{2} D_{in}$ and $L_{ORZ} \approx D_{in}$ giving: $\bar{\epsilon} \approx 3/2$ x $2\pi f_{ORZ}$ and hence relating the ORZ flame spinning frequency to the bulk strain rate in the ORZ. Following this interpretation, when the extinction strain rate of the flame (predominately dictated by the fuel composition and the equivalence ratio) becomes larger than the ORZ strain rate (predominately dictated by the inlet velocity and the swirler angle) the flame kernel originating from the ISL and entrained into the ORZ will not extinguish and will be capable of expanding and igniting the ORZ reactants leading ultimately to the new flame macrostructure.

**Scaling the onset of thermo-acoustic instability in the acoustically coupled combustor:** The ORZ Karlovitz number defined allowed the scaling of the onset of combustion in the ORZ. In **chapter**-3, we showed that the flame transition to the ORZ is concomitant with the onset of thermo-acoustic coupling. This means that the proposed scaling parameter should also allow the scaling of the onset of limit cycle oscillations. This is confirmed as it can be seen in Fig.4-18; when replacing the equivalence ratio by the inverse of the ORZ Karlovitz number, the stability maps collapse and the onset of coupling takes place at a unique value of the scaling parameter for both fuel mixrtures (pure methane and methane with 20% $H_2$).

## 4.6 Chapter Conclusion and Next Step

The goal of this study was two-fold: first, investigate the mechanism underlying the flame appearance in the outside recirculation zone in a canonical swirl-stabilized combustor as well as its dominant dynamics. Second, propose a predictive criterion for its occurrence. We reached the following conclusions:

1. A dual camera approach using two perpendicular, simultaneous and time resolved chemiluminescence, combined with OH-PLIF measurements allowed us to elucidate the mechanism through which the flame transitions to the OSL. We found evidence that the flame — initially stabilized along the ISL — is entrained towards the ORZ and a detached reactive kernel causes it to ignite.

2. This flame kernel is an ignition source deposited in the ORZ initially filled with reactants. At the critical equivalence ratio corresponding to the onset of the flame transition, it can successfully ignite the entire ORZ reactant region. Below the critical equivalence ratio, we showed that a flame kernel can still occasionally

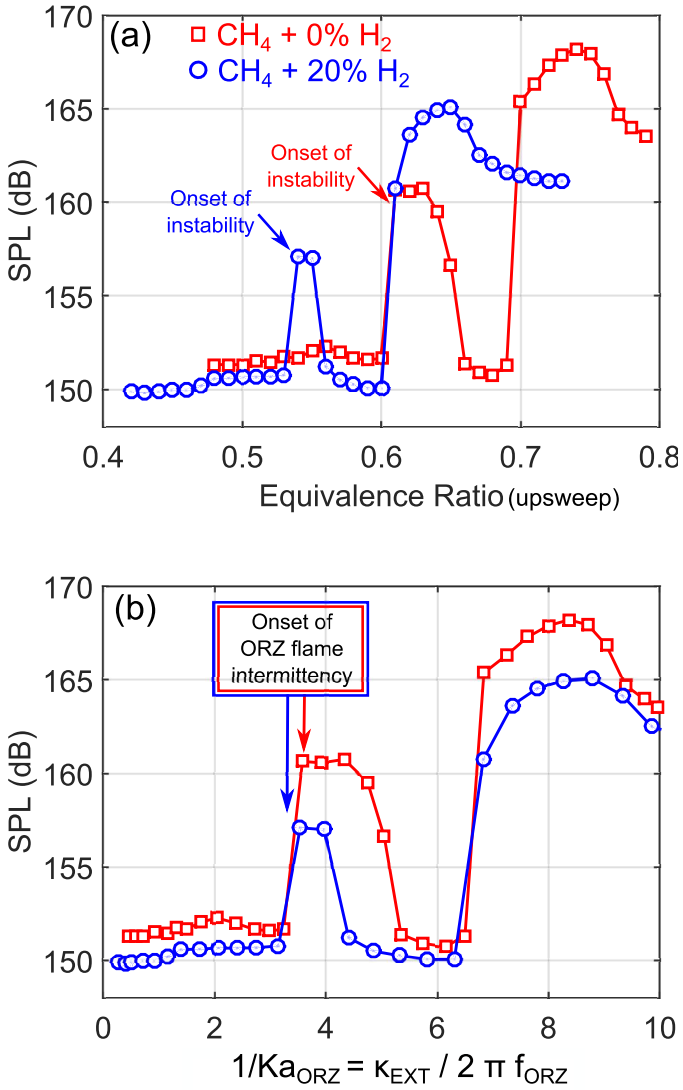


Figure 4-18: (a) Stability maps for methane (red squares) and methane with 20% $H_2$ (blue circles) with the equivalence ratio as parameter. (b) Stability maps for methane (red squares) and methane with 20% $H_2$ (blue circles) with the inverse of the ORZ Karlovitz number as parameter. The onset of thermo-acoustic coupling and the onset of ORZ flame intermittency is shown.

reach the ORZ, but always fails to expand.

3. The intermittent spinning of the flame, advected by the predominately azimuthal ORZ flow, is one of major dynamics associated with the transition from flame III to flame IV. We showed that this motion can be captured by a single swirl Strouhal number that embeds the effect of both swirl and inlet bulk velocity.

4. We showed that the transition to an ORZ flame is independent of the heat flux at the ORZ boundary and is governed by a balance between the extinction strain rate and the ORZ flame spinning frequency, defined as $Ka_{ORZ}$. For different operating conditions (Re, $\alpha_{sw}$, $x_{\mathrm{H}_2}$, $\phi$), when chemistry is fast enough the flame is able to survive in the ORZ flow, ignite it and ultimately stabilize along the OSL. This can also be interpreted as the extinction strain rate of the flame exceeding the bulk azimuthal strain rate approximated by the ORZ flame spinning frequency.

5. When successful, the sudden and intermittent ignition of reactants recirculating in the ORZ leads to large fluctuations in the overall heat release rate, which is one of the main consequence of the transition. This strongly suggest that this sudden ignition is to be considered as a potential mechanism leading to thermo-acoustic instability.

6. The ORZ Karlovitz number allows also a successful scaling of the onset of thermo-acoustic coupling (in the acoustically coupled combustor studied in **chapter**-3) across different fuel compositions.

The investigation undertaken in this chapter differs from previous studies in different important aspects; first, no assumption was made on the appearance of the flame to the ORZ but rather we start with exploring the mechanism leading to it. Second, a

wide range of operating conditions, including different ORZ insulation, were explored affecting the chemistry (primarily through the addition of hydrogen to methane up to 50% by volume) and the flow (primarily through different Reynolds numbers and swirl angles. In our study, although a large range of operating and fuel conditions was investigated, only $CH_4 - H_2$ combustion in Air were used to build and test our predictive model. In the following chapter, we will extend this study by testing its validity to oxy-combustion.

# Chapter 5

# ORZ/OSL Flame Stabilization in Oxy-Combustion

## 5.1 Introduction

Oxy-flame combustion with carbon capture is also among the promising technologies for cleaner power generation using fossil fuels, along with pre-combustion technologies. In premixed oxy-combustion, carbon dioxide ($CO_2$) is used as diluent to control the flame and turbine inlet temperatures. In this chapter, we will investigate the transition from flame III to IV in oxy-combustion in the same swirl combustor previously used in the previous chapter for air combustion.

### 5.1.1 Oxy vs. Air flame combustion

Modern premixed gas turbines have been historically designed and optimized for air combustion. Several issues, like flammability and combustion instabilities, may arise when switching to oxy-combustion.

Changing the diluent from Nitrogen ($N_2$) to $CO_2$ impacts the flame and the combus-

tion process because of the differences in thermo-physical properties, chemical kinetics and radiation properties [11, 26, 1, 88, 108]; $N_2$ and $CO_2$ have notable differences in density, specific heat capacity and diffusivities. $CO_2$ impacts the chemical kinetics by affecting the radical pool mainly through the reaction $CO_2 + H \rightleftarrows CO + OH$ [7]. Moreover, the $CO_2$ dominated combustion products lead to more radiative heat exchange with the surroundings, compared to air-flames.

There have been a number of studies on premixed methane ($CH_4$) oxy-flames in swirl-stabilized combustors. Shroll et al. [88] investigated dynamic stability characteristics of premixed $CH_4/O_2/CO_2$ and $CH_4/O_2/N_2$ mixtures in a swirl combustor. Oxy-flames were kept at stoichiometric conditions, which is the practical operating condition owing to the relatively large $O_2$-separation cost; variable $CO_2$ dilution levels were used to keep the same adiabatic flame temperature as the air-flame. They found that the transition between thermo-acoustic modes is a function of the adiabatic flame temperature.

Watanabe et al. [108] compared air-flames and oxy-flames in a premixed swirl combustor identical to the one considered in this thesis. When comparing oxy and air flame with the same inlet Reynolds and swirl numbers, adiabatic flame temperature and equivalence ratio (lean), they found differences in flame stabilization.

In another recent study, the effects of swirl number and flame temperature on the lean stability and shapes of premixed air and oxy-flames were analyzed by Jourdaine et al. [42] in a swirl combustor. The $CO_2$-diluted flames were found to be less stable than the $N_2$-diluted flames at Re $< 20{,}000$; however, air and oxy-flame shapes matched when the swirl numbers and adiabatic flame temperatures were the same for both.

Runyon et al. [80] studied the flame structures and emissions that result from premixed methane-oxygen and methane-air mixtures in a swirl-stabilized burner at varying thermal power and pressure. Oxy-flames demonstrated stable combustion at a

range of thermal powers and pressures (up to 3 bar) confirming the possibility to retrofit existing air combustion designs. They also highlighted a change in flame structure that they attribute to changes in transport properties and chemistry.

Amato et al. [1] focused on the lean blowoff limit and showed that the operability boundaries of a $CO_2$ diluted system reduces significantly compared to methane-air mixtures in a premixed swirl combustor; this was attributed to the slower kinetics of the $CH_4/O_2/CO_2$ mixture. The $CO_2$ diluted mixture was found to blow off at adiabatic flame temperatures about 300 K higher than the air mixture for a given nozzle exit velocity, showing that the adiabatic flame temperature does not govern the flame static stability.

Finally, work on oxy-combustion has been done also in a swirl combustor by Kutne et al [50] at atmospheric conditions. The $O_2$ mole fraction in the oxidizer mixture, as well as the equivalence ratio and thermal power were varied to study the flame macrostructure and static stability at lean conditions. The inlet Reynolds number and velocities were not directly controlled. Here, an enhanced stability (leaner blowout limit) was found as the $O_2$ fraction in the oxidizer was raised; they attributed this observation to the change in laminar flame speed and Reynolds number.

When comparing air and oxy combustion, some parameters need to be held constant in order to isolate the desired effect, like often thermo-chemical effects in the case of oxy-flames. Some kept the inlet Reynolds number constant to satisfy dynamic similarity. Others kept the thermal input constant, driven by a more practical need for testing the retrofit of existing air combustor. Other studies compared oxy and air flames at the same adiabatic flame temperatures to keep similar turbine inlet temperature, a major constraint in gas turbine combustion. The choice of the inlet parameter to be controlled is crucial and will be an important part of the current study.

### 5.1.2 Operating Conditions and Procedure

We vary the equivalence ratio, the inlet velocity and the inlet Reynolds number in order to compare air and oxy-combustion and isolate thermo-chemical effects; all other parameters are held constant (including the inlet temperature of 300 K). For oxy-combustion, at each equivalence ratio, $CO_2$ mole fraction is adjusted to obtain the same adiabatic flame temperature at the same equivalence ratio, when compared to air combustion. The procedure to identify the critical equivalence ratio ($\phi_{onset}$) at which the flame appears in the ORZ is the following: for each operating condition, we start from lean conditions (close to blowoff) and gradually raise the equivalence ratio; when the flame appears in the ORZ, $\phi_{onset}$ is recorded along with high speed flame chemiluminescence during the intermittent transition. Chemiluminescence is then used to compute the ORZ flame spinning frequency ($f_{ORZ}$) introduced earlier. Each $\phi_{onset}$ measurement is repeated three times; the mean value is plotted along with the error bar.

### 5.1.3 Chapter Goal and Outline

In this chapter, we investigate the transition from flame III to IV in oxy-combustion in the same swirl combustor previously used in the previous chapter for air combustion. Our working hypothesis here is that oxy-flame appearance in the ORZ is also governed by a balance between the extinction strain rate and the prevailing strain rate in the ORZ. *The goal of this chapter's study is to test the validity of this hypothesis and determine which flame property governs its transition to the ORZ in swirl-stabilized oxy-combustion.*

The different parts of the chapter will answer the following questions:

1. How does the critical equivalence ratio at which the flame appears in the ORZ

changes when switching from air to oxy-flames ? (section 5.2.1-a)

2. When comparing air vs oxy-flame, what inflow parameters need to be maintained in order to impose a similar flow field in the ORZ ? Is the ORZ Strouhal number independent of the Reynolds number when changing the fluid's kinematic viscosity from air to oxy-combustion ? (section 5.2.1-b)

3. Can the extinction strain rate be used as a scaling parameter for flame stabilization in the ORZ/OSL in both air and oxy-combustion ? at what temperature should the extinction strain rate be computed ? (sections 5.2.2)

## 5.2 Results and Discussion

### 5.2.1 Flame III to IV For Air vs. Oxy flames

**a - Critical Equivalence Ratio:**

We start by comparing the critical equivalence ratio at which the flame appears in the ORZ ($\phi_{onset}$) for air and oxy-flames. First, the inlet Reynolds number (Re) is maintained constant; to do so, the inlet velocity is lowered to compensate for the change in dynamic viscosity (-12%) and density (+37%) when switching from $N_2$ to $CO_2$ as diluent. Figure 5-1-(a) illustrates the dependence of $\phi_{onset}$ on Re; increasing Re requires a higher equivalence ratio for both air or oxy flames. Moreover, for a fixed Re, the air flame requires a higher equivalence ratios to appear in the ORZ, e.g. at Re=20,000, the oxy-flame's first appearance in the ORZ occurs at $\phi$=0.59 while it takes place at $\phi$=0.60-0.61 for the air-flame. Although small, this difference is statistically significant as shown by the repeated measurements and displayed error bars. The trends are different when fixing the inlet velocity; in Fig. 5-1 (b), $\phi_{onset}$ is now plotted against the inlet bulk velocity. The interesting observation here is the existence of an

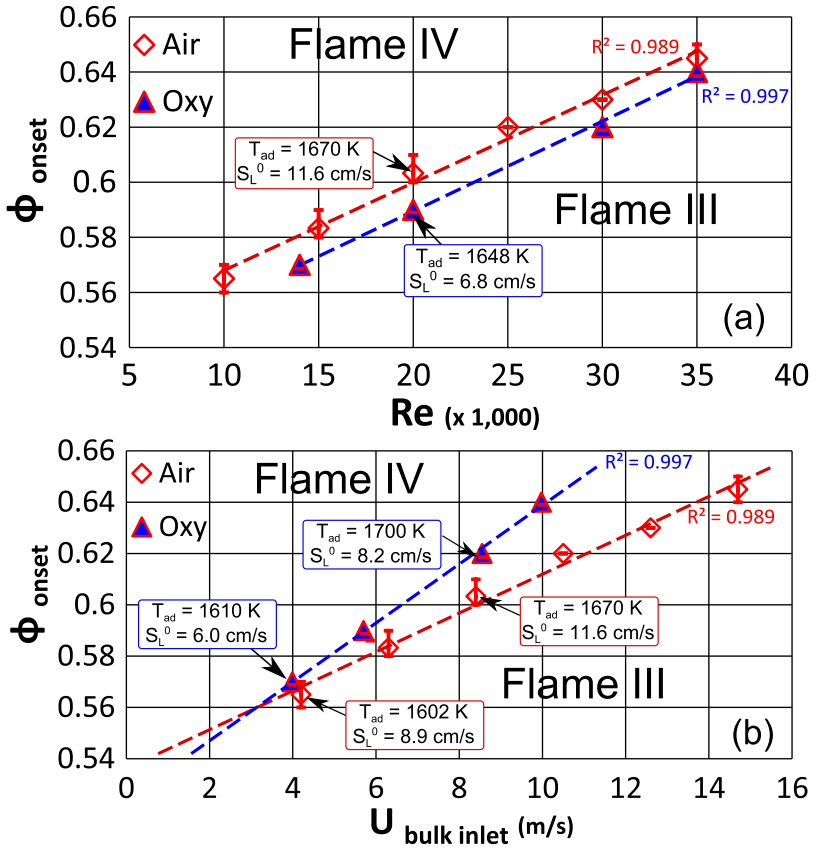


Figure 5-1: Effect of inlet Reynolds number (a) and inlet bulk velocity (b) on the critical equivalence ratio. Each measurement is repeated three times and error bars displayed. Linear least square fit lines are shown along with the corresponding $R^2$.

equi-transition point at an inlet velocity of about 3 m/s; at this inflow condition, both air and oxy flames appear in the ORZ at the same equivalence ratio $\phi^* \approx 0.56$ as $\phi$ is raised.

When switching from air to oxy combustion, thermochemical properties change; in order to isolate the effect of these changes on the transition from Flame III to IV, a similar flow field needs to be imposed. The question is: which of the inlet velocity or inlet Reynolds number lead to a similar flow field in the ORZ ? As mentioned in the introduction, the ORZ flame spinning frequency obtained during the intermittent appearance of the flame in that region is a surrogate for the azimuthal flow and the

bulk strain rate that the flame is subject when it reaches ORZ. In the following section, the variation of this frequency with both Re and inlet velocity will be analyzed to determine which of these two parameters is more suitable to impose similar flow field in the ORZ/OSL to both air and oxy-flames.

**b - Independence of the Strouhal number on Re:**

The transition between flame III and IV for both air and oxy-flames takes places intermittently over a range of equivalence ratios; during this intermittent ORZ flame regime, the flame is spinning at a frequency $f_{ORZ}$ that is predominately dictated by the flow and is independent of the fuel and the equivalence ratio [102]. $f_{ORZ}$ is obtained by applying the Fast Fourier Transform (FFT) algorithm to the flame chemiluminescence signal spatially integrated over the ORZ at $\phi_{onset}$. Figure 5-2 depicts $f_{ORZ}$ for both air and oxy flames as a function of the Reynolds number (a) and the inlet bulk velocity (b). If we consider the air and oxy flame at the same Reynolds number of 20,000, which corresponds to $U_{in}$ = 8.4 and 5.4 m/s for air and oxy respectively due to difference in kinematic viscosity, the corresponding spinning frequencies are $f_{ORZ,air}$= 27 Hz and $f_{ORZ,oxy}$ 19 Hz. However when comparing the frequencies for the same inlet velocity the air and oxy flames' plots collapse despite the different density and dynamic viscosity. This shows that, in the range of conditions studied here, the Strouhal number is independent of the Reynolds number (see Fig.5-2-(c)) making $f_{ORZ}$, hence the ORZ flow dynamics only dictated by the inlet velocity.

The above result has the important implication that, in order to maintain similar flow conditions in the ORZ when comparing air vs oxy, it is more relevant to fix $U_{in}$ rather than Re. Based on this result, we now know that the experiment shown in Fig. 5-1-(b) is more relevant than Fig. 5-1-(a) in isolating thermochemical effects on the ORZ flame transition.

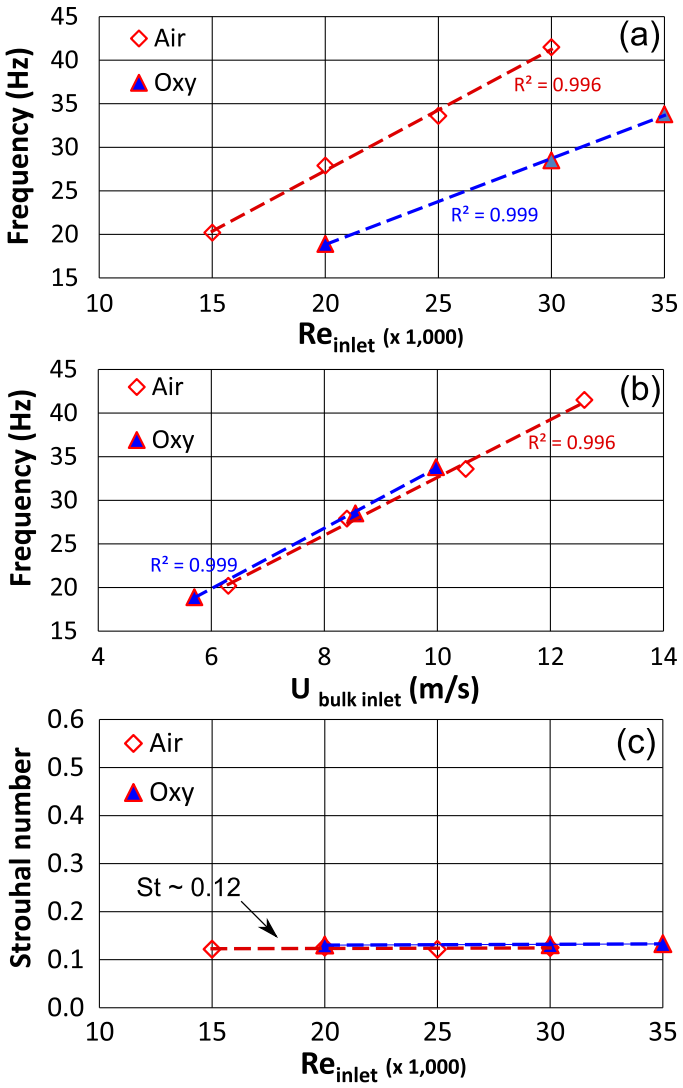


Figure 5-2: ORZ flame spinning frequency as a function of: (a) the inlet Reynolds number, (b) inlet bulk velocity. (c) Strouhal number St$=\frac{f_{ORZ}D}{U_{in}}$ dependence on the inlet Reynolds number. Linear least square fit lines are shown along with the corresponding $R^2$.

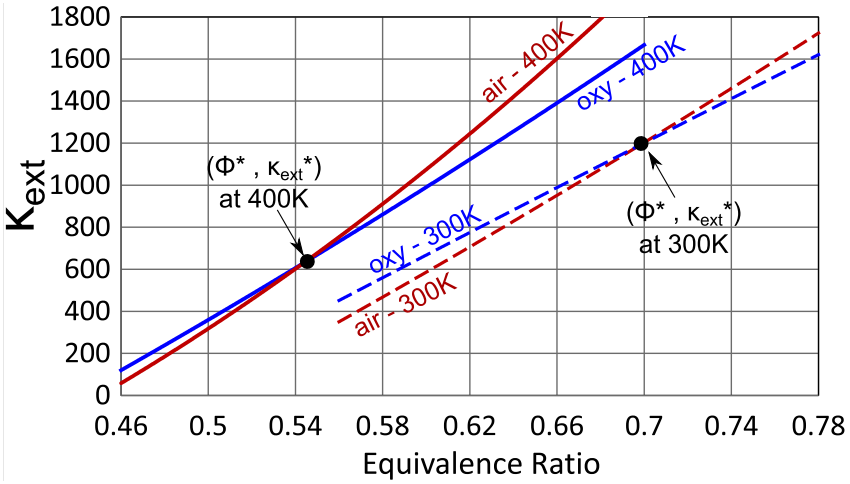


Figure 5-3: Calculated laminar extinction strain rates for air and oxy flames at a range of equivalence ratios. Blue lines correspond to air flames and red lines correspond to oxy flames. For each flame, a case at ambient temperature (300 K) and a case at 400 K is shown.

Now the question is : which flame property can be used to explain the trends we observe in Fig. 5-1-(b) ? Fig. 5-1 (see boxes) displays also the unstretched laminar burning velocity ($S_L^0$) and adiabatic flame temperature ($T_{ad}$) at the transition from oxy and air flames for $U_{in}$ = 4 m/s and $U_{in}$ = 8.4 m/s; at $U_{in}$ = 8.4 m/s for example, the oxy-flame has a $T_{ad}$=1700 K and $S_L^0$=8.2 cm/s when it transition from flame III to IV whereas the air-flame has a $T_{ad}$=1670 K and $S_L^0$=11.6 cm/s. Thus, none of these flame properties can be successfully used to explain this transition. In the next section, we will test the use of the extinction strain rate as a fundamental flame property to scale flame stabilization in the ORZ/OSL.

### 5.2.2 Flame III to IV Scaling

#### a - Extinction strain rate for Air vs. Oxy flames

Extinction strain rates are computed for air and oxy-flames as a function of the equivalence ratio, first, at an ambient temperature $T_0$ = 300 K which is the experimental

| | $U_{in}$ (m/s) | Re ($10^3$) | $\phi$ | $T_{ad}$ (K) | $T_{ORZ}$ (K) |
|---|---|---|---|---|---|
| **Air** | 8.4 | 20 | 0.59 | 1648 | 407 |
| **Oxy** | 8.4 | 29.5 | 0.59 | 1648 | 402 |

Table 5.1: Experimental ORZ temperature measurements comparing air vs oxy flames at different inlet velocities and Reynolds numbers. In the oxy-combustion cases is the mole fraction of $CO_2$ in the oxidizer $x_{CO2}$ is equal to 0.6434 to maintain the same $T_{ad}$.

inlet temperature of the combustor. Air and Oxy flame extinction strain rates increase with the equivalence ratio but at different rates; this leads to an equi-extinction strain rate $\kappa^*$ point at $\phi^* \approx 0.70$ where oxy and air flames are equally resistant to the strain rate (such a cross point was observed in previous studies [108]). At $\phi \leq \phi^*$, oxy flames have higher extinction strain rates than air flames and at $\phi \geq \phi^*$, oxy-flames become less resistant to strain. The existence of a cross point can be directly compared to the existence of an equi-transition point in Fig.5-1-(b); however, the experiment shows a lower equivalence ratio ($\phi \approx 0.56$) when both flames have the same behavior in terms of ORZ stabilization.

Computing $\kappa_{ext}$ at $T_0 = 300$ K does not necessarily match the thermal conditions in the ORZ. The inlet temperature is an important parameter that can affect differently properties of oxy-flames and air-flames. In order to compute more realistic extinction strain rates in the ORZ, the thermal conditions in that zone are needed. Temperature measurements in the ORZ are taken for that purpose. Steady state average temperatures of ORZ recirculating reactants, with $\phi$ just below ORZ flame appearance, are listed in Table 5.1. While the inlet temperature of the combustor is ambient, the average ORZ temperature, $T_{ORZ}$, is around 400 K with a small variation between air and oxy cases.

Figure-5-3 displays the extinction strain rates for air and oxy flames computed at $T_{ORZ} = 400$ K, closer to the experimental conditions in the ORZ. As expected, the

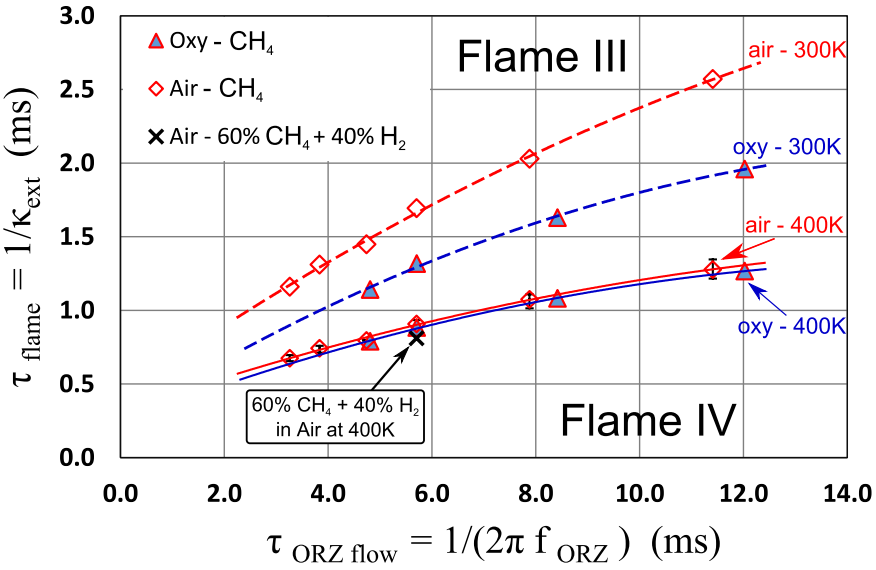


Figure 5-4: Characteristic flame time versus characteristic ORZ flow time for Oxy and air flames. Characteristic flame time computed at 300 K and 400 K. Quadratic least square fit lines are displayed.

extinction strain rate increases with the reactants temperature as it is raised from 300 to 400 K for both flames. However, the higher $T_{ORZ}$ has a weaker effect on the oxy-flame and the equi-extinction strain rate point ($\kappa^*$) still exists but shifts to lower equivalence ratio, from $\phi^*_{T_0} \approx 0.70$ to $\phi^*_{T_{ORZ}} \approx 0.54$-$0.55$.

### b - ORZ Flame Transition Scaling

We finally combine the previous results shown in Figs. 5-1-(b) and 5-3. The characteristic ORZ flow time changes are reflected by $1/2\pi f_{ORZ}$. For each imposed characteristic ORZ flow time, an equivalence ratio $\phi_{onset}$ is required for the transition to take place and $1/\kappa_{ext}$ is chosen as a characteristic flame time encapsulating chemical and thermo-physical effects. At each transition from Flame III to IV, the imposed characteristic flow time is plotted against the associated flame time scale computed at $T_{ORZ}$, i.e. closer to the actual ORZ reactants temperature before combustion starts to take place there. The result is displayed by Fig. 5-4: both air and oxy data collapse into a single

line that split the flow-flame time space into Flame III and Flame IV regions. This is not the case when the characteristic flame time is computed at $T_0$ = 300 K showing the importance of the importance of taking into account the preheating of the ORZ reactants in the model to collapse air and oxy data into a single correlation. Results for 60% $CH_4$ + 40% $H_2$ combustion in air at $U_{in}$=8.4 m/s are reproduced from [102] and plotted in Fig.5-4. At the same equivalence ratio, 60% $CH_4$ + 40% $H_2$/air mixture has a much larger unstretched laminar burning velocity compared to pure methane in air and the same flame temperature. Thus, this mixture has a very different thermo-chemistry when compared to Oxy-flame which has a much lower laminar burning velocity at the same equivalence ratio and adiabatic flame temperature. Despite this large difference (relatively fast chemistry for $CH_4$-$H_2$ combustion in air and slow chemistry for $CH_4$ oxy-flames) the mixtures collapse onto the same curve in the flame time - flow time space, further establishing the universality of the extinction strain rate choice as the relevant flame time scale that governs the flame stabilization in the ORZ in turbulent swirl combustion.

## 5.3 Chapter Conclusion and Next Step

In this chapter, we examined the effect of the diluent ($N_2$ vs. $CO_2$) on the onset of an ORZ flame in a lean premixed turbulent swirl-stabilized combustion system. We conclude the following:

1. There exists an experimental equi-transition point where the onset of flame stabilization in the ORZ takes place at the same equivalence ratio and inlet velocity in both air and oxy-combustion. The transition does not necessarily take place at the same adiabatic flame temperature and unstretched laminar burning velocity.

2. The ORZ flame spinning frequency is a purely kinematic phenomenon with a

Strouhal number independent the Reynolds number. This makes the inlet velocity a more relevant parameter to be fixed in order to maintain similar flow conditions in the ORZ and isolate thermo-chemical effects, when comparing air and oxy-combustion.

3. By defining the inverse of the ORZ spinning frequency as a characteristic flow time and the inverse of the extinction strain rate as a characteristic flame time scale, we demonstrated the existence of a single correlation, valid for both air and oxy combustion is found. In order to successfully scale air and oxy data, the extinction strain rate must be computed at a temperature that reflects realistic thermal conditions in the ORZ.

In this study, oxy and air flames were compared by adjusting the $CO_2$ mole fraction to obtain the same adiabatic flame temperature at the same equivalence ratio (lean burning). In practice, and because of the cost associated with $O_2$ separation, oxy-combustion would be preferably performed at stoichiometric conditions. An interesting idea for future work is to test and extend our ORZ flame model to these more practical conditions. The two previous chapters focused on the dynamics and physics underlying the ORZ flame transition. While investigating this transition, the microstructure of the flame stabilized along the ISL — unveiled by OH-PLIF data — suggested the presence of large scale flame wrinkling that appears to be due to vortical structures along the shear layer. In the final chapter of this thesis, we will investigate the origin and dynamics of these flame and flow structures.

# Chapter 6

# Flame-Vortex Interaction and Origin of Flame Structures

## 6.1 Introduction

Premixed flames in swirl-stabilized combustion devices take advantage of the low velocity regions created by these flows like shear layers and recirculation zones. The desired feature here is the aerodynamically created inner or central recirculation zone (IRZ), called also vortex breakdown (VB). While vortex breakdown helps stabilize a premixed flame, the same mechanism can be also detrimental because of the appearance of vortical structures. Whether coherent or not, these structures can interact with the flame and potentially lead to heat release disturbances. In this chapter, we will examine the existence of such structures in the reacting flows we have been investigating throughout this thesis.

### 6.1.1 Swirling Flow Structures and Dynamics

Two important groups of large scale structures exist in swirling flows:

**-1-** Vortical structure due to Kelvin-Helmholtz instabilities: the shear layers are zones of large velocity gradients that are inherently unstable following "the all-pervasive phenomenon of Kelvin-Helmholtz instabilities" [66]. As these KH instabilities develop, vorticity aggregates into well defined vortical structures; these roll-up and grow as they are convected downstream. In a non-swirling axisymmetric jet flow, Kelvin-Helmholtz instability gives rise to well-known vortex rings. The physical mechanism in swirling flows is similar and the combined axial-azimuthal shear layer would give rise to a helical vortex instead that winds around the shear layer; These instabilities were analytically studied by Gallaire et al. [22] but also examined experimentally in several studies [], as well as numerically using LES [36, 59]. In addition to the shear layer created at the interface between the incoming swirling jet and the vortex breakdown zone, often referred to as inner shear layer or ISL, an outer shear layer (OSL) often exist in swirling flow used in combustion. This OSL is formed owing to the use of a sudden expansion or a diffuser section between the burner and the main chamber (this is used in reacting swirling flows to stabilize the axial location of the stagnation point and the IRZ). The origin of the OSL is the boundary layer separation at the wall; it is also hydrodynamically unstable and leads to KH instabilities.

**-2-** Vortex Core: the vortical structures and instabilities mentioned above are shear driven; these are modified under swirling flows (compared to non-swirling jets) but not unique to them. A structure that is unique to swirling flows relates to the vortex core around which the flow swirls. Above certain conditions of swirl strength, this vortex core can develop self-sustained oscillations and bifurcate to a limit cycle following a

supercritical Hopf bifurcation [69]. In this oscillatory state, the center of the vortex core itself is in circular motion around the geometrical centerline in a precessing type motion. This is commonly known as the precessing vortex core (PVC). With such a PVC the entire flow becomes dominated by this azimuthal off-axis motion. This dynamics, unique to swirling flow, hasn't revealed yet all its mysteries and is still subject to investigation. There is no clear definition for the PVC but rather several descriptions of it; according to a description by Gicquel et al. [25], "*The PVC believed to be at the origin of such [azimuthal] oscillations coincides with a vorticity tube of helical shape located at the outer rim of the IRZ*". Another definition of the PVC by Wang et al.[107] states: "*it is found that the center of the IRZ is not often at the center of the circular pipe, but rotates about the axis of symmetry at a low frequency. This unsteady motion is usually called PVC.*". The above definitions both agree on the off-axis precessing motion of the PVC. But while the former describes a helical vortex winding around the IRZ, the latter merely defines the PVC by the off-axis motion of the IRZ. Thus, a more precise definition of the PVC is needed. In the current chapter, we will be talking about the helical vortex core (HVC) following the vocabulary used by Steinberg et al [96]; this HVC can potentially have a precessing motion (it would be a Precessing Helical Vortex Core, PHVC) as well if the whole structure's centerline rotates around the burner's centerline).

Heat release due to combustion has a profound effect on the PVC [31]. The precessing motion has been observed to be damped and eventually disappears when switching from a non-reacting to a reacting flow under some conditions; thermal expansion and subsequent density gradient as well as the strength of the backflow on the jet axis are the main parameters controlling the suppression of the PVC [71]. From linear stability analysis in a reacting flow[70], it was found that the temperature and density profiles at the combustor inlet or swirler centerbody are key in triggering this large scale az-

imuthal oscillatory motion; this has been used recently to explain why lifted flame are more often observed to be concomitant with the existence of precessing dynamics. The corollary of this is that when a flame attaches to a wall or a centerbody, it is expected to lead to a damping of the precessing motion.

### 6.1.2 Vortex Core vs. K-H Vortex

Syred and Beer [106] had already observed at the time that the PVC is usually situated on the boundary of the reverse flow zone. By having a conical , helical shape and being located at the edge of the recirculation zone (as described above in the definition given by Gicquel et al. [25]), the PVC appears to share common features with spiral vortical structures stemming from a Kelvin-Helmholtz instability of the inner shear layer. *Then, one important question is, how to differentiate between a helical vortex core that might also have a precessing motion from a helical vortex rolled up due to Kelvin-Helmholtz instabilities ?* A simple criteria often used to differentiate a vortex core from shear layer vortices is the following: the vorticity vector of the shear layer's K-H vortices should be perpendicular to the dominant shear flow whereas a vortex core in a confined swirling flow will be essentially in a streamwise direction; in a swirling flow inside a straight round tube with no vortex breakdown, one expect the vortex core to be aligned with the tube geometric centerline with a predominately axial vorticity,

However, the answer to the above question is not always straightforward; for example, in their LES efforts to identify coherent structures in turbulent swirling flows, Garcia-Villalba et al. [23] considered the inner spiral vortical structure appearing along the ISL and rolling up through a Kelvin-Helmholtz instability mechanism to be the PVC itself : "*the vortex axis is not parallel to the streamlines but orthogonal to them. This fact supports the interpretation that the precessing vortex core is generated by a shear layer instability, i.e., a Kelvin-Helmholtz instability, of the inner shear layer.*".

On the other hand, Lieuwen [57] warns against possible confusion and stresses the importance to differentiate "*the PVC from other helical shear flow structures that may also be present, such as those due to shear layer instabilities*". In the current work, one of our goals is to identify and track the origin of vortical structures observed in the experiments, hence it is important, throughout this process to be aware of similarities and differences between different types of helical structures in swirling flows.

### 6.1.3 Consequence of Flow Structures on the Combustion Process

Vortical structures and their dynamics play an important role in combustion systems. These structures, whether coherent or not, modulate the mixing processes between the fuel, air, and hot combustion products [37]. Moreover, these structures may interact with the flame and potentially wrinkle and stretch it. Depending on the sign of the stretch rate and the Lewis number (Le) of the fuel air mixtures, reactivity and the heat release rate can be enhanced (positive stretch with sub-unity Le) or reduced. The effect on heat release can also have the dramatic consequence of coupling with the acoustic field and potentially establish a positive feedback loop that leads to thermo-acoustic instabilities [73]. For the reasons mentioned above and owing to the relevance of swirling flows in modern premixed combustion systems, it is important to sustain the research effort to identify coherent structures, the way they may interact with premixed flames in such flow configurations and understand their origin.

## 6.2 Goal and Outline of the Current chapter

The goal of this work is to combine experimental and simulations in order to identify the origin and dynamics of flame and flow structures and their dynamics in a model turbu-

lent premixed gas turbine featuring a swirling flow. While doing that, we will keep our attention on some of the unclear points identified earlier in the introduction, namely: (1) similarity between coherent structures originating from a Kelvin-Helmholtz roll-up and the helical precessing vortex core; (2) the effect of combustion on "suppressing the PVC" and whether it is limited to the suppression of the off-axis precessing motion of the vortex core or it extends to modifying the entire vortex core ?

This chapter is organized as follows: first, we start with a description of the operating conditions we are focusing on in this chapter. Next, experimental results are described and evidence of large scale flow and flame structures and their dynamics are shown and analyzed (some of these were already observed in previous chapters). Finally, we rely on the validate LES code (see validation study in **chapter**-2) to track the origin of the vortical structures observed in the experiment. The simulation gives access to the entire three dimensional field and thus complements the detailed but mainly two dimensional optical diagnostics used in our investigation. This will allows us to unveil the vortical structures dynamics and interaction with the premixed reaction zone.

### 6.2.1 Operating Conditions

The two main cases studied experimentally and numerically in this chapter are a non-reacting flow at a Reynolds number (Re) of 20,000 and swirl number (S) of 0.7 (45 deg. angle) and a premixed $CH_4$-Air reacting case, with the same Re and S, at an equivalence ratio $\phi$=0.60; these two main cases are labeled as the non-reacting and the reacting cases. In both cases the inlet temperature is ambient and the pressure atmospheric. At $\phi$=0.60, a specific mode of flame stabilization is observed, which is the inner shear layer (ISL) flame. At these condition, we expect the flame to be in the reaction sheet (or thickened-wrinkled) regime as displayed by the turbulent combustion Borghi-Peters diagram in Fig.6-1. Owing to the presence of different zones in the swirling flow with

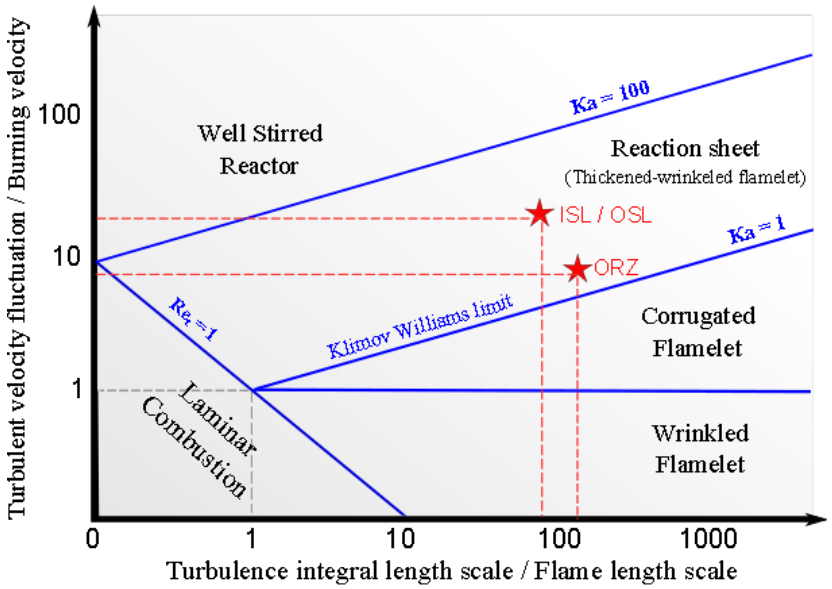


Figure 6-1: Borghi-Peters diagram for turbulent combustion regimes. The two red stars corresponds to the reacting flow case studied in this chapter (premixed $CH_4$-Air combustion, $\phi$=0.60, Re=20,000, $T_{inlet}$=298 K, atmospheric pressure); one for the flow conditions in the outer recirculation zone (ORZ) and one for the flow conditions in the inner and outer shear layers (ISL and OSL).

substantially different turbulent intensity, the outer recirculation zone (ORZ) flow and flows along the inner and outer shear layers are placed separately on the diagram. In the Borghi-Peters diagram displayed in Fig.6-1, the integral length scale used for the shear layers is the largest scale of flame wrinkles observed in OH-PLIF images (which will be shown later), whereas the integral length scale for the ORZ was considered equal to the step height.

Other flame stabilization modes (referred to as flame macrostructures) are observed for other equivalence ratios and these will be described later. Although the focus of this chapter will be on the non-reacting and reacting reference cases mentioned above, additional cases for different equivalence ratio or different Reynolds number will be used to support our discussion when needed.

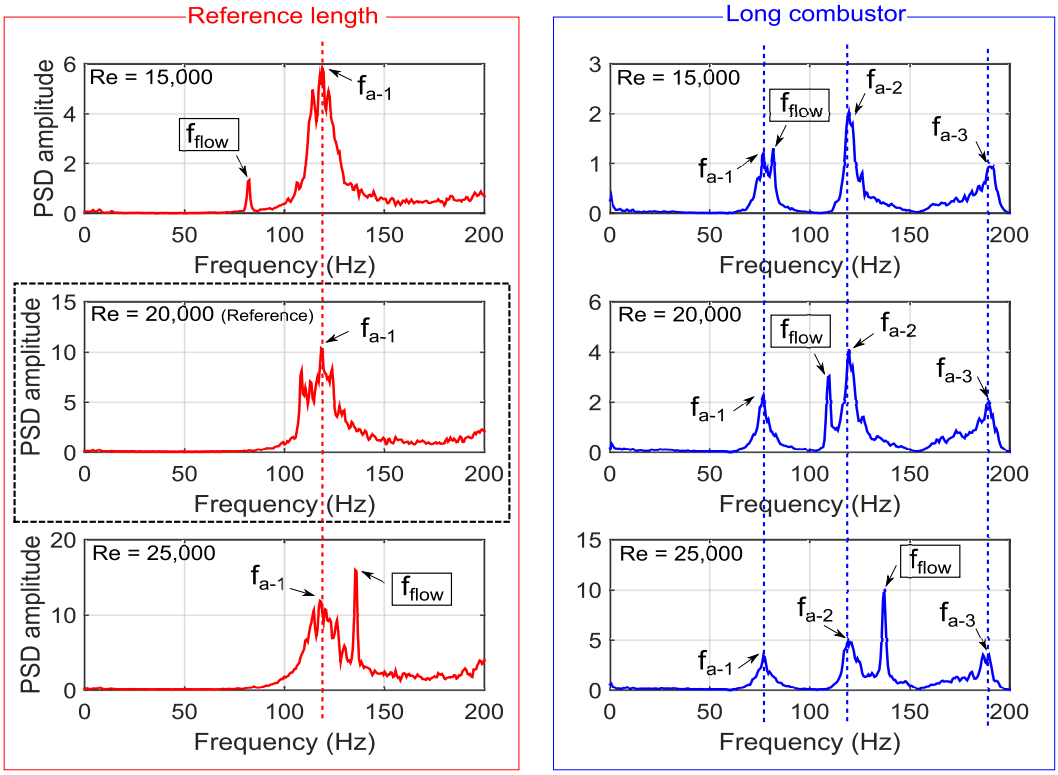


Figure 6-2: Power Spectral Density (PSD) of pressure recorded at the dump plane for non-reacting flows at different Reynolds numbers: reference length (left column) and longer chamber (right column). The reference inflow conditions are shown in the dotted box (Re=20,000 and reference length).

## 6.3 Experimental Results and Analysis

In this section, we present experimental results to unveil the dominant flame and flow dynamics in both the non-reacting and reacting cases at $\phi$=0.60. Before focusing on the two cases we are studying in this chapter (the non-reacting case and the reacting case at $\phi$=0.6), other flame shapes or macrostructures, obtained for different equivalence ratio (at same inflow conditions) will be briefly described.

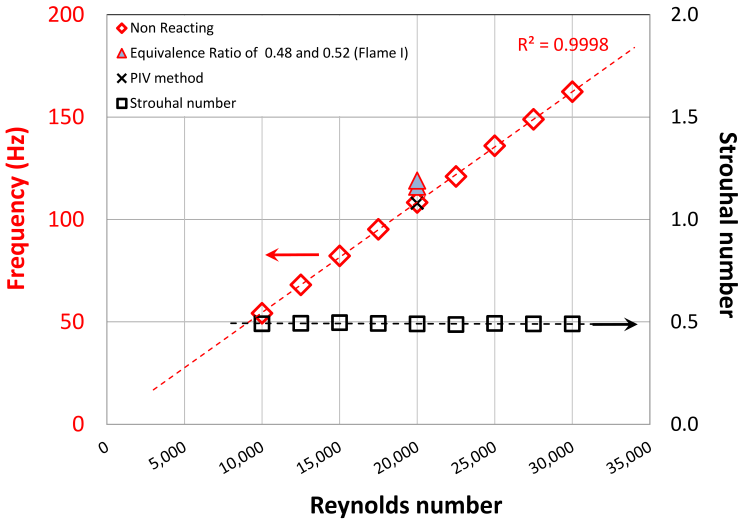


Figure 6-3: Pressure-extracted flow frequency and Strouhal number at different Re for non-reacting flow and reacting at low equivalence ratio (0.48 and 0.52 shown by triangles). For comparison, the PIV-extracted frequency for the

### 6.3.1 Large Scale Precessing Dynamics

#### Pressure-based Method

As a first step to uncover the dominant flow dynamics present in the swirling flow, the dynamic pressure is recorded at the location shown on the experimental setup schematic in Fig-2-1, i.e. between the swirler and the expansion plane. The recorded fluctuations would also include acoustic pressure fluctuations; from previous investigations using the same combustor geometry [101] the fundamental longitudinal acoustic mode is expected to be around 120 Hz. The power spectral density (PSD) amplitude of the pressure signal for the non-reacting flow is shown in Fig.6-2; the PSD amplitude at the reference inflow conditions (Re=20,000) and reference geometry is shown inside the dotted box of the left column of Fig.6-2. At these reference condition, the PSD shows a relatively large frequency band centered around 120 Hz, which is the expected fundamental frequency of the reference length combustor. Such an approach using only one pressure transducer does not differentiate between acoustic and aerodynamic

fluctuations; for this reason, we also recorded the pressure signal for different inflow conditions as well as for a different chamber length; by increasing the combustor's length downstream to four times the reference length (long combustor in the right column of Fig.6-2) and the Reynolds number (different rows in Fig.6-2), acoustic frequencies and the flow driven frequencies can be separately modified allowing for their identification. We see that when changing Re (plots on the left column of Fig.6-2) an additional peak appears around 80 Hz at Re=15,000 while the 120 Hz peak remains unchanged confirming its acoustic origin (the mean flow has a negligible impact on the acoustic frequency). By increasing the length of chamber, the acoustic frequency is modified while the frequency peak originating from the flow is unchanged. This method allows the extraction of aerodynamic-based frequencies for different Reynolds numbers even when these when these overlap with the natural acoustic pressure modes of the combustion chamber, which is the case here. At the reference conditions, a frequency $f_{flow}$=106 Hz is extracted. In Fig.6-3, this aerodynamic frequency ($f_{flow}$) is plotted against the Reynolds number, showing a linear dependence. This leads to a constant Strouhal number defined using the inlet (pre-swirler) bulk velocity and the inlet diameter ($St = \frac{f\ D_{in}}{U_{bulk}} \approx 0.49$). Using the same method, the frequency of the reacting case for flame I, at $\phi = 0.48$ and phi = 0.52, is extracted and plotted on the same graph (lean blowoff being at $\phi$=0.47). The dominant peak appears at a slightly higher frequency for $\phi = 0.48$ and phi = 0.52 : a 7% and 10% increase respectively compared to the non-reacting flow. However, pressure measurements at higher equivalence ratio for flame macrostructures for flame II, III and IV, did not exhibit a tonal spectrum around the frequencies showed above, besides the acoustic frequencies of the chamber. The coherent fluctuations show the existence of flow driven dynamics. However, spatio-temporal information on this motion cannot be extracted from simply measuring the pressure fluctuations.

**Flow-based method**

In order to better characterize the above dynamics, the flow field data acquired using PIV is analyzed. The instantaneous flow for the non-reacting flow is characterized by a large off-axis motion taking place at a precise frequency. In the reacting flows, this large scale motion is only observed for the columnar shaped flame observed from $\phi_{LBO}$=0.47 to $\phi = 0.54$ (Flame I). We analyze this motion using the following method : at a distance of $D_{in}/2$ from the expansion plane, the radial location of the axial velocity local maxima $M_{up}(t)$ and $M_{down}(t)$ are extracted. $M_{up}(t)$ and $M_{down}(t)$ are shown in Fig.6-4 (first row) plotted for the mean axial velocity profile for the non-reacting (left column of Fig.6-4) and reacting cases (right column of Fig.6-4). These two points are found to oscillate in time at $f_{jet} = 108$ Hz for the non-reacting case which is similar to the frequency extracted using the pressure-based method at the same flow conditions, as shown in Fig.6-3.

The phase delay between $M_{up}(t)$ and $M_{down}(t)$ show that the two maxima move in phase suggesting that the entire flow field is rotating around the combustor's centerline which is one of the main characteristic of the PVC, introduced earlier. The frequency of flow oscillation for flame I at $\phi$=0.51 is found at 117 Hz. The similarity between this frequency and the ones extracted above using the pressure-based method shows that the frequencies measured in Fig.6-3 are indeed flow driven frequency peaks and these are due to a large scale off-axis motion. When increasing the equivalence ratio beyond $\phi = 0.54$, this large scale dynamics disappears as soon as the flame macrostructures changes and the flame extends to the swirler centerbody located inside the burner tube; For $\phi \leq 0.55$ i.e. the equivalence ratio for which flame II appears (as we increase the equivalence ratio), there is only a weak and non-coherent motion of $M_{up}(t)$ and $M_{down}(t)$ as it can be seen in Fig-6-4 (right column). As noted in the introduction, the suppression of the PVC has been attributed to the attachment of flame to the centerbody and the related

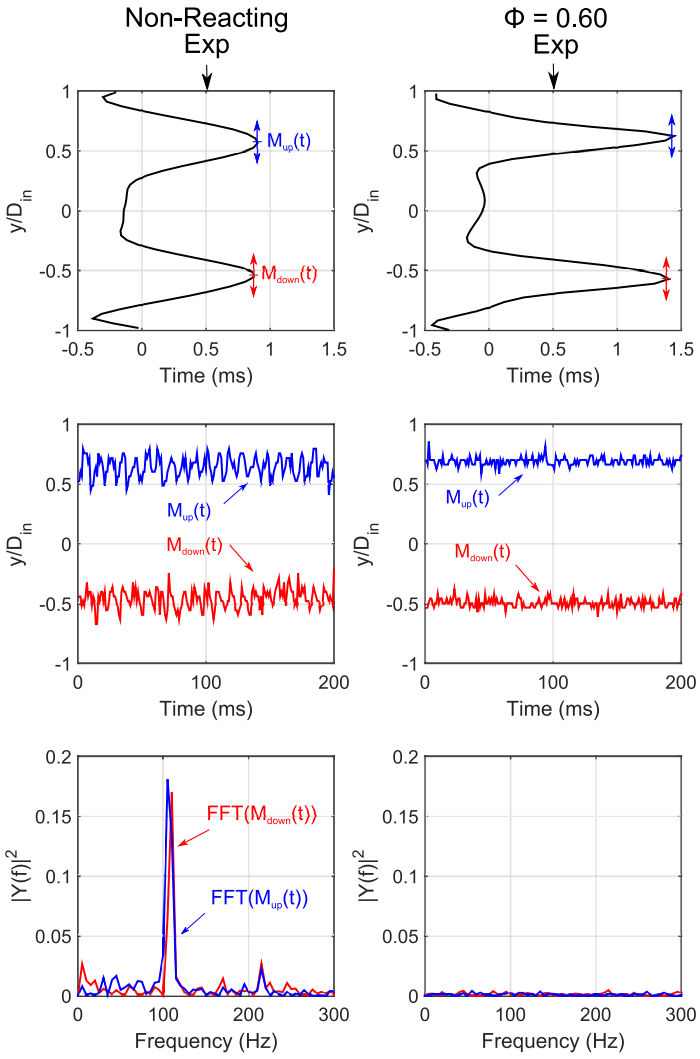


Figure 6-4: Dynamics of the incoming jet maxima (at x=$D_{in}/2$) for the non-reacting flow case (left column) and the reacting case at $\phi$=0.60 (right column) extracted from PIV data. The first row represents the mean velocity profile and location of maxima ($M_{up}$ and $M_{down}$). the second row shows $M_{up}$(t) and $M_{down}$(t) signals. The third row shows the FFT of $M_{up}$(t) and $M_{down}$(t).

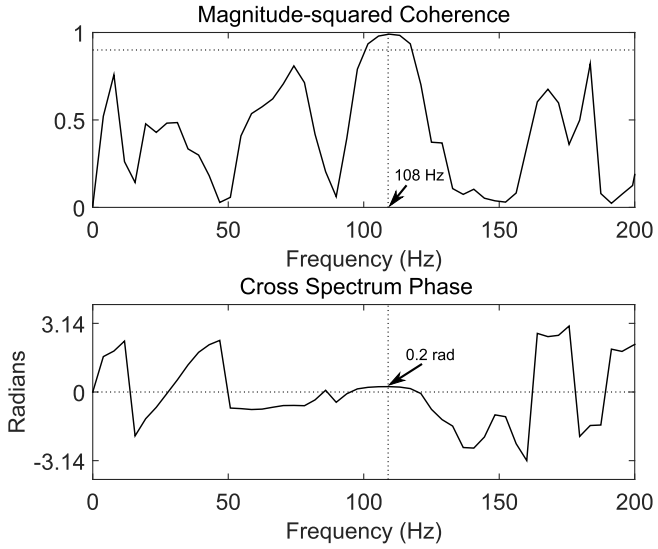


Figure 6-5: Phase between $M_{up}(t)$ and $M_{down}(t)$ for different frequencies showing in-phase oscillations at the frequency of 108 Hz.

change in the density ratio in the inlet region; our experimental results are consistent with that hypothesis.

### 6.3.2 Vortical Structures Along the Shear Layers

The precessing dynamics is only present in the non-reacting flow and very lean lifted flames (flame I) at the inflow conditions of interest in this chapter (S=0.7 and Re=20,000). For the ISL stabilized flame at $\phi$=0.60, this large scale motion of the entire flow field disappears; however, other flow and flame structures and dynamics are still observed. These are mainly vortical structures along the inner shear layer and in this section, we show experimental evidence for their existence. We will mainly rely on optical diagnostics (PLIF, PIV and chemiluminescence) as pressure measurements did not allow the identification of any large scale dynamics besides the natural acoustic frequencies of the chamber.

**OH-PLIF evidence:**

The ISL stabilized flame's micro-structure are now interrogated using OH-PLIF. A set of non-consecutive images from this data (taken at a 10 Hz repetition rate, not sufficient to resolve flow and flame dynamics) is shown in Fig.6-6. These images confirm the ISL stabilization of the instantaneous flame front. More importantly, we observe the flame to be wrinkled by what appears to be vortical structures as can be clearly seen in ($b_1$). In some instances as in ($b_1$) and ($b_2$), the flame large scale wrinkles are not aligned on the same axial position suggesting the presence of a spiral vortex similar to what was described in the introduction. In other instances, the flame is entrained by a large scale vortex as in ($a_1$) and ($a_2$); such structures are of the order of $\delta \approx 10$ - 12 mm i.e. one order of magnitude larger than the laminar flame thickness. Finally, in other cases as highlighted in ($c_1$) and ($c_2$), the flame has smaller structures with length scale of the order of the average flame thickeness that do not appear to have any spatial coherence. The observation of flame snapshots similar to the flame in ($b_1$) strongly suggests the existence of organized vortical structures. While it seems clear from their shape that these flame wrinkles are due to the flow structure in the shear layer, their origin is less straightforward.

**PIV evidence:**

PIV measurements are performed to confirm the existence of vortical structures along the inner shear layer conjectured above. In Fig.6-7, the instanteneous planar velocity streamlines (smaller field of view focused on half chamber width) at 3 consecutive times are displayed, with 1 ms separating each snapshot. A vortex can be observed at the first time step and tracked in time along the shear layer. It is likely that these vortices are the ones responsible for large scale wrinkling of the flame observed in Fig.6-6-(a). Different methods to analyze the spectral content of such structures were performed. Probing

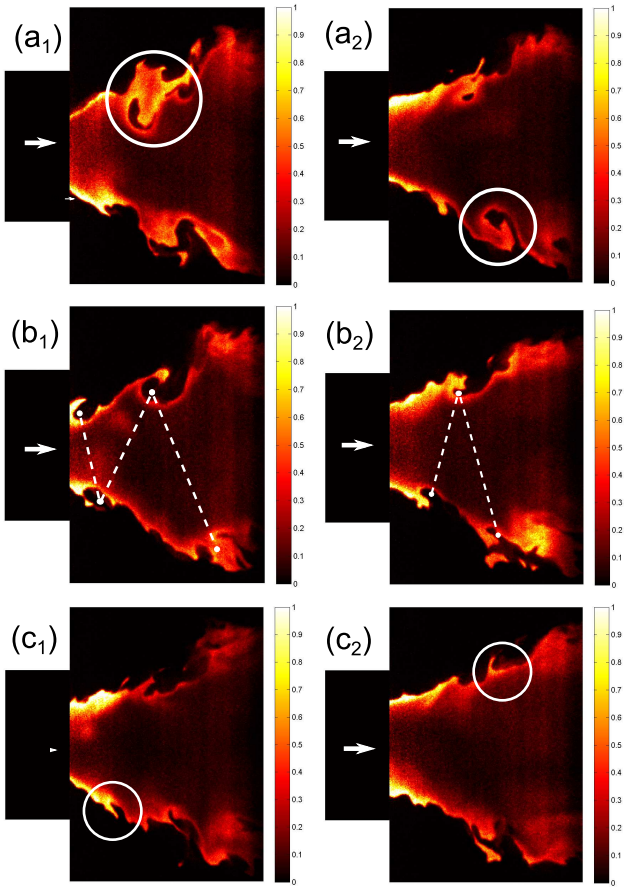


Figure 6-6: Non-consecutive OH-PLIF images of ISL flame for $CH_4$/air at $\phi$=0.60

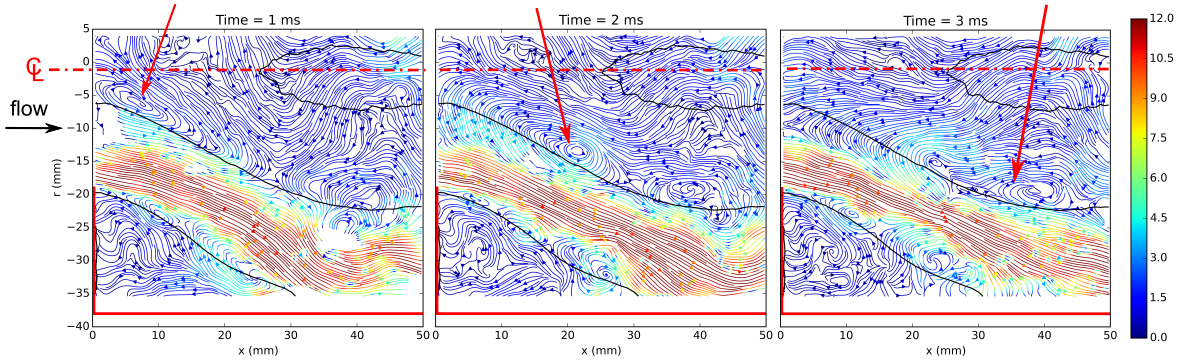


Figure 6-7: Consecutive streamline plots colored by x-r velocity magnitude (colored by the sign of axial velocity) at $\phi$=0.60. Solid black line corresponds to the mean zero velocity contour. Solid red border corresponds to the chamber wall. Dotted red line shows the chamber's centerline.

the velocity field along the ISL did not allow us to extract any frequency associated with this shear layer dynamics. A Proper Orthogonal Decomposition (POD) of the flow field is also performed in order to extract the most energetic coherent structures in the flow.

**POD analysis** POD is used to confirm previous results and shed additional light on the dynamics shown earlier. POD results for the non-reacting (Fig.6-8) and reacting (Fig.6-9) cases are compared; these include the kinetic energy ranking of the different modes and the extraction of the four most energetic modes. The first most energetic POD mode is expected to be the mean velocity field; this is confirmed as it can be seen in Fig6-8 (b) and (c) and Fig6-9 (b) and (c). In the non-reacting case, 59% of the energy is captured by the first "mean" mode. Modes 2 and 3 hold jointly 10% of the energy. the energy per mode for m>3, becomes negligible and no coherence has been found in these. Modes 2 and 3 reflect the coherent precessing previously highlighted taking place at 108 Hz. The location of the energetically dominant vortical structures appear in Fig6-8 (e) and (g). In contrast to the non-reacting flow, the reacting POD analysis shows that the mean flow holds 78% of the kinetic energy; the higher modes 2, 3 and 4 have respectively 1.4%, 1.1% and 0.8% of the energy with no apparent coherence as can be seen from the power spectral amplitude shown in (f) and (h). In this case, the flow is dominated instead by a low frequency motion taking place at 7 Hz (see (d)). Previous analysis showed that this frequency is likely due to a pulsation of the IRZ that is cyclically filled and emptied with combustion products.

**Chemiluminescence evidence:**

Flame chemiluminscence images suffer from the limitation of being line of sight data, but in the current context of extracting flow and flame dynamics these can be useful

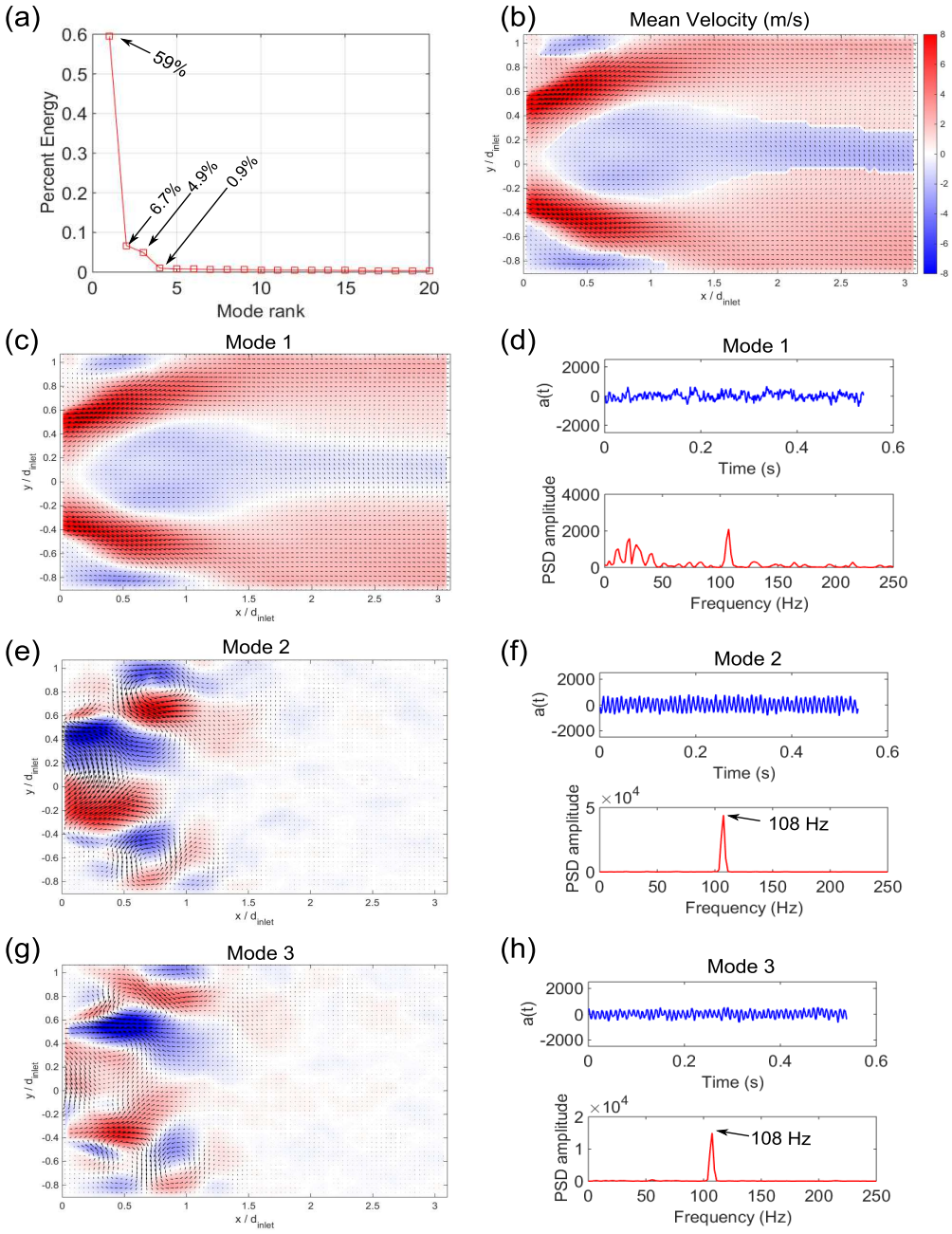


Figure 6-8: POD results for the non-reacting flow: (a) rank of modes eigenvalues showing kinetic energy distribution. (b) mean velocity contours. Three most energetic modes: mode 1 (c and d), mode 2 (e and f), mode 3 (g and h). (c, e and g): mode reconstruction; (d, f and h): temporal mode variation and FFT of the temporal component of each mode. The percentage weight of the 4 most energetic modes are displayed in (a).

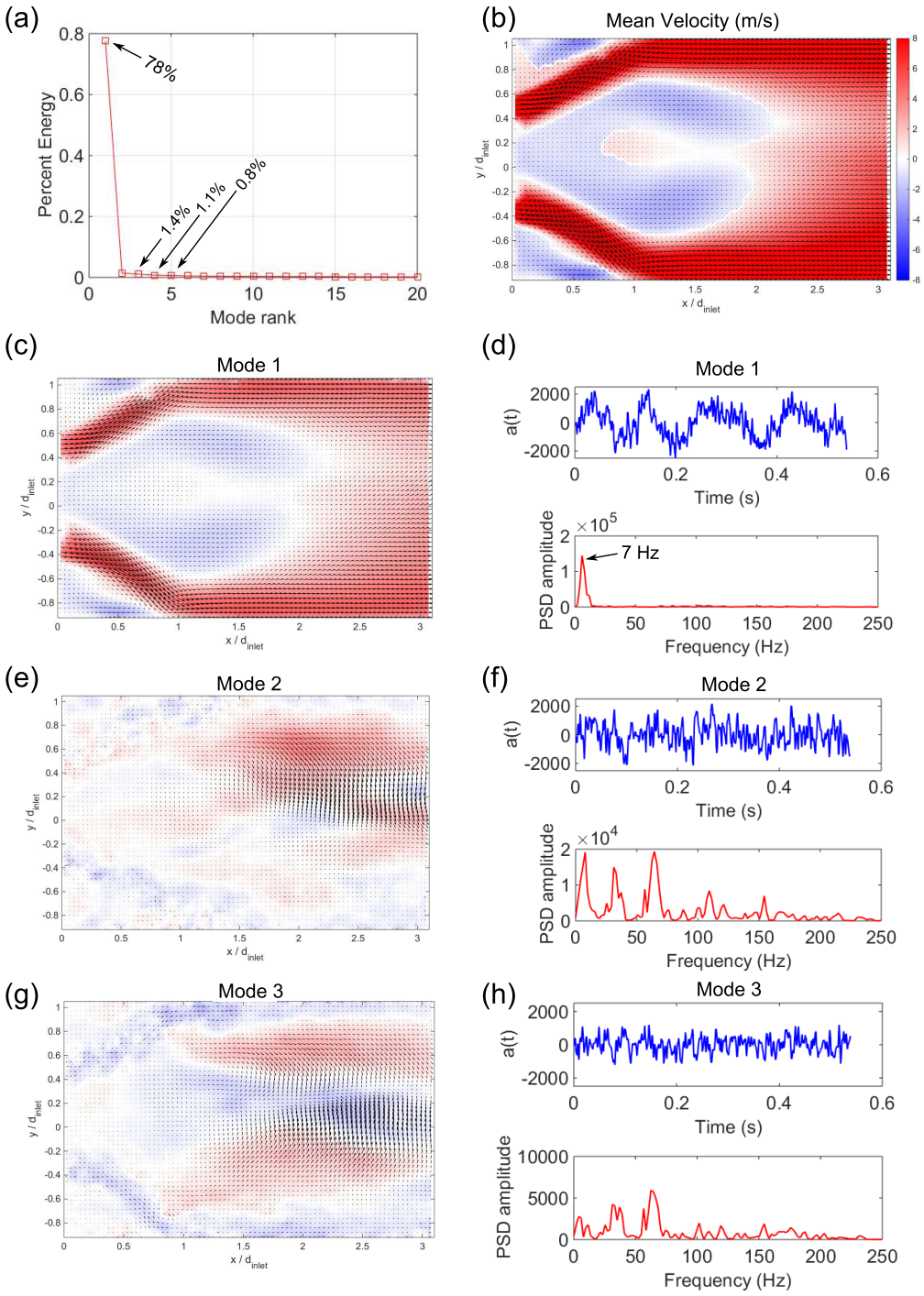


Figure 6-9: POD results for the reacting flow $\phi$=0.60: (a) rank of modes eigenvalues showing kinetic energy distribution across modes. (b) mean velocity contours. Three most energetic modes: mode 1 (c and d), mode 2 (e and f), mode 3 (g and h). (c, e and g): mode reconstruction; (d, temporal mode variation and FFT of the temporal component of each mode. The percentage weight of the 4 most energetic modes are displayed in (a).

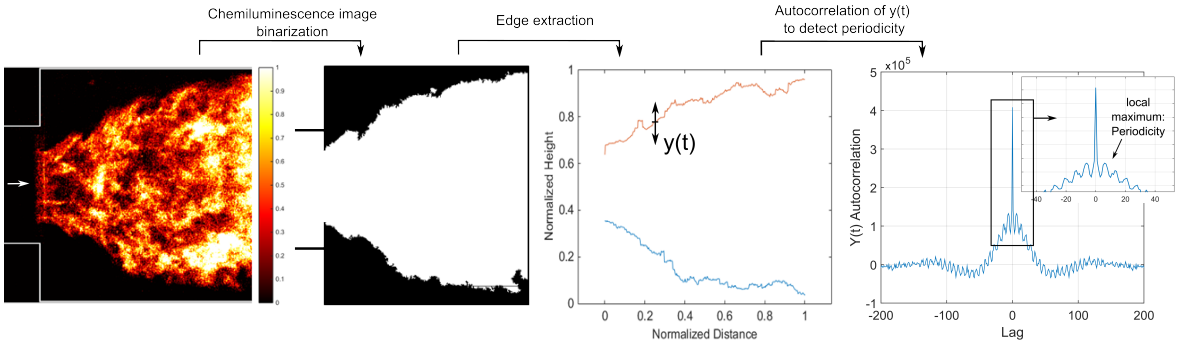


Figure 6-10: Procedure for dynamics extraction from flame chemiluminescence images.

and effective. Flame images are taken using an IR-filter at 1000 Hz and an analysis procedure is performed following the schematic in Fig.6-10. The different flame snapshots are binarized and the flame edge extracted. Along the flame front (or more accurately here the flame brush), the radial position Y(t) of the flame is recorded and the auto-correlation function of Y(t) computed. The autocorrelation function is shown in Fig. 6-10: a local maxima appears at a certain values of the lag which hints to the presence of a periodic motion; in the reference case of Re=20,000 and swirl angle of 45 deg. the lag value of the first local maxima is L = 6.5 and L = 115 leading to a frequency of f = $\frac{f_{sampling}}{Lag}$ $\approx$ 150 Hz and f = 8 Hz, respectively. The low frequency is similar to the one previously extracted using POD; again, this frequency is likely associated with the pulsation of the entire IRZ due to cyclical filling and emptying.

In order to better characterize this frequency and its dependence on the flow, the same analysis is performed for different values of Re from 15,000 to 30,000. The results are shown in Fig.6-11. The coherent radial motion of the flame position does not exhibit a dependence to the Reynolds number which is counter-intuitive for dynamics with hydrodynamic origin that usually scales with the inlet velocity. A different swirl angle (60 deg.) is used and the ISL flame frequency extracted again following the same procedure described in Fig.6-10. In this case, the autocorrelation function led to a dominant frequency that increases linearly with the Reynolds number which is the

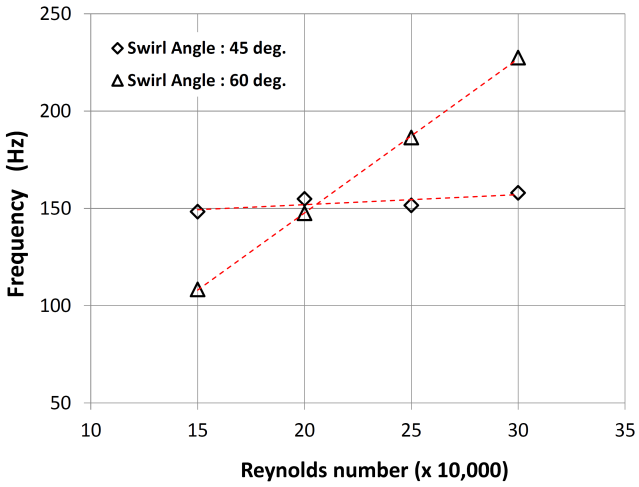


Figure 6-11: Frequency of oscillation of ISL vortices extracted following procedure in Fig.6-10 for different swirlers (Reference case swirler: 45 deg.) and Reynolds numbers.

expected behavior. A possible explanation for the independence of the frequency in the reference case of 45 deg. angle swirler is the potential lock-on of the ISL vortices motion to the fundamental longitudinal acoustic mode's frequency of the chamber.

## 6.4 LES Results

The experimental approach undertaken above allowed to clearly identify the precessing dynamics; however, it only suggested the existence of vortical structures along the shear layer without full characterization (frequency, shape...). Now we rely on LES to continue the examination of vortical structures along the ISL and most importantly their origin. The first step is to determine whether the large scale precessing dynamics shown experimentally in the non-reacting flow, as well as its absence at larger equivalence ratio can also be demonstrated in the simulation.

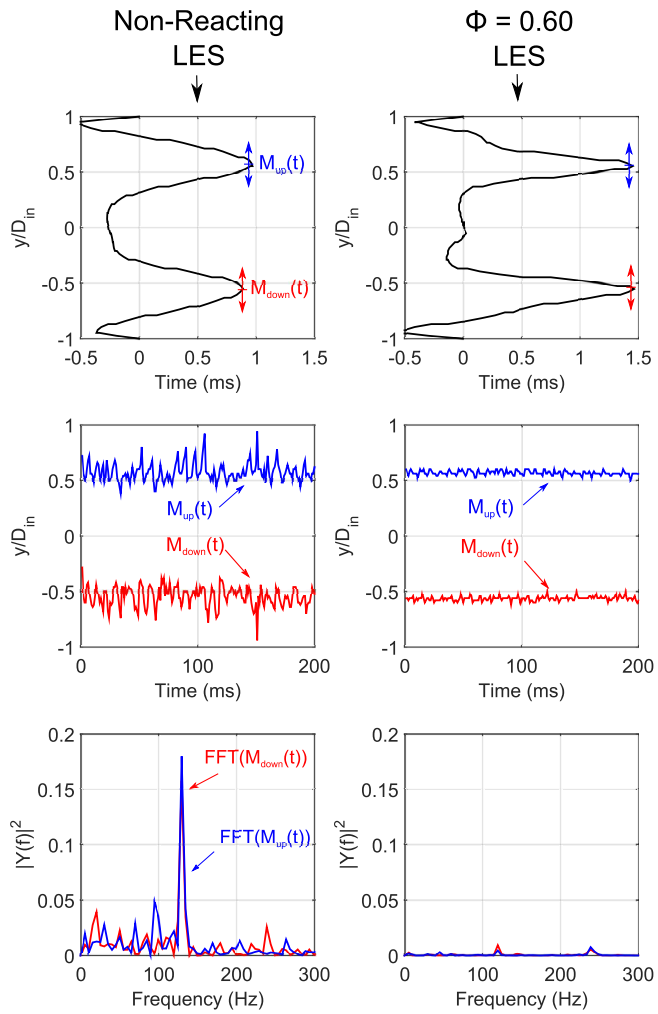


Figure 6-12: Dynamics of the incoming jet maxima (at x=$D_{in}/2$) for non-reacting flow case (left column) and reacting case (right column) extracted from LES (to be compared to Fig.6-4). The first row represents the mean velocity profile and location of maxima ($M_{up}$ and $M_{down}$). the second row shows $M_{up}$(t) and $M_{down}$(t) signals. The third row shows the FFT of $M_{up}$(t) and $M_{down}$(t).

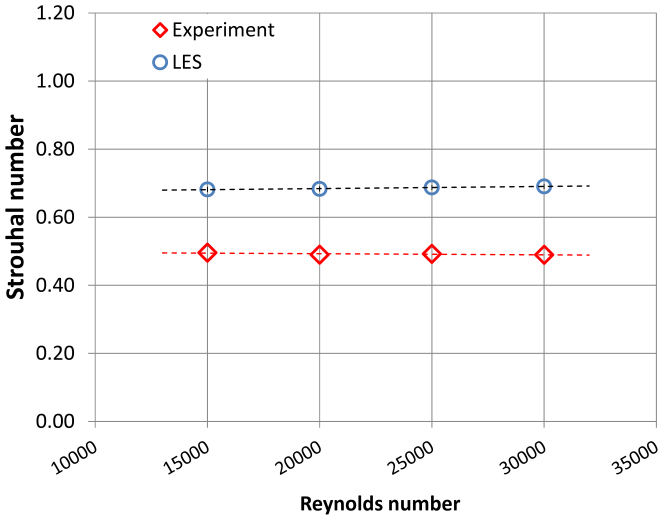


Figure 6-13: LES vs. Experimental precessing frequency for the non-reacting flow case (frequency extracted using the velocity method for LES and pressure method for the experimental data)

### 6.4.1 Precessing motion

The simulated non-reacting swirling flow case at the reference conditions does exhibit large scale precessing motion. A corresponding plot to Fig.6-4, which illustrated the precessing motion from experimental data, but now obtained using the simulation results is shown in Fig.6-12; the radial locations of the two velocity maxima oscillate in-phase like in the experiment. The oscillation takes place at a frequency of 149 Hz; this frequency is to be compared with the experimental precessing frequency of 108 Hz. When simulating the reacting case, the flame stabilizes along the inner shear layer and extends to the swirler centerbody which is visually seen. However, similar to the experiment the precessing motion is damped and only a very weak peak at 150 Hz can be seen. The precessing motion was previously shown to scale with the Reynolds number and to lead to a constant Strouhal number (Fig-6-3). The same behavior is captured by the simulation as shown in Fig.6-13. However, some discrepancy can be seen in the frequency itself which is one of the improvement that will be made in

future work. Large eddy simulations lead to a constant Strouhal number at $\mathrm{St}_{LES} = 0.68$, higher than the experimental value $\mathrm{St}_{exp} = 0.49$. In the current analysis, this is considered acceptable since the scaling with the inflow conditions, i.e. different Re's, is well captured.

### 6.4.2 Flame Wrinkling and the Helical Vortex

The flame wrinkling that was observed experimentally is now numerically investigated. Although the three dimensional field is available in simulations, we start by emulating the experimental 2D field of view. Longitudinal cross sections of the domain are considered and the azimuthal vorticity is plotted along with the flame contour. The result is shown in Fig.6-14. In the upper ISL, we can see a clockwise vortex present (located by the vertical dashed line). This vortex entrains the flame front in its motion and wraps it around. 1 ms and 2 ms later, a vortex appears slightly downstream wrinkling the flame as well. These vortices can be tracked in time and 2D-space; a vortex in the same upper ISL would appear again at approximately the same location every 6-7 ms i.e. with frequency around 154 Hz. These results show that the simulation predicts vortical structures along the ISL and these are indeed able to wrinkle the flame as observed in the experiment. Moreover the vortices in the upper ISL appear to be not aligned with the lower ISL vortices following a "zig-zag" pattern.

We now extract the flow's vortex cores using the Lambda-2 detection algorithm [40]. The results are plotted in Fig.6-15; we see that the vortices are in fact 2D cuts of the helical vortex extending to the swirler centerbody. Similar helical vortex cores can be observed for both the reacting and non-reacting flow. In the reacting flow case the vortex core is mostly aligned with the combustor centerline as it gets closer to the swirler centerbody. As we move downstream the vortex core deviates from the geometrical centerline and starts winding around in the helical motion. Vorticity

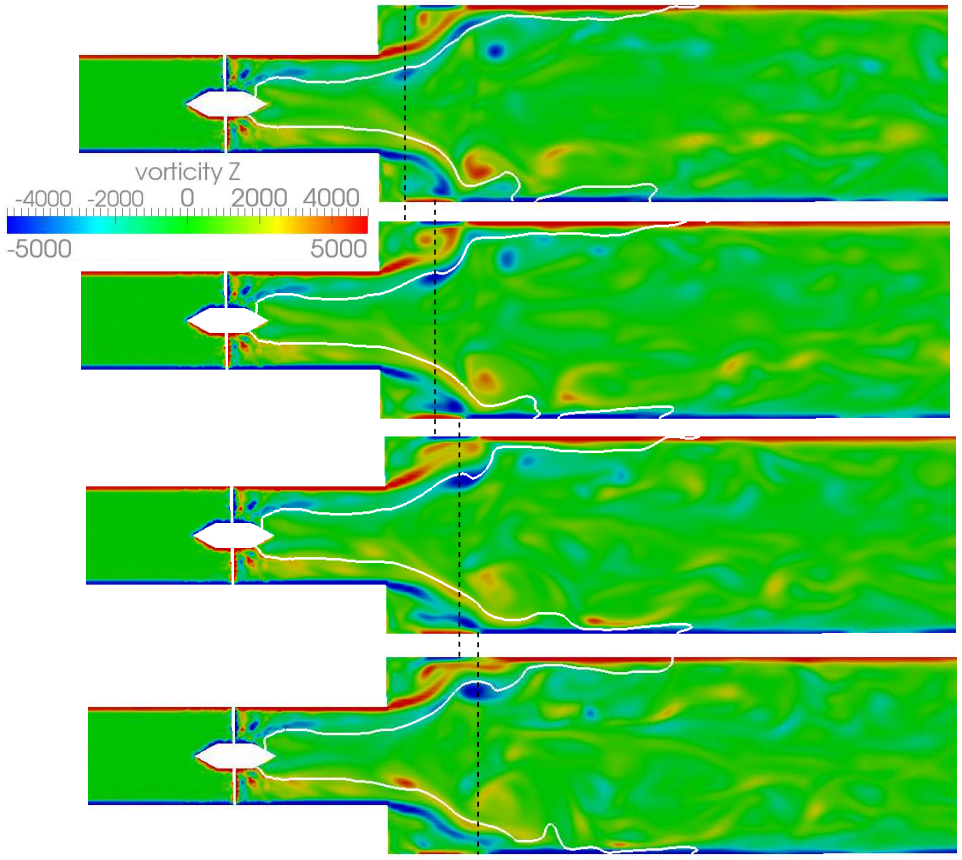


Figure 6-14: LES of reacting case $\phi$=0.60 featuring the out of plane vorticity as well as the progress variable contour c=0.8 (white line) as a way to locate the flame front. 1 ms separates consecutive frames.

transitions from being predominately streamwise to predominately tangential. The streamwise vorticity portion inside the inlet tube have a weak off-axis motion and the HVC dynamics is mainly a cork screw like motion around the centerline where the axis of the cork screw remains close to the geometrical centerline. This motion means that the convection of vortices downstream, as seen in Fig.6-14, is only an illusion due to the 2D cut; a vortex will appear at the same location on the interrogated plane when the helix performs an entire revolution around the combustor's centerline.

The non-reacting flow is characterized by a similar HVC but with more complex dynamics. In addition to the rotation observed for the reacting flow, the non-reacting

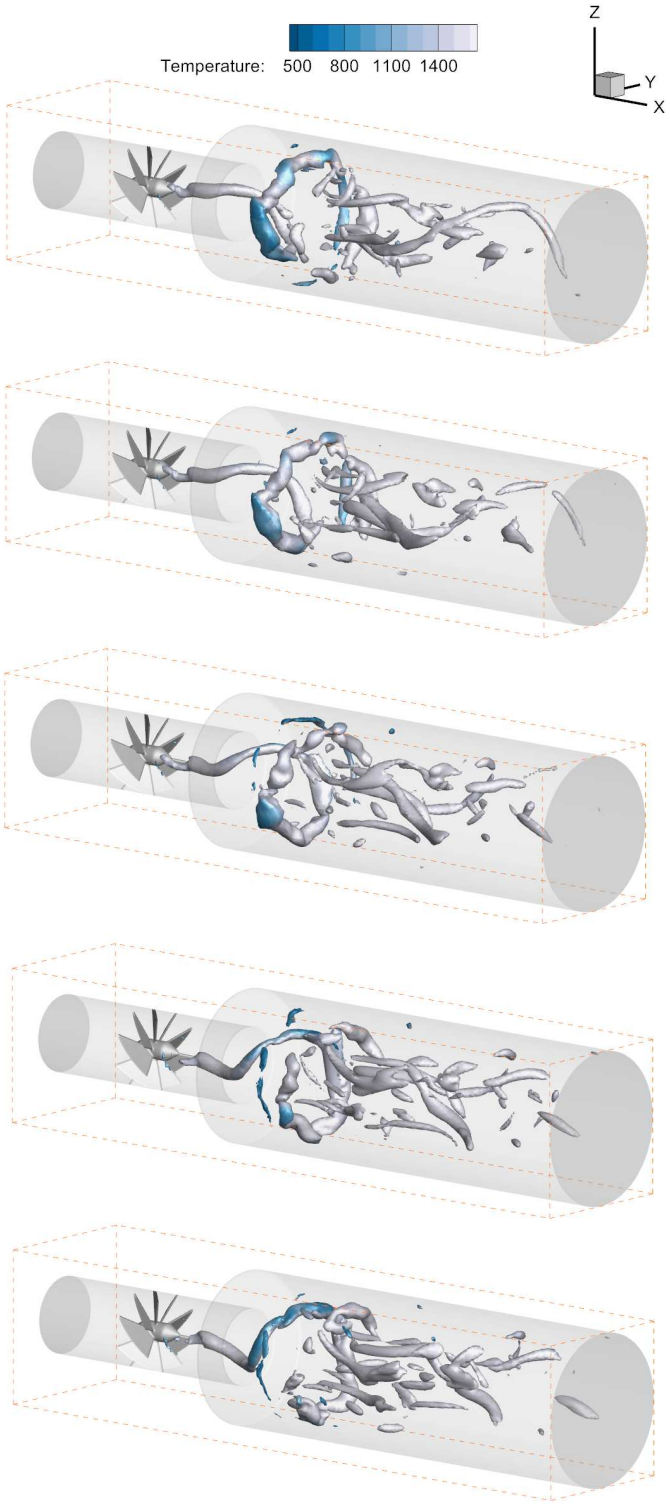


Figure 6-15: Three-dimensional vortex core identification using the Lambda-2 criterion (here colored by temperature) showing the helical vortex core for the reacting case with a time interval of 1 ms between each image.

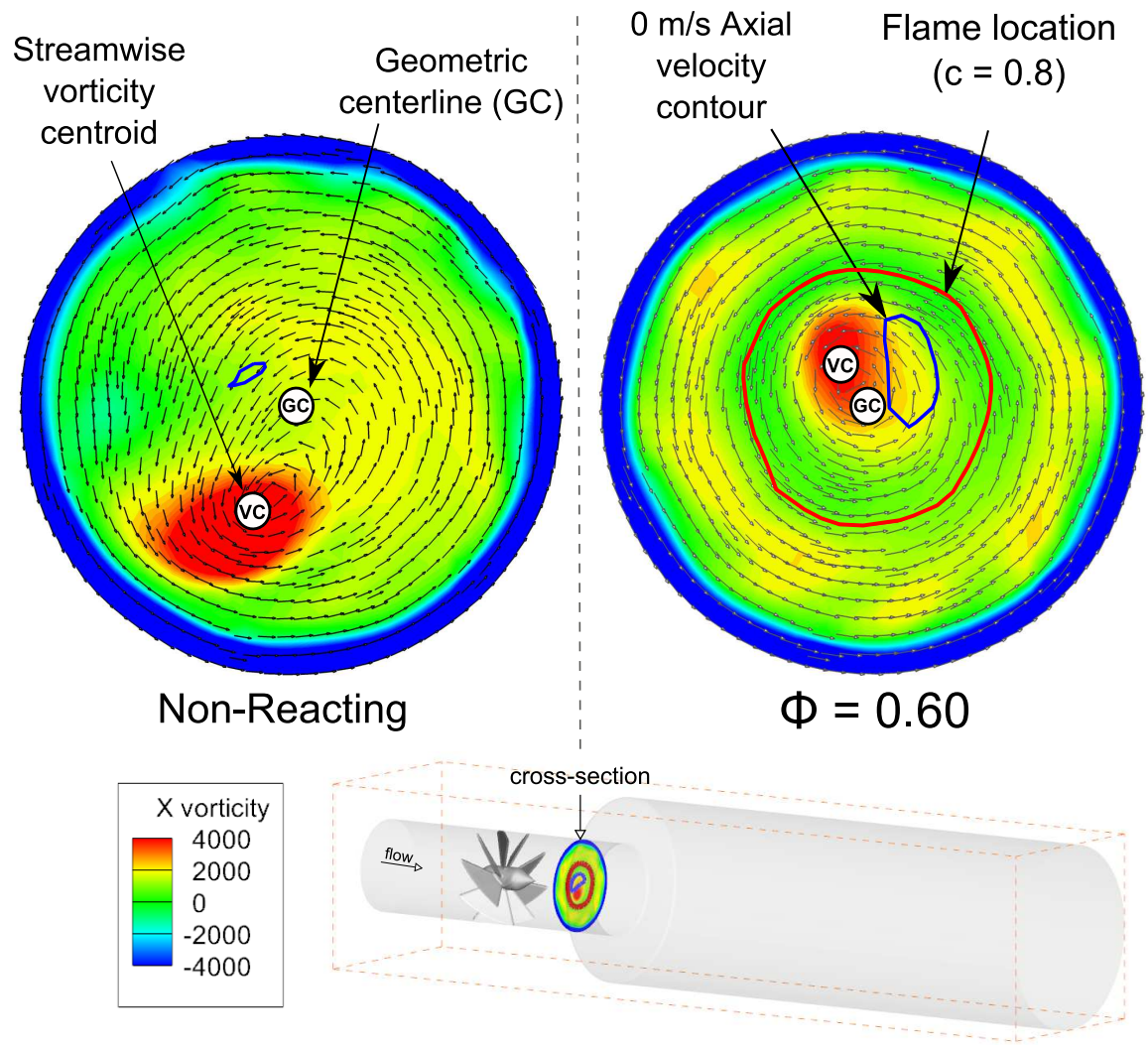


Figure 6-16: Superposition of LES streamwise vorticity, velocity field, zero axial velocity contours and the flame (progress variable c=0.8) showing the location of the vortex core relatively to the centerline, the negative axial velocity region and the flame. Slice location: x = $D_{in}$ from the swirler, inside the inlet tube. Left column: non-reacting flow. Right column: reacting flow.

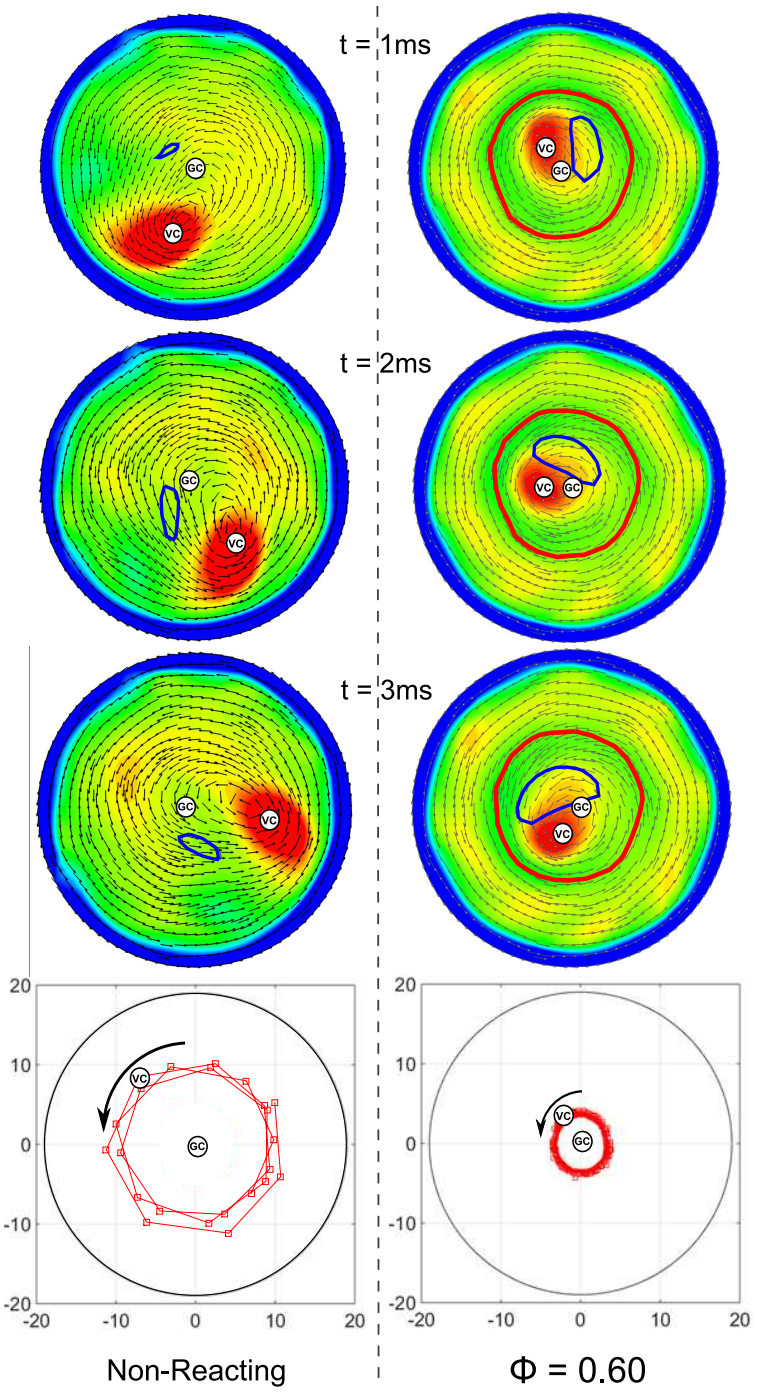


Figure 6-17: Superposition of LES streamwise vorticity, velocity field, zero axial velocity contours and the flame (progress variable c=0.8) showing the location of the vortex core relatively to the centerline, the negative axial velocity region and the flame. Slice location: x = $D_{in}$ from the swirler, inside the inlet tube. Left column: non-reacting flow. Right column: reacting flow. Time between snapshots : 1 ms. Bottom row: trajectory of the vortex core over time.

HVC has an off-axis motion of the vortex core around the geometric centerline entraining the entire flow in such a precessing motion; the inlet tube portion of the VC does not remain close to the centerline but rotates around it. Fig.6-16 and Fig.6-17 illustrate this important difference between the reacting flow and the non-reacting one: for the non-reacting flow (left column), the vortex core is closer to the wall than to the centerline. The precessing radius is shown in the bottom row of Fig.6-17. In the reacting case (right column), the precessing radius is smaller. The streamwise vorticity showing the location of the vortex core is inside the flame tube. It is also adjacent to the negative velocity region illustrated in the figure by the zero axial velocity contour; both the negative velocity region and the vortex core are in a circular motion around the geometric centerline.

The vortex core extends to the swirler centerbody close the centerline and deviates only slightly from it in the reacting case; the vortex core also appears inside the flame tube away from the shear layer where the flame stabilizes, as illustrated by the snapshot in Fig.6-18(b). This shows that the vortical structures is not caused by shear layer instability but rather a helical instability of the swirling flow (discussed in the introduction of this chapter). Moreover, the Helical vortex core is inside the high temperature product zone; the dilatation effect of heat release is a vorticity sink mechanism and is likely responsible for the lower rotation radius of the vortex core around the geometric centerline (precessing). As we move downstream of the centerbody, the core moves away from the centerline and acquires a cone-spiral shape. The core gets closer to the vortex breakdown's inner shear layer where the flame is stabilized and starts interacting with the flame, ultimately wrapping it in a helical roll-up as illustrated by Fig.6-19. In this figure, the flame contour is shown along with the position of the HVC. Further downstream, the HVC breaks into smaller structures contributing to turbulence.

Finally, outer shear layer instabilities (Kelvin-Helmholtz) are likely present in this

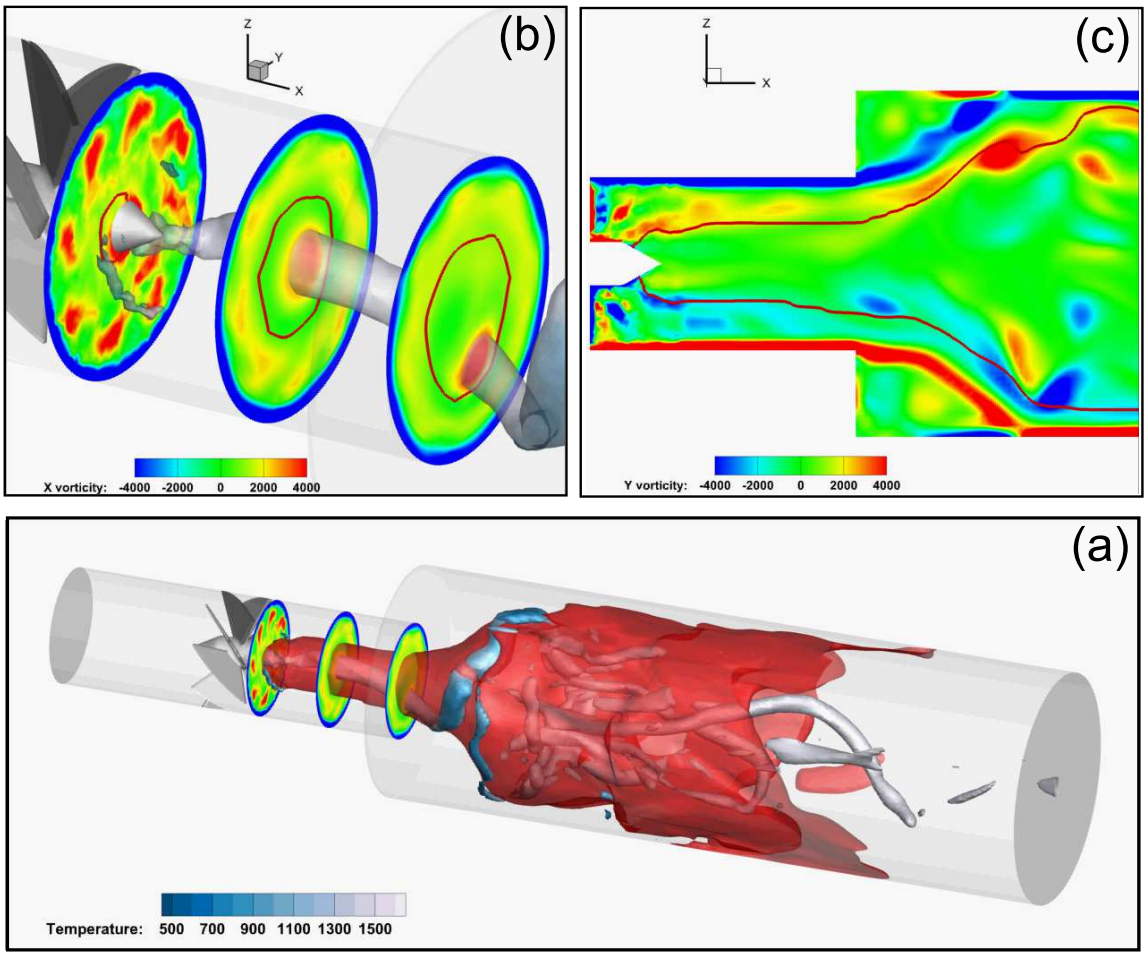


Figure 6-18: (a) Instantaneous flame contour (progress variable c=0.8) for the reacting case ($\phi$=0.60) with Helical Vortex Core identified using lambda-2 criterion. (b) zoom on the region between the swirler and the sudden expansion showing the vortex core originating from the swirler centerbody and remaining aligned with the geometrical centerline and inside the flame tube. Cross-sections show axial vorticity contours. (c) Azimuthal vorticity contours and instantaneous flame contour (progress variable c=0.8) showing the flame roll-up by the helical vortex core when it reaches the inner shear layer.

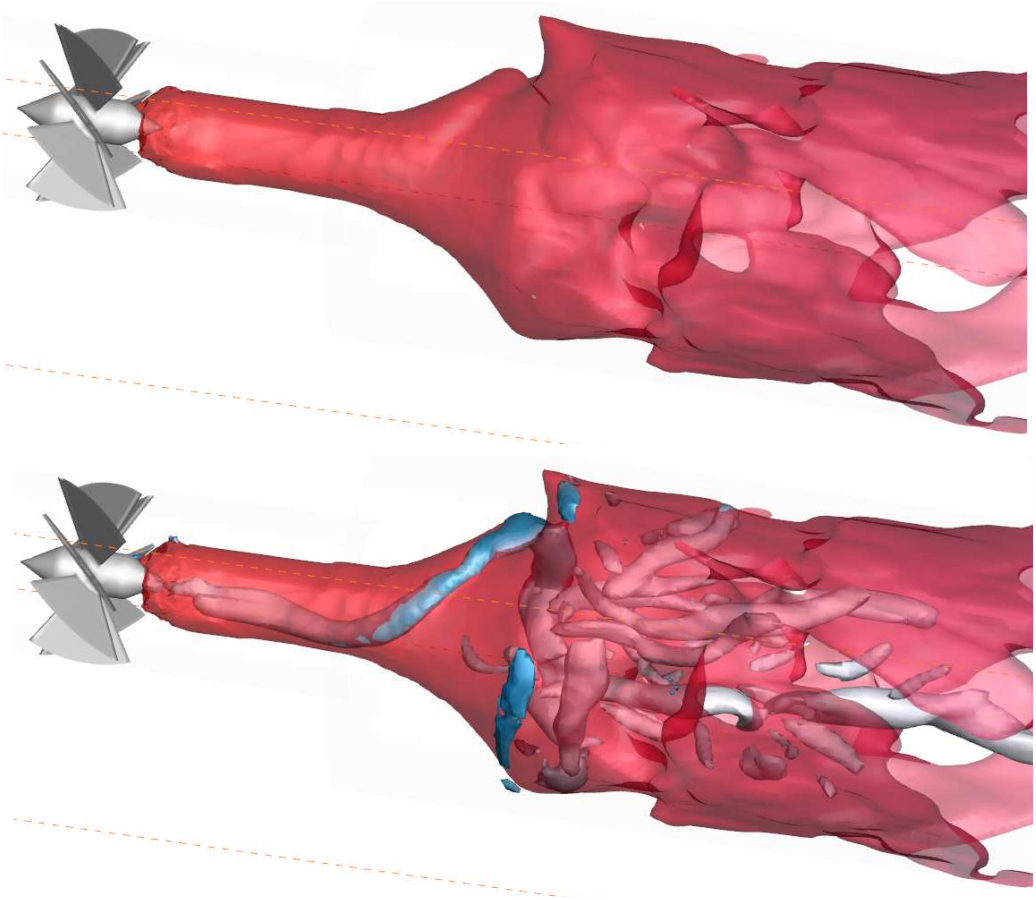

Figure 6-19: Instantaneous flame contour for the reacting case ($\phi$=0.60): (top) without Helical Vortex Core showing a helical roll-up of the flame, and (bottom) with Helical Vortex Core showing the location of the vortex with respect to the flame. Helical Vortex Core identified using lambda-2 criterion.

reacting flow but are of a smaller scale and strength compared the helical vortex core highlighted here. For this reason, large eddy simulations performed with a grid/filter of the order of the 1 mm did not resolve these vortical structures. The interaction between the inner and outer shear layer through the interaction between the vortical structures along these shear layers is potentially the reason behind a flame kernel detaching from the ISL and reaching the ORZ (mechanism of flame transition to the ORZ highlighted in **chapter**-4). Finer LES grid/filter simulations would be needed to confirm this hypothesis.

## 6.5 Chapter Conclusion

In this study, we investigated important swirling flow and flame dynamics and its impact on the premixed flame. We relied on a combination of experimental (PIV, OH-PLIF) and numerical (LES) tools to unveil complex dynamics. A parallel goal was to also validate the LES code and identify areas of improvement. We reached the following conclusions:

1. The precessing dynamics is present for the non-reacting flow and lifted columnar flames; it is largely damped for the ISL stabilized flame. Both experimental results and LES capture this behavior. The suppression of the off-axis motion is concomitant with the change in vortex breakdown type and also the flame attachment to the swirler centerbody, consistent with observations in the literature.

2. A helical vortex core exists in both non-reacting and reacting cases; it originates at the swirler centerbody. In the non-reacting case, its off-axis precessing motion dominates its dynamics. In the reacting flow, the vortex core dynamics is dominated by a “cork screw" type rotation with only a weak off-axis motion around the combustor’s centerline.

3. LES results show that the “cork screw" shape and motion of the HVC is responsible for the large scale flame wrinkling exhibited by the two-dimensional experimental results.

# Chapter 7

# Summary of Contribution and Publications

We investigated experimentally (using advanced laser diagnostics) and numerically (using Large Eddy Simulations) premixed combustion dynamics and the complex interactions between the turbulent flow and the flame in a practical swirling flow configuration, similar to those found in modern gas turbine combustors. An original contribution was made where we highlighted a new triggering mechanism of thermo-acoustic instabilities and propose a scaling model to predict flame stabilization modes under a wide range of fuels, diluents and operating conditions. Moreover, the series of experiments and LES simulations undertaken provide an improved understanding of the reacting swirling flow field dynamics and the effect of heat release on the flow. In this chapter, we summarize this thesis's contribution point by point and these are followed by the publications that resulted from it. Each contribution was detailed in a chapter of this thesis manuscript.

# Summary of Contribution and Main Publications

The original contribution of this thesis to the scientific community can be summarized as follows:

1. We reviewed the progress made in understanding the effects of fuel composition on premixed gas turbine combustion, with a special emphasis on system stability and emissions, for hydrogen-rich fuel mixtures. Due to the substantially different chemical, transport and thermal properties that distinguish different fuels, especially $H_2$, when compared with conventional hydrocarbon fuels, these non-standard fuels pose several challenges in premixed combustion. These challenges were reviewed along with the combustion fundamentals of such fuels. A survey of available technologies able to handle syngas and hydrogen-rich fuel in general was done reflecting the difficulties encountered while using these fuels in real large scale commercial applications. A large part of this comprehensive review is not included in this manuscript since it goes beyond the issues we focus on in this thesis (combustion dynamics). The full literature review can be found in the published paper (see below).

    - **S. Taamallah**, K. Vogiatzaki, F.M. Alzahrani, E.M.A. Mokheimer, M.A.M. Habib and A.F. Ghoniem, "Fuel flexibility, stability and emissions in premixed hydrogen-rich gas turbine combustion: Technology, fundamentals, and numerical simulations", (Review paper) Applied Energy Journal, Volume 154, 2015. [Web Link]

2. A comparison of stability maps and flame macrostructures with their counterparts in an acoustically decoupled version of the combustion system demonstrated that the onset of thermo-acoustic instabilities is concomitant with the appearance and stabilization of the flame in the the swirling flow's outside recirculation zone (ORZ)

and shear layer (OSL). This is valid for different $CH_4$-$H_2$ fuel blends. This showed that the flame transition to the ORZ is an important flame transition that can be responsible for the onset of thermo-acoustic instability. The sudden onset of large amplitude limit cycle oscillations and the observed hysteresis suggest the existence of a sub-critical Hopf bifurcation typically characterized by a bi-stable or "triggering" zone: the flame intermittency in the ORZ can potentially provide the disturbance required to trigger these oscillations. In the acoustically decoupled case, the transition of the flame to the ORZ occurs gradually starting with the intermittent appearance of a flame in the ORZ. Spectral analysis of this phenomenon, we referred to as "ORZ flame flickering" shows the existence of an unsteady event occurring over a narrow frequency band centered around 28 Hz along with a weaker broadband region at lower frequency in the range [5-10] Hz. The low frequency dynamics is associated with the pulsation of the inner recirculation zone (IRZ) while the 28 Hz tone was shown to be due to the azimuthal advection of the flame by the outer recirculation zone flow. This first step in the analysis of the onset of thermo-acoustic instability led to two publications (see below).

- **S. Taamallah**, Z. LaBry, S.J. Shanbhogue and A.F. Ghoniem "Thermo-acoustic Instabilities in Lean Premixed Swirl-stabilized Combustion and Their Link to Acoustically Coupled and Decoupled Flame Macrostructures", Proceedings of the Combustion Institute, Volume 35, Issue 3, 2015. [Web Link]
- **S. Taamallah**, Z. LaBry, S.J. Shanbhogue, M.A.M. Habib and A.F. Ghoniem, "Correspondence Between "Stable" Flame Macrostructure and Thermo-acoustic Instability in Premixed Swirl-Stabilized Turbulent Combustion", Journal of Engineering for Gas Turbines and Power, 137, 2015. [Web Link]

3. Naturally after the previous step, we investigated the mechanism underlying the

flame transition to the ORZ and proposed a criterion for its occurrence, in an acoustically decoupled combustion system. To reach this goal, the effects of $H_2$ addition, Reynolds number, swirler blade angle and heat loss were experimentally analyzed using multiple advanced optical diagnostics. We found evidence that the transition starts with an intermittent inflammation of the ORZ caused by a flame kernel detaching from the ISL. Above a critical equivalence ratio that depends on the operating conditions, the flame kernel expands and spins along with the ORZ flow. Below that equivalence ratio, the flame kernel can reach the ORZ but always extinguishes and fail to expand. Next, we explored the effect of the operating conditions on the onset of an ORZ flame as well as on the dominant flow-flame dynamics during the transition. We proposed a Strouhal number to describe the observed intermittent ORZ flame spinning also shown to be a predominately hydrodynamic quantity as it was shown to be independent of $H_2$ addition. Finally, we showed that the flame transition to the ORZ is governed by a balance between a flame time and a flow time that can be expressed in a form of a Karlovitz number ($Ka_{ORZ}$) defined as the ratio of the ORZ spinning frequency and the extinction strain rate ; The former is a surrogate for the bulk azimuthal strain rate in the ORZ. Following the interpretation of the ORZ spinning frequency as a bulk strain rate, the flame can survive in the ORZ if it can overcome that region's bulk strain rate i.e. when its extinction strain rate is higher than the prevailing strain.

- **S. Taamallah**, S.J. Shanbhogue and A.F. Ghoniem, "Turbulent Flame Stabilization Modes in Premixed Swirl Combustion: Physical Mechanism and Karlovitz number based Predictive Criterion", Accepted for Publication in Combustion and Flame, 2015.

4. The previous model was extended to Oxy-combustion. We compared the conditions

leading to the stabilization of turbulent methane air and oxy-flames in the ORZ. We found that, when similar flow conditions are imposed in the ORZ, the transition is also governed by the extinction strain and can occur at different adiabatic flame temperature and unstretched laminar burning velocity. First, we showed that the non-dimensional parameter characterizing the flow in the ORZ, that is the Strouhal number associated with the azimuthal ORZ spinning frequency, is independent of the Reynolds number and has the same constant value in air and oxy-combustion ($St = \frac{f_{ORZ}.D_{in}}{U_{in}} \approx 0.12$). This has the important implication that the inlet velocity is a more relevant parameter choice than the inlet Reynolds number in order to maintain similar flow conditions in the ORZ. Next, by comparing the extinction strain rates computed at the measured ORZ temperature, we demonstrated the existence of a single correlation between the inverse of the ORZ spinning frequency (taken as a characteristic ORZ flow time) and the inverse of the extinction strain rate (taken as a characteristic flame time)allowing the scaling of oxy and air flames and delimiting the regions of existence of different flame macrostructures independently from the diluent.

- **S. Taamallah**, N.W. Chakroun, H. Watanabe, S.J. Shanbhogue and A.F. Ghoniem, "On the Characteristic Flow and Flame Times For Scaling Oxy and Air Flame Stabilization Modes in Premixed Swirl Combustion", Submitted to the 36th Proceedings of the Combustion Institute (Under Review).

5. Finally, we showed how Large Eddy Simulations (LES) can be successfully used to complement 2D optical diagnostics tools and elucidate the origin and dynamics of the flow and flame structures observed in the experiment. Vortical structures interact with the flame and can lead to heat release disturbances hence the importance of examining their origin. LES simulations showed that these flame and flow

structures come from a helical vortex core (HVC). The helical structure resemble a conical "cork-screw" that originates from the swirler's centerbody; This vortical structure stays aligned with the centerline in the combustor upstream section, but bends and reaches the inner shear layer-stabilized flame around the sudden expansion where it causes the flame wrinkling. We proposed that the flame kernel igniting the ORZ/OSL observed in the experiment may be related to the interaction between the helical vortical structure and the outer shear layer.

- **S. Taamallah**, N.W. Chakroun, S.J. Shanbhogue, K. Vogiatzaki, G. Kewlani and A.F. Ghoniem, "Vortical Structures Dynamics and Flame Interaction in Turbulent Premixed Swirl-Stabilized Combustion: a Combined Experimental and LES Investigation", in preparation for Submission to Physics of Fluids Journal.

# Other Publications Related to the Thesis

In addition to the Peer-Reviewed Journal Papers listed above, peer-reviewed conference proceedings publications and abstract-reviewed conference presentations related to the current thesis were done. These are listed below.

### Peer-Reviewed Conference Proceedings

- **S. Taamallah**, Z. LaBry, S.J. Shanbhogue and A.F. Ghoniem, "Correspondence between uncoupled flame macrostructures and thermoacoustic instability in premixed swirl-stabilized combustion", ASME Turbo Expo 2014 - Dusseldorf, Germany. GT2014-27316. (Recommended for journal publication). [Web Link]
- **S. Taamallah**, S.J. Shanbhogue, Y.S. Sanusi, E.M.A. Mokhiemer and A.F. Ghoniem , "Transition from a single to a double flame structure in swirling re-

acting flows: mechanism, dynamics, and effect of thermal boundary conditions", ASME Turbo Expo 2015 - Montreal, Canada. GT2015-43998. (Invited for journal publication). [Web Link]

- Z. LaBry, **S. Taamallah**, G. Kewlani, S. J. Shanbhogue and A. F. Ghoniem, "Mode transition and intermittency in an acoustically uncoupled lean premixed swirl-stabilized combustor", ASME Turbo Expo 2014 - Dusseldorf, Germany. GT2014-27266. [Web Link]

**Abstract-Reviewed Conference Papers**

- S.J. Shanbhogue, **S. Taamallah**, S.H. Hong, H. Watanabe, Z.A. LaBry, R.L. Speth, Ahmed F. Ghoniem, "Is Scaling of Premixed Turbulent Combustion Dynamics Using Strained Flame Models Possible ?", 9th U. S. National Combustion Meeting. Cincinnati, Ohio. May 17-20, 2015.

- S.J. Shanbhogue, Y.S. Sanusi, **S. Taamallah**, M.A. Habib, E.M.A. Mokheimer, and A.F. Ghoniem, "Scaling of Combustion Instability Mode Transitions Associated with the Appearance of the Outer Recirculation Zone Flame in Swirling $CH_4/H_2$ Mixtures.", 9th U. S. National Combustion Meeting. Cincinnati, Ohio. May 17-20, 2015.

**Abstract-Reviewed Conference Presentations**

- **S. Taamallah et al.**, "Importance of the Representation of Experimental Boundary Conditions for Swirling and Non swirling Jet Flows in Large Eddy Simulations", 14th Conference on Numerical Combustion, San Antonio Texas; 04/2013.

- **S. Taamallah**, K. Vogiatzaki, G. Kewlani, S.J. Shanbhogue, and A.F. Ghoniem, "Experimental and Numerical Investigation of Vortical Structures in Lean Pre-

mixed Swirl-Stabilized Combustion", 68th Annual Meeting of the APS Division of Fluid Dynamics, Boston, MA, November 22-24, 2015. [Web Link]

# Appendix A

# LES Equations

The density-weighted filtered (Favre filtering) Navier-Stokes equations that are solved for the flow field, are shown below, following general form (using Poinsot et al. notations [75]). Several terms are neglected in our implementation based on the specific flow conditions we are simulating in this thesis.

$$\overline{p} = \overline{\rho} R \widetilde{T} \quad (Equation\ of\ state) \tag{A.1}$$

$$\frac{\partial \overline{\rho}}{\partial t} + \frac{\partial \overline{\rho} \widetilde{u}_j}{\partial x_j} = 0 \tag{A.2}$$

$$\frac{\partial \overline{\rho} \widetilde{u}_i}{\partial t} + \frac{\partial \overline{\rho} \widetilde{u}_i \widetilde{u}_j}{\partial x_i} = -\frac{\partial \overline{p}}{\partial x_i} + \underbrace{f_i}_{C} + \frac{\partial}{\partial x_i} ( \underbrace{\overline{\tau}_{ij}}_{A} - \underbrace{\overline{\rho} (\widetilde{u_i u_j} - \widetilde{u}_i \widetilde{u}_j)}_{B} ) \tag{A.3}$$

$$\frac{\partial \overline{\rho}\widetilde{Y}_k}{\partial t} + \frac{\partial \overline{\rho}\widetilde{u}_i\widetilde{Y}_k}{\partial x_i} = \underbrace{\frac{\partial}{\partial x_i}(\overline{V_{k,i}Y_k}}_{I} - \underbrace{\rho(\widetilde{u_iY_k} - \widetilde{u}_i\widetilde{Y}_k))}_{J} + \underbrace{\overline{\dot{\omega}_k}}_{K} \tag{A.4}$$

$$\begin{aligned}\frac{\partial \overline{\rho}\widetilde{h}_s}{\partial t} + \frac{\partial \overline{\rho}\widetilde{u}_i\widetilde{h}_s}{\partial x_i} &= \underbrace{\overline{\frac{Dp}{Dt}}}_{D} + \frac{\partial}{\partial x_i}(\underbrace{\lambda\overline{\frac{\partial T}{\partial x_i}}}_{E_1} - \underbrace{\rho(\widetilde{u_ih_s} - \widetilde{u}_i\widetilde{h}_s)}_{E_2}) + \underbrace{\overline{\tau_{ij}\frac{\partial u_i}{\partial x_j}}}_{F} - \underbrace{\frac{\partial}{\partial x_i}(\overline{\rho\sum_{k=1}^{N} V_{k,i}Y_kh_{s,k}})}_{G} \\ &\quad + \underbrace{\overline{\dot{\omega}_T}}_{H}\end{aligned} \tag{A.5}$$

where t is the time and $x_i$ the space variable (Einstein notation was used). $\rho$, $u_i$ and $p$ represent the density, the spatial components of velocity and pressure of the gaseous mixture respectively. $\mu$ is the molecular viscosity. $h_s$ and T and $\lambda$ are the sensible enthalpy, the temperature and the thermal diffusivity. $Y_k$ is the mass fraction of species $k$. The over bars and tildes represent the spatially filtered and density-weighted filtered values with a filter width $\Delta$ respectively.

The terms (A to K) in the system of governing equation are detailed below. These are in some cases modeled and other cases neglected:

- A: molecular or resolved viscous stress modeled as $\tau_{ji} = -\frac{2}{3}\mu\frac{\partial\widetilde{u}_k}{\partial x_k}\delta_{ji} + \mu(\frac{\partial\widetilde{u}_j}{\partial x_i} + \frac{\partial\widetilde{u}_i}{\partial x_j})$ for a Newtonian fluid.
- B: The sub-grid scale (sgs) stress is unknown and results from the LES filtering operation. It represents the effect of the sub-grid stresses on all the scales equal or larger than the filter level. This term requires modeling and we use the Boussinesq hypothesis and the Prandtl's one-equation model based on the turbulent kinetic energy (TKE); this requires solving an additional PDE for k the turbulent kinetic energy.

- C: Body forces like gravity forces are neglected. The Froude number is estimated here Fr≈45.
- D: Heating due to compressibility effects. This term is characterized by the dimensionless Eckert number $\mathrm{E}_{ck} = \frac{U^2}{c_p\ \Delta T}$. In this study $\mathrm{E}_{ck} \approx 10^{-4}$ thus the heating due to compressibility effects can be neglected compared with heat release from combustion. This is generally the case in reacting flows and the term is neglect in our model.
- $E_1 and I$: The laminar diffusion fluxes (thermal and species) are approximated by the Fourier and Fick's law respectively using a molecular thermal and mass diffusivities.
- $E_2$: The unresolved sensible enthalpy flux is modeled using the gradient assumption analogous to Fourier's law but using a subgrid scale thermal diffusivity ($\alpha_{sgs}$). $\alpha_{sgs}$ is calculated from $\nu_{sgs}$ and a turbulent or sgs Prandtl number.
- F: The viscous dissipation term is neglected as the Brinkman number ($Br = \frac{\mu\, U^2}{k\ \Delta T}$) associated with this term is small compared to one $Br \approx 10^{-5}$.
- G: Heat transport due to species diffusion. This Dufour effect is neglected.
- H: Heat release due to chemical reactions.
- J: The unresolved species flux is modeled using also the gradient assumption analogous to Fick's law but using a subgrid scale mass diffusivity ($D_{sgs}$). $D_{sgs}$ is calculated from $\nu_{sgs}$ and a turbulent or sgs Schmidt number ($Sc_{sgs}$). $Sc_{sgs}$ is assumed equal to the laminar Schmidt number.
- K: The filtered reaction rate requires modeling. This is the subgrid scale combustion model. We use the thickened flame model (TFM) allowing the use of an Arrhenius type reaction rate.

# Appendix B

# 1-D Heat Transfer Modeling and Temperature Correction

The temperature is measured for the reference reacting case ($CH_4$ at $\phi$=0.6) using a K-type sheathed thermocouple $TC_2$ (sheath diameter is 1/16 inches, a response time around 1 s and sampling frequency of 20 Hz) inserted from the tube end along the centerline reaching a distance x = 0.2 m from the expansion plane (middle of the quartz tube). The measurement is repeated twice and steady state values are recorded and averaged in time to obtain $T_{probe}$. During this measurement the probe loses heat by radiation to the relatively colder chamber wall and a radiation correction is required. A simplified one dimensional steady state thermal resistance network model is used to estimate heat losses and the temperature at the wall by considering a thermal energy balance for the wall: internal forced convection to the wall , radiation from the products to the wall, conduction through the quartz tube thickness, radiation out to the environment and finally natural convection cooling of the tube. The wall resistance is neglected compared to other resistances and the wall temperature is assumed uniform across the wall. Heat is lost by natural convection and radiation exchange with the

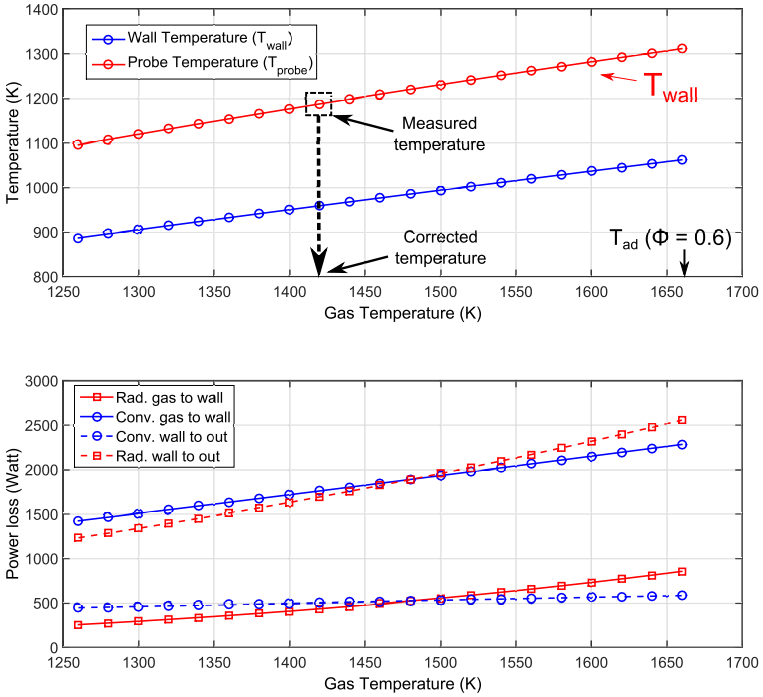


Figure B-1: Top: Gas and wall temperatures obtained from the radiation loss correction of the temperature measured by the thermocouple. Bottom: Modeled losses mechanism for half the combustor length (where the temperature measurement is performed). The black arrows correspond to the estimates based on the measured temperature.

surroundings at ambient temperature. Using this model, for each gas temperature ($T_{gas}$), a wall temperature ($T_{wall}$) can be solved for. Such a model allows also to estimate the relative weight of each heat transfer mode.

The downstream temperature measurement ($T_{probe}$) repeated twice gives 1181 K and 1188 K. Knowing $T_{probe}$ and by using a heat balance on the probe, which exchanges heat with the products flowing around it at $T_{gas}$ but also looses heat to the wall at $T_{wall}$ by radiation, $T_{gas}$ and the associated $T_{wall}$ are estimated. The corrected gas temperature is thus $T_{gas} = 1420$ K. This estimate of the gas temperature is used for LES results validations. Figure B-1 (a) shows the estimated wall and probe temperatures as a function of the gas temperature using the 1D model. In Figure B-1 (b) the contribution of each mode of heat transfer from the hot gases is estimated. The total

power input is equal to 19.8 kW (for $CH_4$-air at $\phi$=0.60 and Re=20,000). About 18% is estimated to be lost by forced heat convection to the wall and 4% by radiation which led us to neglect radiation modeling in LES calculations.

# Bibliography


[1] A Amato, B Hudak, P D'Carlo, D Noble, D Scarborough, J Seitzman, and T Lieuwen. Methane oxycombustion for low $CO_2$ cycles: Blowoff measurements and analysis. *Journal of Engineering for Gas Turbines and Power*, 133(6), 2011.

[2] M Baratieri, P Baggio, B Bosio, M Grigiante, and GA Longo. The use of biomass syngas in ic engines and ccgt plants: a comparative analysis. *Applied Thermal Engineering*, 29(16):3309–3318, 2009.

[3] J. M. Beer and N.A. Chigier. *Combustion aerodynamics*. Krieger, 1983.

[4] Gal Berkooz, Philip Holmes, and John L Lumley. The proper orthogonal decomposition in the analysis of turbulent flows. *Annual review of fluid mechanics*, 25(1):539–575, 1993.

[5] Paul Billant, Jean-Marc Chomaz, and Patrick Huerre. Experimental study of vortex breakdown in swirling jets. *Journal of Fluid Mechanics*, 376:183–219, 1998.

[6] O. Bolland and J. F. Stadaas. Comparative evaluation of combined cycles and gas turbine systems with water injection, steam injection, and recuperation. *Journal of engineering for gas turbines and power*, 117(1):138–145, 1995.

[7] Dominik Bongartz and Ahmed F. Ghoniem. Chemical kinetics mechanism for oxy-fuel combustion of mixtures of hydrogen sulfide and methane. *Combustion and Flame*, 162(3):544 – 553, 2015.

[8] Nicolas Bouvet, Fabien Halter, Christian Chauveau, and Youngbin Yoon. On the effective lewis number formulations for lean hydrogen/hydrocarbon/air mixtures. *International Journal of Hydrogen Energy*, 38(14):5949 – 5960, 2013.

[9] Sebastien Candel. Combustion dynamics and control: Progress and challenges. *Proceedings of the Combustion Institute*, 29(1):1 – 28, 2002. Proceedings of the Combustion Institute.

[10] Kent H. Casleton, Ronald W. Breault, and George A. Richards. System issues and tradeoffs associated with syngas production and combustion. *Combustion Science and Technology*, 180(6):1013–1052, 2008.

[11] Lei Chen, Sze Zheng Yong, and Ahmed F Ghoniem. Oxy-fuel combustion of pulverized coal: Characterization, fundamentals, stabilization and cfd modeling. *Progress in Energy and Combustion Science*, 38(2):156–214, 2012.

[12] I Chterev, CW Foley, S Kostka, AW Caswell, N Jiang, JM Seitzman, and TC Lieuwen. Flame and flow topologies in an annular swirling flow. In *ASME Turbo Expo 2013: Turbine Technical Conference and Exposition*. American Society of Mechanical Engineers, 2013.

[13] I. Chterev, C.W. Foley, D.R. Noble, B.A. Ochs, J.M. Seitzman, and T.C. Lieuwen. Shear layer flame stabilization sensitivities in a swirling flow. *Proceedings of ASME Turbo Expo 2012*, 2012.

[14] O. Colin, F. Ducros, D. Veynante, and T. Poinsot. A thickened flame model for large eddy simulations of turbulent premixed combustion. *Physics of Fluids*, 12(7):1843–1863, 2000.

[15] Marcos Escudero, Celina Gonzalez, and Ignacio Lopez. Quantitative analysis of potential power production and environmental benefits of biomass integrated gasification combined cycles in the european union. *Energy Policy*, 53, 2013.

[16] D Ferguson, D Straub, G.A. Richards, and E Robey. Impact of fuel variability on dynamic instabilities in gas turbine combustion. In *Engines*. Western States Section of the Combustion Institute, 2007.

[17] Lorenzo Figura, Jong Guen Lee, Bryan D Quay, and Domenic A Santavicca. The effects of fuel composition on flame structure and combustion dynamics in a lean premixed combustor. In *ASME Turbo Expo 2007: Power for Land, Sea, and Air*, pages 181–187. American Society of Mechanical Engineers, 2007.

[18] Charles Fleming. Turbine makers are caught in innovation trap. *Wall Street Journal*, february 1988.

[19] C Foley, I Chterev, J Seitzman, and T Lieuwen. Flame configurations in a lean premixed dump combustor with an annular swirling flow. In *7th US National Combustion Meeting*, number 1D16, 2011.

[20] D Fritsche, M Füri, and K Boulouchos. An experimental investigation of thermoacoustic instabilities in a premixed swirl-stabilized flame. *Combustion and Flame*, 151(1):29–36, 2007.

[21] D Fritsche, M Füri, and K Boulouchos. An experimental investigation of thermoacoustic instabilities in a premixed swirl-stabilized flame. *Combustion and Flame*, 151(1):29–36, 2007.

[22] François Gallaire and J-M Chomaz. Instability mechanisms in swirling flows. *Physics of Fluids (1994-present)*, 15(9):2622–2639, 2003.

[23] M García-Villalba, J Fröhlich, and W Rodi. Identification and analysis of coherent structures in the near field of a turbulent unconfined annular swirling jet using large eddy simulation. *Physics of Fluids*, 18(5):055103, 2006.

[24] Matteo Gazzani, Paolo Chiesa, Emanuele Martelli, Stefano Sigali, and Iarno Brunetti. Using hydrogen as gas turbine fuel: Premixed versus diffusive flame combustors. *Journal of Engineering for Gas Turbines and Power*, 136(5):051504, 2014.

[25] L.Y.M. Gicquel, G. Staffelbach, and T. Poinsot. Large eddy simulations of gaseous flames in gas turbine combustion chambers. *Progress in Energy and Combustion Science*, 38(6):782 – 817, 2012.

[26] Peter Glarborg and Line LB Bentzen. Chemical effects of a high $CO_2$ concentration in oxy-fuel combustion of methane. *Energy & Fuels*, 22(1):291–296, 2007.

[27] Dave Goodwin, Nicholas Malaya, Harry Moffat, and Raymond Speth. Cantera: An object-oriented software toolkit for chemical kinetics, thermodynamics, and transport processes. *Caltech, Pasadena, CA*, 2009.

[28] F Grisch and M Orain. Role of planar laser-induced fluorescence in combustion research. *Onera Aerospacelab Journal*, 2009.

[29] TF Guiberti, D Durox, P Scouflaire, and T Schuller. Impact of heat loss and hydrogen enrichment on the shape of confined swirling flames. *Proceedings of the Combustion Institute*, 2014.

[30] TF Guiberti, L Zimmer, D Durox, and T Schuller. Experimental analysis of v to m shape transition of premixed CH4/H2/air swirling flames. *Proceedings of ASME Turbo Expo 2013*, 2013.

[31] Ashwani K Gupta, David Grantham Lilley, and Nick Syred. Swirl flows. *Tunbridge Wells, Kent, England, Abacus Press, 1984, 488 p.*, 1, 1984.

[32] Satoshi Hada, Masanori Yuri, Junichiro Masada, Eisaku Ito, and Keizo Tsukagoshi. Evolution and future trend of large frame gas turbines: A new 1600 degree C, J-class gas turbine. In *ASME Turbo Expo 2012: Turbine Technical Conference and Exposition*, pages 599–606. ASME, 2012.

[33] Adam G. Hendricks and Uri Vandsburger. The effect of fuel composition on flame dynamics. *Experimental Thermal and Fluid Science*, 32(1):126 – 132, 2007.

[34] Seunghyuck Hong, Raymond L. Speth, Santosh J. Shanbhogue, and Ahmed F. Ghoniem. Examining flow-flame interaction and the characteristic stretch rate in vortex-driven combustion dynamics using PIV and numerical simulation. *Combustion and Flame*, 160(8):1381 – 1397, 2013.

[35] Ying Huang, Hong-Gye Sung, Shih-Yang Hsieh, and Vigor Yang. Large-eddy simulation of combustion dynamics of lean-premixed swirl-stabilized combustor. *Journal of Propulsion and Power*, 19(5):782–794, 2003.

[36] Ying Huang and Vigor Yang. Effect of swirl on combustion dynamics in a lean-premixed swirl-stabilized combustor. *Proceedings of the Combustion Institute*, 30(2):1775 – 1782, 2005.

[37] Ying Huang and Vigor Yang. Dynamics and stability of lean-premixed swirl-stabilized combustion. *Progress in Energy and Combustion Science*, 35(4):293 – 364, 2009.

[38] Ying Huang and Vigor Yang. Dynamics and stability of lean-premixed swirl-stabilized combustion. *Progress in Energy and Combustion Science*, 35(4):293–364, 2009.

[39] M.C. Janus, G.A. Richards, M.J. Yip, and E.H. Robey. Effects of ambient conditions and fuel composition on combustion stability, 1997.

[40] Jinhee Jeong and Fazle Hussain. On the identification of a vortex. *Journal of fluid mechanics*, 285:69–94, 1995.

[41] WP Jones and RP Lindstedt. Global reaction schemes for hydrocarbon combustion. *Combustion and flame*, 73(3):233–249, 1988.

[42] P Jourdaine, C Mirat, J Beaunier, Y Joumani, and T Schuller. A comparison of the structure of $N_2$ and $CO_2$ diluted $CH_4/O_2$ premixed flames in a swirled combustor. In *Proceedings of the European Combustion Meeting 2015*.

[43] Lipika Kabiraj and RI Sujith. Nonlinear self-excited thermoacoustic oscillations: intermittency and flame blowout. *Journal of Fluid Mechanics*, 713:376–397, 2012.

[44] Gaurav Kewlani, Zachary Labry, Neerav Abani, Santosh Shanbhogue, and Ahmed Ghoniem. Large eddy simulations and experimental investigation of flow in a swirl stabilized combustor. In *50th AIAA Aerospace Sciences Meeting including the New Horizons Forum and Aerospace Exposition*, page 178. American Institute of Aeronautics and Astronautics, 2012.

[45] Gaurav Kewlani, Konstantina Vogiatzaki, Santosh Shanbhogue, and Ahmed F Ghoniem. Validation study of large-eddy simulations of wake stabilized reacting flows using artificial flame thickening approaches. In *51st AIAA Aerospace Sciences Meeting including the New Horizons Forum and Aerospace Exposition*, page 169. American Institute of Aeronautics and Astronautics, 2013.

[46] Hiroyuki Kido and Masaya Nakahara. A model of turbulent burning velocity taking the preferential diffusion effect into consideration. *JSME international journal. Series B, fluids and thermal engineering*, 41(3):666–673, 1998.

[47] Kyu Tae Kim, Jong Guen Lee, Hyung Ju Lee, Bryan D Quay, and Domenic A Santavicca. Characterization of forced flame response of swirl-stabilized turbulent lean-premixed flames in a gas turbine combustor. *Journal of Engineering for Gas Turbines & Power*, 132(4):041502, 2010.

[48] P Knoop, FEC Culick, and EE Zukoski. Extension of the stability of motions in a combustion chamber by nonlinear active control based on hysteresis. *Combustion science and technology*, 123(1-6):363–376, 1997.

[49] A. Kushari, L.J. Rosen, J.I. Jagoda, and B.T. inn. The effect of heat content and composition of fuel on pulse combustor performance. *Symposium (International) on Combustion*, 26(2):3363 – 3368, 1996.

[50] Peter Kutne, Bhavin K Kapadia, Wolfgang Meier, and Manfred Aigner. Experimental analysis of the combustion behaviour of oxyfuel flames in a gas turbine model combustor. *Proceedings of the Combustion Institute*, 33(2):3383–3390, 2011.

[51] Zachary A LaBry, Santosh J Shanbhogue, Raymond L Speth, and Ahmed F Ghoniem. Instability suppression in a swirl-stabilized combustor using microjet air injection. *48th AIAA Aerospace Sciences Meeting including the New Horizons Forum and Aerospace Exposition*, january 2010.

[52] Zachary A LaBry, Soufien Taamallah, Gaurav Kewlani, Santosh J Shanbhogue, and Ahmed F Ghoniem. Mode transition and intermittency in an acoustically uncoupled lean premixed swirl-stabilized combustor. *Proceedings of ASME Turbo Expo*, GT2014-27266, 2014.

[53] Jong G Lee, Esteban Gonzalez, and Domenic A Santavicca. On the applicability of chemiluminescence to the estimation of unsteady heat-release during unstable combustion in lean premixed combustor. *AIAA Paper*, (2005-3575), 2005.

[54] Min Chul Lee, Seok Bin Seo, Jae Hwa Chung, Si Moon Kim, Yong Jin Joo, and Dal Hong Ahn. Gas turbine combustion performance test of hydrogen and carbon monoxide synthetic gas. *Fuel*, 89(7):1485–1491, 2010.

[55] Arthur H Lefebvre. *Gas turbine combustion*. CRC Press, 2010.

[56] Tim C Lieuwen. Experimental investigation of limit-cycle oscillations in an unstable gas turbine combustor. *Journal of Propulsion and Power*, 18(1):61–67, 2002.

[57] Tim C Lieuwen. *Unsteady combustor physics*. Cambridge University Press, 2012.

[58] A.N. Lipatnikov and J. Chomiak. Turbulent flame speed and thickness: phenomenology, evaluation, and application in multi-dimensional simulations. *Progress in Energy and Combustion Science*, 28(1):1 – 74, 2002.

[59] Xiyun Lu, Shanwu Wang, Hong-Gye Sung, Shih-Yang Hsieh, and Vigor Yang. Large-eddy simulations of turbulent swirling flows injected into a dump chamber. *Journal of Fluid Mechanics*, 527:171–195, 2005.

[60] O Lucca-Negro and T O'doherty. Vortex breakdown: a review. *Progress in Energy and Combustion Science*, 27(4):431–481, 2001.

[61] E. Mallard and H.L. Chatelier. *Recherches expérimentales et théoriques sur la combustion des mélanges gazeux explosives*. H.Dunod et E. Pinat, 1883.

[62] Sathesh Mariappan and RI Sujith. Modelling nonlinear thermoacoustic instability in an electrically heated rijke tube. *Journal of Fluid Mechanics*, 680:511–533, 2011.

[63] Kaoru Maruta, Kazuki Abe, Susumu Hasegawa, Shigenao Maruyama, and Jun'ichi Sato. Extinction characteristics of $CH_4/CO_2$ versus $O_2/CO_2$ counterflow non-premixed flames at elevated pressures up to 0.7 MPa. *Proceedings of the Combustion Institute*, 31(1):1223 – 1230, 2007.

[64] Teresa Mendiara and Peter Glarborg. Ammonia chemistry in oxy-fuel combustion of methane. *Combustion and Flame*, 156(10):1937–1949, 2009.

[65] Jonas P. Moeck, Jean-Francois Bourgouin, Daniel Durox, Thierry Schuller, and Sebastien Candel. Nonlinear interaction between a precessing vortex core and acoustic oscillations in a turbulent swirling flame. *Combustion and Flame*, 159(8):2650 – 2668, 2012. Special Issue on Turbulent Combustion.

[66] HK Moffatt. Spiral structures in turbulent flow. In *New Approaches and Concepts in Turbulence*, pages 121–129. Springer, 1993.

[67] Masaya Nakahara and Hiroyuki Kido. Study on the turbulent burning velocity of hydrogen mixtures including hydrocarbon. *AIAA journal*, 46(7):1569–1575, 2008.

[68] F. Nicoud and T. Poinsot. Thermoacoustic instabilities: Should the rayleigh criterion be extended to include entropy changes ? *Combustion and Flame*, 142(1âĂŞ2):153 – 159, 2005.

[69] Kilian Oberleithner, Moritz Sieber, CN Nayeri, CO Paschereit, Christoph Petz, H-C Hege, BR Noack, and I Wygnanski. Three-dimensional coherent structures in a swirling jet undergoing vortex breakdown: stability analysis and empirical mode construction. *Journal of Fluid Mechanics*, 679:383–414, 2011.

[70] Kilian Oberleithner, Michael Stöhr, Seong Ho Im, Christoph M Arndt, and Adam M Steinberg. Formation and flame-induced suppression of the precessing vortex core in a swirl combustor: experiments and linear stability analysis. *Combustion and Flame*, 2015.

[71] Kilian Oberleithner, Steffen Terhaar, Lothar Rukes, and Christian Oliver Paschereit. Why nonuniform density suppresses the precessing vortex core. *Journal of Engineering for Gas Turbines and Power*, 135(12):121506, 2013.

[72] Jacqueline O'Connor and Tim Lieuwen. Recirculation zone dynamics of a transversely excited swirl flow and flame. *Physics of Fluids*, 24(7):075107, 2012.

[73] Christian Oliver Paschereit, Ephraim Gutmark, and Wolfgang Weisenstein. Coherent structures in swirling flows and their role in acoustic combustion control. *Physics of Fluids (1994-present)*, 11(9):2667–2678, 1999.

[74] Norbert Peters. *Turbulent combustion*. Cambridge university press, 2000.

[75] T. Poinsot and D. Veynante. *Theoretical and numerical combustion*. Edwards, Philadelphia, 2005.

[76] Lord Rayleigh. The explanation of certain acoustical phenomena. *Nature*, 18:319–321, july 1878.

[77] CHEMKIN-PRO Release. 15101, reaction design. *Inc., San Diego, CA*, 2010.

[78] G.A Richards, M.M McMillian, R.S Gemmen, W.A Rogers, and S.R Cully. Issues for low-emission, fuel-flexible power systems. *Progress in Energy and Combustion Science*, 27(2):141 – 169, 2001.

[79] Antonio Rovira, Maria Jose Montes, Fernando Varela, and Monica Gil. Comparison of heat transfer fluid and direct steam generation technologies for integrated solar combined cycles. *Applied Thermal Engineering*, 52:264âĂŞ274, 2013.

[80] Jon Runyon, Richard Marsh, Agustin Valera-Medina, Anthony Giles, Steve Morris, Daniel Pugh, Yura Sevcenco, and Phil Bowen. Methane-oxygen flame stability in a generic premixed gas turbine swirl combustor at varying thermal power and pressure. In *ASME Turbo Expo 2015*. ASME, 2015.

[81] Turgut Sarpkaya. Turbulent vortex breakdown. *Physics of Fluids (1994-present)*, 7(10):2301–2303, 1995.

[82] R.W. Schefer, D.M. Wicksall, and A.K. Agrawal. Combustion of hydrogen-enriched methane in a lean premixed swirl-stabilized burner. *Proceedings of the Combustion Institute*, 29(1):843 – 851, 2002. <ce:title>Proceedings of the Combustion Institute</ce:title>.

[83] Ducruix Sébastien, Schuller Thierry, Durox Daniel, and Candel Sébastien. Combustion dynamics and instabilities: Elementary coupling and driving mechanisms. *Journal of Propulsion and Power*, 19(5):722–734, 2003.

[84] S.J. Shanbhogue, Y.S. Sanusi, S. Taamallah, M.A. Habib, E.M.A. Mokheimer, and A.F. Ghoniem. Flame macrostructures, combuztion instability and extinction strain scaling in swirl-stabilized premixed ch4-h2 combustion. *Combustion and Flame*, Accepted for Publication - 2015.

[85] Elysia J. Sheu and Ahmed F. Ghoniem. Redox reforming based, integrated solar-natural gas plants: Reforming and thermodynamic cycle efficiency. *International Journal of Hydrogen Energy*, 39(27):14817 – 14833, 2014.

[86] Elysia J. Sheu and Alexander Mitsos. Optimization of a hybrid solar-fossil fuel plant: Solar steam reforming of methane in a combined cycle. *Energy*, 51(0):193 – 202, 2013.

[87] Andrew Shroll. Dynamic stability, blowoff, and flame characteristics of oxy-fuel combustion. Master's thesis, Massachusetts Institute of Technology, Cambridge MA, USA, 2011.

[88] Andrew P. Shroll, Santosh J. Shanbhogue, and Ahmed F. Ghoniem. Dynamic-stability characteristics of premixed methane oxy-combustion. *Journal of Engineering for Gas Turbines and Power*, 134(5), 2012.

[89] Lawrence Sirovich. Turbulence and the dynamics of coherent structures. part i: Coherent structures. *Quarterly of applied mathematics*, 45(3):561–571, 1987.

[90] Gregory P Smith, David M Golden, Michael Frenklach, Nigel W Moriarty, Boris Eiteneer, Mikhail Goldenberg, C Thomas Bowman, Ronald K Hanson, Soonho Song, William C Gardiner Jr, et al. Gri-mech 3.0. 1999.

[91] Raymond L Speth, H Murat Altay, Duane E Hudgins, and Ahmed F Ghoniem. Dynamics and stability limits of syngas combustion in a swirl-stabilized combustor. *Proceedings of ASME Turbo Expo 2008*, 2008.

[92] Raymond L. Speth and Ahmed F. Ghoniem. Using a strained flame model to collapse dynamic mode data in a swirl-stabilized syngas combustor. *Proceedings of the Combustion Institute*, 32(2):2993 – 3000, 2009.

[93] Raymond L. Speth and Ahmed F. Ghoniem. Using a strained flame model to collapse dynamic mode data in a swirl-stabilized syngas combustor. *Proceedings of the Combustion Institute*, 32(2):2993 – 3000, 2009.

[94] KR Sreenivasan and S Raghu. The control of combustion instability: A perspective. *Current Science*, 79(6):867–883, 2000.

[95] KR Sreenivasan and S Raghu. The control of combustion instability: A perspective. *Curr. Sci*, 79:867–883, 2000.

[96] AM Steinberg, CM Arndt, and W Meier. Parametric study of vortex structures and their dynamics in swirl-stabilized combustion. *Proceedings of the Combustion Institute*, 34(2):3117–3125, 2013.

[97] Ulrich Stopper, Wolfgang Meier, Rajesh Sadanandan, Michael Stohr, Manfred Aigner, and Ghenadie Bulat. Experimental study of industrial gas turbine flames including quantification of pressure influence on flow field, fuel/air premixing and flame shape. *Combustion and Flame*, 160(10):2103–2118, 2013.

[98] P. Strakey, T. Sidwell, and J. Ontko. Investigation of the effects of hydrogen addition on lean extinction in a swirl stabilized combustor. *Proceedings of the Combustion Institute*, 31(2):3173 – 3180, 2007.

[99] Nicholas Syred. A review of oscillation mechanisms and the role of the precessing vortex core (pvc) in swirl combustion systems. *Progress in Energy and Combustion Science*, 32(2):93–161, 2006.

[100] Soufien Taamallah, Zachary A. LaBry, Santosh J. Shanbhogue, and Ahmed F. Ghoniem. Thermo-acoustic instabilities in lean premixed swirl-stabilized combustion and their link to acoustically coupled and decoupled flame macrostructures. *Proceedings of the Combustion Institute*, 2014.

[101] Soufien Taamallah, Zachary A. LaBry, Santosh J. Shanbhogue, Mohamed A. M. Habib, and Ahmed F. Ghoniem. Correspondence between "stable" flame macrostructure and thermo-acoustic instability in premixed swirl-stabilized turbulent combustion. *Journal of Engineering for Gas Turbines and Power*, 137(7), 2015.

[102] Soufien Taamallah, Santosh J. Shanbhogue, and Ahmed F. Ghoniem. Turbulent flame stabilization modes in premixed swirl combustion: Mechanisms and Karlovitz number based predictive criteria. *Combustion and Flame*, 2015.

[103] Soufien Taamallah, Konstantina Vogiatzaki, Fahad M. Alzahrani, Esmail M.A. Mokheimer, Mohamed A. Habib, and Ahmed F. Ghoniem. Fuel flexibility, stability and emissions in premixed hydrogen-rich gas turbine combustion: Technology, fundamentals, and numerical simulations. *Appl Energy*, 2015.

[104] T.Lieuwen, V. McDonell, E. Petersen, and D. Santavicca. Fuel flexibility influences on premixed combustor blowout, flashback, autoignition, and stability. *J. Eng. Gas Turbines Power*, 130(1), 2008.

[105] David S Underwood, Ian A Waitz, and Edward M Greitzer. Confined swirling flows with heat release and mixing. *Journal of Propulsion and Power*, 16(2):169–177, 2000.

[106] Agustin Valera-Medina, Nicholas Syred, and Anthony Griffiths. Characterization of large coherent structures in a swirl burner under combustion conditions. In *AIAA International Meeting*, pages 2009–646, 2009.

[107] Ping Wang. *Large eddy simulation of turbulent swirling flows and turbulent premixed combustion.* PhD thesis, Lund University, 2005.

[108] Hirotatsu Watanabe, Santosh J. Shanbhogue, and Ahmed F. Ghoniem. Impact of equivalence ratio on the macrostructure of premixed swirling CH4/Air and CH4/O2/CO2 flames. *Proceedings of ASME Turbo Expo*, (GT2015-43224), 2015.

[109] DM Wicksall and AK Agrawal. Acoustics measurements in a lean premixed combustor operated on hydrogen/hydrocarbon fuel mixtures. *International journal of hydrogen energy*, 32(8):1103–1112, 2007.

[110] Qingguo Zhang, Santosh J Shanbhogue, Shreekrishna, Tim Lieuwen, and Jacqueline O'Connor. Strain characteristics near the flame attachment point in a swirling flow. *Combustion science and technology*, 183(7):665–685, 2011.